Biomolecular Tools for Noninvasive Imaging and Manipulation of Engineered Cells

Thesis by
Di Wu

In Partial Fulfillment of the Requirements for
the Degree of Doctor of Philosophy
in Medical Engineering

CALIFORNIA INSTITUTE OF TECHNOLOGY
Pasadena, California

2021
(Defended September 18th, 2020)

Di Wu
ORCID: 0000-0002-6848-668X

ACKNOWLEDGEMENTS

First and foremost, I wish to acknowledge my PhD advisor Mikhail Shapiro, who is hands down the best mentor and role model I could have asked for. I am extremely grateful for the opportunities he provided that challenged me to grow both scientifically and personally. Mikhail gave me interesting problems to tackle and room to explore, which allowed me to discover the pleasure of finding things out. He provided valuable feedback and words of encouragement when I needed them the most. In addition, Mikhail has fostered a fun, stimulating, and caring lab culture that I am grateful to be a part of, day in and day out.

I would like to thank the scientific mentors that I had before coming to Caltech: Guosong Hong, Hongjie Dai, and Warren Chan. They have initiated me to life in a lab, helped to shape my research interests, and continued to offer helpful advice on life and career.

I would like to thank YC Tai, Mory Gharib, and Rob Phillips for being members of my PhD committee. I would also like to thank YC for creating the Medical Engineering program at Caltech of which I am proud to be a member of its inaugural class. I am grateful to Rob for his penetrating questions on science and life that I often return to and gain from.

I am grateful to the many collaborators and colleagues with whom I had the good fortune of working alongside in the Shapiro Lab over the years: Mohamad Abedi, Maria Paulene Abundo, Avinoam Bar-Zion, Raymond Bourdeau, Marjorie Buss, Hunter Davis, Xiaozhe Ding, Mengtong Duan, Arash Farhadi, Abdullah Farooq, Rob Hurt, Gabrielle Ho, Zhiyang Jin, Jeong Hoon Ko, Jérôme Lacroix, Anupama Lakshmanan, Justin Lee, Audrey Lee-Gosselin, Bill Ling, George Lu, David Mittelstein, Dina Malounda, David Maresca, Arnab Mukherjee, Dan Piraner, Claire Rabut, Pradeep Ramesh, Danny Sawyer, Shirin Shivaei, Jerzy Szablowski, Teresa Tran, Yuxing Yao, and Sangjin Yoo. These are incredibly talented and motivated scientists, and I have gained so much from interacting with each of them.

I am also extremely fortunate to have worked with amazing collaborators outside the lab: Diego Baresch, Colin Cook, Zhichao Ma, Tian Qiu, Peer Fischer, James Friend. They have been extremely generous to share their time and expertise, which have been instrumental to the work presented in this thesis.

I am grateful to the Caltech Medical Engineering Department and the Amgen-Charles Lee Powell Foundation for their generous support during my initial years at Caltech.

Thank you to Christine Garske for going above and beyond in making my life effortless in Medical Engineering.

On a more personal note, I would like to extend my profound appreciation for the people in the Shapiro Lab who, in addition to being incredible colleagues, have also become my family and lifelong friends. The past 7 years have been the most memorable years of my life because of them. Thank you, Mo, for being like a brother to me, and being on this PhD journey with me from start to finish. Thank you, Pradeep, for welcoming me with open arms and making me feel at home from the very beginning. Thank you, Dan, for taking me on as his rotation student and initiating me into the lab. Thank you, Zhiyang and Teresa for their caring friendship and all the heartfelt conversations. Thank you, Mittelstein, Danny, and Abdullah for always being up for a wild discussion, and for being wonderful travel companions. Thank you, Maresca, Jerzy, George, and Avinoam for sharing their unique perspectives on life and academia. Thank you to Bill, Shirin, Anu, Justin, Rob, and Arash for all the laughs and shenanigans over the years.

Thank you to Cathy Miao, for sharing part of this journey with me, and for teaching me to have balance in my life.

Finally, my deepest gratitude goes to my family for their unparalleled love and support. I am grateful to my mom, Hong, for being my mentor in life and a constant source of inspiration. I am grateful to my grandparents, BangJian and Fuhe, for raising me during my early years and for their continued love and support. I am grateful to my dad, Zhuxin, for teaching me to live authentically. I am also grateful to my family for supporting my moving away from home towards better opportunities.

It takes a village, and I am extremely fortunate to have these people in my life. This thesis is dedicated to them.

ABSTRACT

Today's most advanced tools for imaging and controlling cellular function are based on fluorescent or light-controlled proteins, which have limited utility in large organisms or engineered living materials due to the scattering of photons. Deeply penetrant forms of energy such as magnetic fields and sound waves, while routinely used to monitor and treat diseases on the tissue and organism level, do not process the equivalent set of biomolecular tools for interfacing with biology at the molecular and cellular scale. Emerging technologies discussed in this thesis aim to bridge this gap by harnessing biomolecules that have the appropriate physical properties to interact with sound waves or magnetic fields in such a way that enables the visualization and control of specific cells (Chapter 1). We describe two additions to the expanding toolkit for noninvasive imaging and control. In the first case, we show that gas vesicles, a class of hollow protein nanostructures naturally found in aquatic single-cell organisms, can be used as acoustic actuators to enable the control of cellular forces, movement, and patterning using ultrasound (Chapter 2). In the second case, we show that aquaporins, a class of membrane water channels, can be used to alter cellular permeability and serve as genetic reporters for magnetic resonance imaging (Chapter 3). These tools provide critical capabilities for interfacing with cellular function noninvasively and could open the door to applications in various research, biomedical, and industrial settings.

PUBLISHED CONTENT AND CONTRIBUTIONS

Wu D, Baresch D, Cook C, Malounda D, Maresca D, Abundo MP, Mittelstein DR, Shapiro MG. (2019) "Genetically Encoded Nanostructures Enable Acoustic Manipulation of Engineered Cells". In: *BioRxiv* 691105. doi:10.1101/691105.

DW conceived the study with MGS, DB, and DMaresca, designed and fabricated the devices with CC and DRM, prepared the samples with DMalounda, designed and conducted the experiments with DB, analyzed the data, and wrote the manuscript with MGS.

Mukherjee A[†], **Wu D**[†], Davis HC, Shapiro MG (2016) "Non-Invasive Imaging Using Reporter Genes Altering Cellular Water Permeability". In: *Nature Communications* 7, 13891. doi:10.1038/ncomms13891.

([†]Equal Contribution)

DW designed, performed, and analyzed data from *in vivo* experiments with AM, and participated in the writing of the manuscript.

Piraner DI, Farhadi A, Davis HC, **Wu D**, Maresca D, Szablowski JO, Shapiro MG (2017) "Going Deeper: Biomolecular Tools for Acoustic and Magnetic Imaging and Control of Cellular Function". In: *Biochemistry*. doi:10.1021/acs.biochem.7b00443.

DW participated in the writing of the manuscript.

Maresca D[†], Lakshmanan A[†], Abedi M, Bar-Zion A, Farhadi A, Lu GJ, Szablowski JO, **Wu D**, Yoo S, Shapiro MG (2018) "Biomolecular Ultrasound and Sonogenetics". In: *Annual Review of Chemical and Biomolecular Engineering*. 9, 229–52. doi:10.1146/annurev-chembioeng-060817-084034.

DW participated in the writing of the manuscript.

TABLE OF CONTENTS

LIST OF ILLUSTRATIONS AND/OR TABLES

Chapter 1

BIOMOLECULAR TOOLS FOR ACOUSTIC AND MAGNETIC IMAGING AND CONTROL OF CELLULAR FUNCTION

This chapter is in large part a reformatted version of the manuscript entitled " Going Deeper: Biomolecular Tools for Acoustic and Magnetic Imaging and Control of Cellular Function" published by Piraner D.I., Farhadi A, Davis H.C., Wu D., Maresca D., Szablowski J.O., and Shapiro M.G. in *Biochemistry*[1]. Under the supervision of Mikhail Shapiro, I contributed to the writing of the manuscript.

Abstract

Most cellular phenomena of interest to mammalian biology occur within the context of living tissues and organisms. However, today's most advanced tools for observing and manipulating cellular function – based on fluorescent or light-controlled proteins – work best in cultured cells, transparent model species or small, surgically accessed anatomical regions. Their reach into deep tissues and larger animals is limited by photon scattering. To overcome this limitation, we must design biochemical tools that interface with more penetrant forms of energy. For example, sound waves and magnetic fields easily permeate most biological tissues, allowing the formation of images and delivery of energy for actuation. These capabilities are widely used in clinical techniques such as diagnostic ultrasound, magnetic resonance imaging, focused ultrasound ablation, and magnetic particle hyperthermia. Each of these modalities offers spatial and temporal precision that could be used to study a multitude of cellular processes *in vivo*. However, connecting these techniques to cellular functions such as gene expression, proliferation, migration, and signaling requires the development of new biochemical tools that can interact with sound waves and magnetic fields as optogenetic tools interact with photons. Here, we discuss the exciting challenges this poses for biomolecular engineering, and provide examples of recent advances pointing the way to greater depth in *in vivo* cell biology.

Length scales for studying cellular function *in vivo*

Before discussing technologies for cellular imaging and control, it is useful to think about the length scales on which these techniques must operate. Consider three representative

biological systems: the mammalian microbiome, the adaptive immune system, and the brain (Figure 1a). A microbe's life in the mammalian gastrointestinal tract is intricately linked to its location along the length of the tract, its radial position within the lumen, and its place within a microenvironment such as the colonic crypt[2]. These locations are associated with length scales of centimeters, millimeters, and microns, respectively. Likewise, adaptive immunity is a multi-scale phenomenon. Antigen presentation and recognition occur at sub-micron immunological synapses, while immune cell recruitment from blood and lymphoid organs, proliferation, and regulatory signaling occur on the scale of millimeters to centimeters. Similarly, neural signaling is organized at length scales ranging from sub-micron synapses to millimeter-sized brain regions and centimeter-scale axonal projections.

In all three systems, key biological questions involve the function of particular cell types within a certain spatially-defined anatomical context. For example, which microbes can successfully colonize the small intestine? Which genes do T-cells express after migrating into a tumor and recognizing a neoantigen? How does the activity of excitatory neurons in a certain part of the hippocampus relate to the development of seizures? Each of these questions involves ensemble cellular behaviors occurring on the millimeter scale, which are difficult to recapitulate in *in vitro* models. Studying biology at this scale complements the understanding gained by examining cells at the single-cell and sub-cellular level, and requires a dedicated set of experimental tools.

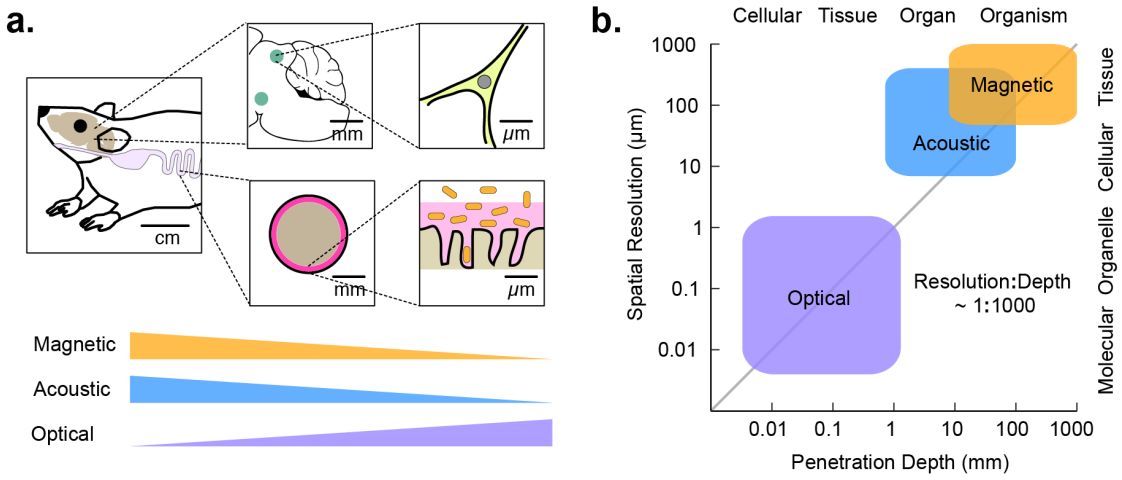

Figure 1 | Modalities for *in vivo* imaging and control of cellular function. (**a**) Diagram of the length scales of several biological processes of interest *in vivo*, and the degree to which these length scales are accessible by imaging technologies. (**b**) Approximate length scales and maximal tissue penetration depths accessible by optical, acoustic, or magnetic imaging.

Forms of energy for biological imaging and control

The key elements of any technology for cellular imaging and control are the form of energy applied to or measured from the sample and the molecular mechanisms connecting this energy to a biological process of interest (Figure 1b). Since the work of van Leeuwenhoek, the dominant energy type used to study biological phenomena has been visible light, with modern microscopy taking advantage of an impressive array of molecular tools to optically visualize and perturb cellular processes. Unfortunately, visible light gets scattered within approximately one millimeter in most tissues, limiting its use to *in vitro* specimens and shallow or surgically accessed anatomical regions.

On the other hand, sound waves and magnetic fields are capable of penetrating deep into tissues. Ultrasound at MHz frequencies permeates through several centimeters, enabling imaging or focused energy deposition with a wavelength-dependent resolution down to approximately 100 μm[3]. This is further improved to below 10 μm with recently developed super-resolution techniques[4]. Due to this excellent performance, ultrasound imaging is widely used in the clinic and in pre-clinical research. In addition, ultrasound can be focused at depth to deliver mechanical forces or localized heating[5]. These capabilities are used clinically for non-invasive ablation of diseased tissues.

Likewise, magnetic fields experience minimal tissue attenuation. They can be used to produce high-contrast images of many organs by exploiting the context-dependent magnetic resonance behavior of nuclear spins, with a spatial resolution on the order of 100 μm. In addition, static or time-varying magnetic fields can produce mechanical forces or heat in tissues containing magnetic nanomaterials[6], which can be localized in to the millimeter scale using field-free point scanning techniques[7].

Based on their tissue penetration and spatiotemporal resolution, sound waves and magnetic fields are well-suited to imaging and controlling the function of cells *in vivo* (Figure 1b). All that is needed is a set of biomolecular tools that can link these forms of energy to specific cellular functions such as gene expression and signaling. Developing such tools presents an exciting challenge to biomolecular engineers. Just as the discovery of the green fluorescent protein stimulated the development of hundreds of reporters, sensors, and actuators through creative protein engineering, recent developments in acoustically and magnetically active

proteins may allow us to engineer a similar variety of biological tools for ultrasound and magnetic resonance. Initial inroads towards this goal are described in the following sections.

Biomolecular tools for ultrasound imaging

Diagnostic ultrasound uses the scattering of sound waves to delineate tissue boundaries, monitor the motion of organs such as the heart and quantify the velocity of blood flow (Figure 2a). Until recently, the prospect of using ultrasound to image the function of specific cells was remote due to the lack of suitable molecular reporters. Conventional ultrasound contrast agents are micron-sized synthetic bubbles that resonantly scatter sound waves. Although these microbubbles can be targeted to specific endovascular targets for molecular imaging in the bloodstream, their size and long-term instability makes it difficult to use them in labeling and monitoring the function of specific cells[8]. Alternatively, scattering synthetic nanoparticles have been explored as ultrasound contrast agents with the potential for cell labeling and extravascular interrogation[9,10].

To connect ultrasound more closely with molecular and cellular biology, we recently adapted a unique class of gas-filled proteins, called gas vesicles or GVs, as the first biomolecular acoustic reporters. GVs evolved in aquatic photosynthetic microbes as a means to regulate buoyancy for optimal access to sunlight and other nutrients[11]. Despite their name, gas vesicles contain no lipids; they comprise a 2 nm-thick protein shell enclosing a hollow interior with dimensions on the order of 250 nm (Figure 2, b-c). Their shell allows gases dissolved in the surrounding media to freely permeate in and out of their interior, while their hydrophobic inner surface prevents the formation of a liquid aqueous phase. GVs are encoded by clusters of 8-14 genes, including two primary structural proteins and several minor constituents, chaperones, and regulators.

In 2014, we showed that GVs can produce ultrasound contrast in purified form, inside cells and *in vivo*, establishing them as the first acoustic biomolecules[12]. Since this initial discovery, considerable advances have been made in understanding the acoustic properties of GVs and improving the ability of ultrasound to detect them with greater sensitivity and specificity. One key finding was that GVs undergo nanoscale buckling deformations under ultrasound (Figure 2d), resulting in non-linear scattering and allowing amplitude-modulated pulse sequences to detect GVs with greater specificity against background tissues (Figure 2e) in a

process analogous to two-photon microscopy[13,14]. Another key finding was that the acoustic properties of GVs can be engineered at the genetic level. In particular, a key component of the GV shell called GvpC influences the response of GVs to pressure, setting thresholds for buckling and irreversible collapse[15]. Tuning GvpC at the genetic level enables modulation of

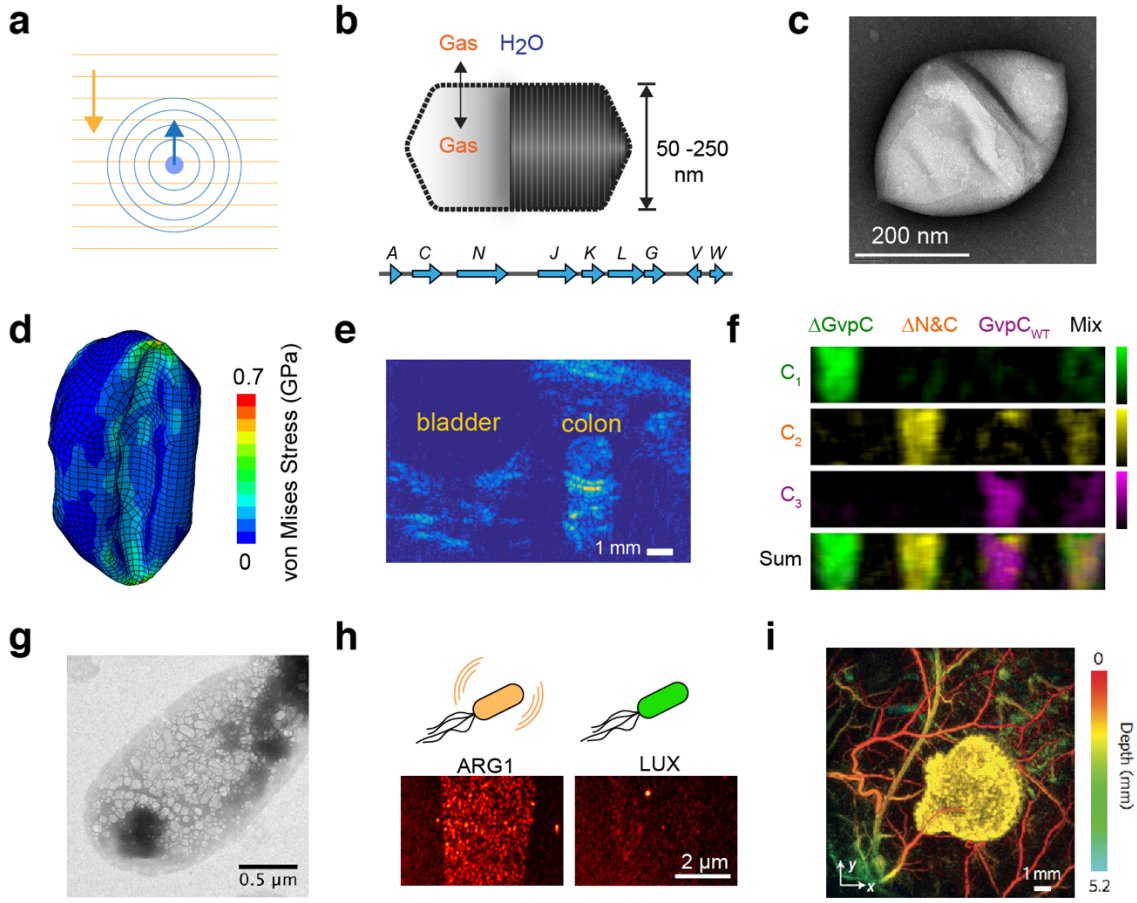

Figure 2 | Biomolecular tools for ultrasound imaging. (**a**) Illustration of sound propagation in the imaging medium and received echo used to form the ultrasound image. (**b**) GVs are hollow protein nanostructures that freely allow diffusion of dissolved gas through their shell but exclude water[12]. GVs are encoded by operons consisting of 8-14 genes. (**c**) Representative transmission electron micrograph of purified GV from Halobacterium[12]. (**d**) Simulation illustrating nanoscale deformation of GVs under ultrasound leading to nonlinear backscattered echo[13]. (**e**) Amplitude-modulation pulse sequence reveals GVs in mouse colon[14] (Reprinted from Maresca, D et al (2017). Nonlinear ultrasound imaging of nanoscale acoustic biomolecules. Applied Physics Letters, 110(7), 73704, with the permission of AIP Publishing). (**f**) Multiplexed imaging of genetically engineered GVs[15]. (**g**) Heterologous expression of GVs in *E. coli* using an optimized GV gene cluster[16]. (**h**) Ultrasound image of E. coli expressing GVs or the non-echogenic luminescence reporter, luciferase[16]. (**i**) Photoacoustic imaging of tumor expressing tyrosinase, and surrounding blood vessels[19].

GVs' nonlinear signals, as well as multiplexed imaging of GV variants with differential pressure sensitivity[15] (Figure 2f). Additionally, fusions of GvpC with other polypeptides enable the tailoring of GV surface properties such as charge or affinity for molecular imaging targets[15].

A major effort is also underway to express GVs heterologously as genetically encoded reporters. As an initial target, we have developed genetic constructs to express GVs in model commensal and pathogenic microbes such as *E. coli* and *S. typhimurium* (Figure 2g)[16]. Imaging these and other microbes in mammalian hosts could enable new studies of the microbiome and the tracking of engineered probiotic therapies. Cells expressing the current generation of acoustic reporter genes can be visualized at densities below 10^8 cells/ml, corresponding to a volume fraction of 0.005% – a level compatible with imaging microbes in the GI tract or tumors (Figure 2h)[16]. Another key milestone was our recent introduction of mammalian acoustic reporter genes, which enabled the expression of GVs in mammalian cells.[17]

An alternative mechanism by which ultrasound can facilitate the visualization of cells *in vivo* is photoacoustic imaging, a technique wherein optical excitation is absorbed and converted into thermoelastic pressure waves, which are detected by ultrasound transducers[18]. This enables the use of light to image deeper structures because photons are allowed to scatter en route to their target, with spatial information provided by ultrasound. The major advantage of photoacoustic imaging compared to pure ultrasound is its ability to leverage existing molecular tools developed for optical imaging, including fluorescent proteins or light-absorbing pigments such as melanin (Figure 2i)[19,20]. However, this technique is still difficult to employ at depths beyond one to two centimeters without causing tissue phototoxicity.

Biomolecular tools for ultrasonic actuation

In addition to imaging, ultrasound can be used to deliver energy to focused regions of tissue, with targeting on the scale of a single millimeter. Depending on beam intensity and pulse duration, this energy can be used to apply mechanical forces, drive resonant cavitation of bubbles, or deposit heat (Figure 3a)[5]. These capabilities are used clinically for non-invasive surgery[21]. If they could instead be harnessed, at lower intensities, to modulate the activity of

specific cells *in vivo*, this would facilitate the study of cellular function within relevant anatomical contexts.

Several nascent approaches have been proposed to enable this possibility. For example, the ability of ultrasound to controllably heat tissue within the well tolerated range of 37–42ºC can be coupled to natural or engineered temperature-dependent signaling pathways. This approach has been used to remotely activate transcription driven by the heat shock promoter, pHSP70, in cultured mammalian cells and live mice[22]. While this approach is highly effective in certain contexts, the thermal set-point and activity level of heat shock promoters varies

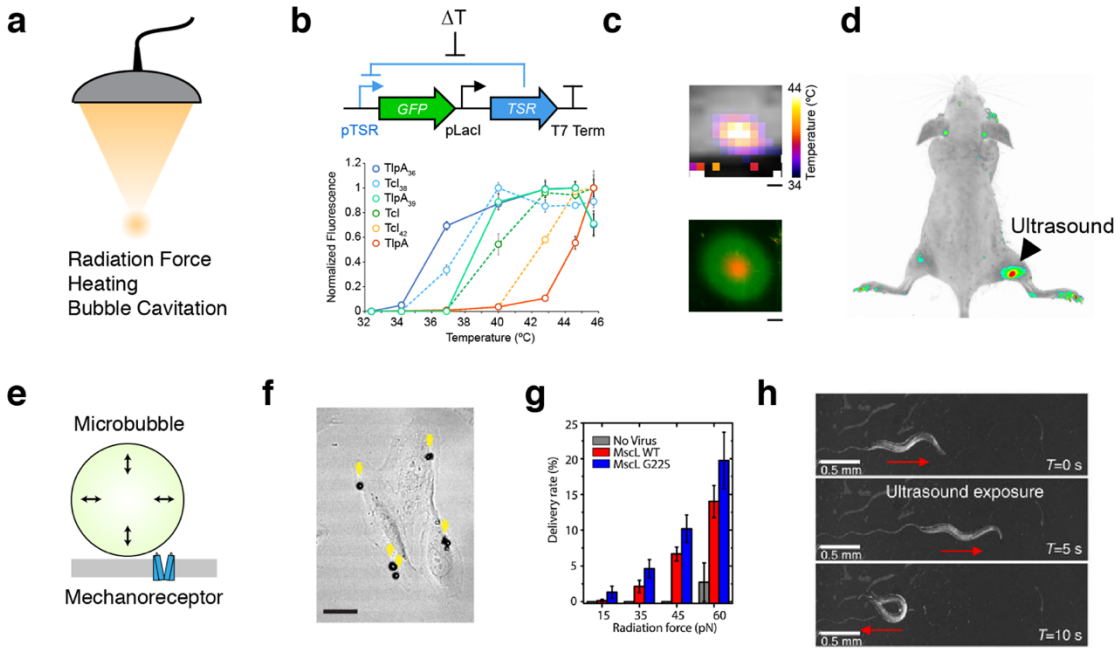

Figure 3 | Biomolecular tools for acoustic control. (**a**) Ultrasound can be focused at depth in tissue and apply several forms of energy to interface with cells. (**b**) Schematic of the gene circuit utilized to gate a GFP reporter gene with a temperature-sensitive repressor (TSR), and a panel of tuned variants of temperature-sensitive repressors[24]. (**c**) MRI thermometry imaging demonstrates a spatial temperature gradient induced by FUS on a plate of bacterial cells, resulting in spatially targeted gene expression[24]. (**d**) *E. coli* were injected into both hindlimbs of a nude mouse; after FUS application to the right hindlimb, reporter gene expression is significantly enriched at the site of heating[24]. (**e**) Diagram of mechanism by which microbubble cavitation can result in membrane deformation leading to mechanoreceptor activation. (**f**) Microbubbles attached to cultured retinal pigment epithelium cells[27]. (**g**) Uptake of membrane-impermeable dye into retinal pigment epithelium cells expressing MscL and functionalized with microbubbles[27]. (**h**) *C. elegans* worm motor response to ultrasound in a bath of microbubbles[28].

between cell types, is not easily tunable, and responds to other stimuli in addition to temperature[23].

In bacteria, endogenous heat shock promoters have only modest activation in response to this range of temperatures, necessitating the development of engineered thermal bioswitches. To address this need, we recently introduced two families of orthogonal, tunable temperature-dependent transcriptional repressors for remote control of bacterial function[24]. These bioswitches are based on the TlpA transcriptional repressor from *S. typhimurium* and a variant of the cI repressor from the Lambda bacteriophage (TcI). Unlike the ~ 10-fold thermal induction of heat shock promoters, the expression of genes downstream of TlpA and TcI operators is turned on by more than 100-fold in response to mild heating. We showed that TlpA and TcI can be engineered through directed evolution to actuate at different desired temperatures, as required by a given application (Figure 3b). In addition, they can be used in combination to build thermal logic circuits, for example to turn on two different functions at two different temperatures. We have demonstrated that these switches can be used to spatially pattern gene expression in plated bacterial cells (Figure 3c) and also in bacteria implanted *in vivo* (Figure 3d). In addition to controlling transcription, these bioswitches can also be used to control protein-protein interactions and protein localization. We showed that TlpA monomers can be engineered through rational design to heterodimerize at a tunable transition temperature.[25] When fused to other proteins, engineered TlpA can reversibly control their association and membrane localization in mammalian cells.[25]

The modest fold change of heat shock promoters (HSPs) can also be improved through the engineering of genetic circuits. By allowing HSPs to drive feed-forward or recombinase-based circuits, we showed that a large or sustained transcriptional response can be achieved.[26] Using these architectures in T-cells, we demonstrated the heat-inducible expression of chimeric antigen receptors and cytokines, and the killing of target tumor cells.[26]

Besides heating, ultrasound is also able to apply mechanical forces to tissues. These forces, which are amplified by acoustically active structures such as microbubbles, could be coupled to signaling elements such as mechanosensitive ion channels, allowing non-invasive control of cellular signaling. This concept was recently demonstrated *in vitro* by combining synthetic microbubbles with mammalian cells heterologously expressing the *E. coli* mechanosensitive ion channel MscL[27]. Microbubbles were similarly used to stimulate the endogenous

mechanosensor Trp4 in *C. elegans*[28]. Unlike thermal stimuli, which are typically associated with timescales on the order of seconds, mechanical effects can be produced on the order of milliseconds, potentially allowing more rapid control of cellular signaling. However, techniques requiring microbubbles are limited in their application to mammals due to the difficulty of delivering bubbles to relevant tissues.

In addition to directly controlling cellular function, ultrasound can be used to spatially target the delivery of genetically encoded tools or treatments. In the brain, such delivery can be targeted non-invasively by opening the blood-brain barrier reversibly at a specific location using focused ultrasound and intravascular microbbubles[29]. This technique allows the delivery of adeno-associated virus (AAV) vectors to targeted regions with millimeter precision[30]. This method has recently been used to deliver AAV vectors encoding for the chemogenetic receptors hM3D(Gq) and hM4D(Gi) into ultrasound-targeted brain regions, which can then be activated or inhibited upon the systemic administration of a small-molecule drug.[31]

Biomolecular tools for magnetic resonance imaging

Like ultrasound, MRI derives contrast from both, endogenous variation in the properties of tissue and molecular contrast agents. Taking advantage of the rich behavior of nuclear spins under various physical and chemical conditions has enabled the development of several classes of biomolecular MRI reporters[32,33]. One major class comprises proteins that contain paramagnetic metals, such as iron or manganese, or lead to the accumulation of these ions in tissue. Proteins in this class include ferritin, bacterial cytochromes, the transferrin receptor and other transporters (Figure 4a-b). Paramagnetic species in these proteins produce T_1 contrast through spin exchange of coordinated water protons and T_2 contrast by distorting the magnetic field near the protein. Another class of reporters includes proteins with large numbers of exchangeable protons – the nuclear spin most commonly imaged with MRI. These protein-bound protons resonate at a distinct frequency (chemical shift) relative to water-bound protons, and can be selectively saturated with radiofrequency pulses, quenching their MRI signal. By applying such saturation while these protons exchange rapidly with the aqueous pool, the signal of the entire pool can be substantially reduced. This “catalytic”

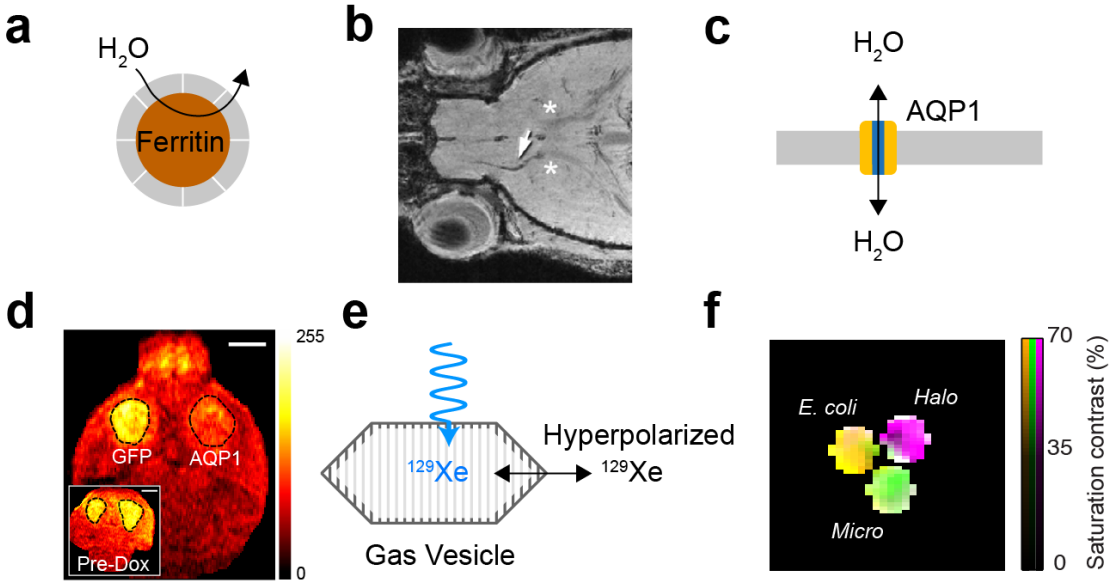

Figure 4 | Biomolecular tools for magnetic resonance imaging. (**a**) Metalloproteins interact magnetically with aqueous ^{1}H nuclear spins, leading to T_1 or T_2 MRI contrast. (**b**) Migrating neuroblasts expressing ferritin produce a hypointense track (arrow) in T_2 weighted MRI[59]. Asterisks denote adenovirus injection sites. (**c**) Overexpression of aquaporin enhances passive diffusion of water across the cell membrane, resulting in contrast on diffusion weighted MRI. (**d**) AQP1 expression in mouse xenograft shows significant contrast compared to contralateral GFP expressing xenograft after expression is induced with doxycycline[36].(**e**) GVs interact with hyperpolarized xenon dissolved in biological media, producing contrast in ^{129}Xe MRI.(**f**) Genetically distinct GVs produce different chemical shifts in ^{129}Xe MRI, enabling multiplexed imaging[39].

contrast scheme is called chemical exchange saturation transfer, or CEST. Proteins detectable with this method include a synthetic lysine-rich protein[34] and human protamine[35].

While these pioneering reporter types have been used to demonstrate the imaging of genetically defined cells using MRI, they are generally limited by their low molecular sensitivity (requiring protein concentrations on the order of μM) or the requirement of metal cofactors, which may not always be bioavailable. Recent efforts have therefore been focused on developing alternative classes of reporters that are more sensitive and do not require metals. For example, we recently introduced aquaporin 1 as a biomolecular reporter for MRI based on its ability to enhance the diffusion of water across cell membranes (Figure 4c)[36]. Aquaporins are transmembrane channels that passively conduct water with exquisite selectivity at rates of up to one billion water molecules per channel per second. We showed that the overexpression of this autologous, non-toxic, metal-free molecule produces contrast

in diffusion-weighted MRI at concentrations below 500 nM, allowing non-invasive imaging of gene expression *in vitro* and *in vivo* (Figure 4d). In addition to aquaporin 1, other water-permeable channels such as the urea transporter can produce diffusion-based contrast, albeit with lower channel selectivity[37].

To push the molecular and cellular sensitivity of MRI even further, recent work has focused on directly addressing a fundamental physical limitation of conventional magnetic resonance: the weak magnetic alignment of nuclear spins under thermal equilibrium. This low polarization results in overall MRI signals approximately 10^5 times weaker than they could be if all the available spins aligned with the applied magnetic field. This limitation can be overcome with hyperpolarization – an advanced technique in which nuclei are prepared via physical methods in a state of non-equilibrium polarization that is up to 10,000-fold stronger than baseline[38]. Hyperpolarized nuclei such as the noble gas ^{129}Xe can then be delivered to the body by inhalation to be imaged during their polarization half-life of a few seconds. Because each hyperpolarized atom carries a much stronger signal than thermally polarized molecules, MRI reporters acting on these nuclei are detectable at much lower concentrations than their conventional counterparts. The first biomolecular reporters for hyperpolarized xenon MRI were GVs, the aforementioned gas-filled protein nanostructures. GVs allow xenon dissolved in surrounding media to exchange in and out of their gaseous compartment, producing MRI contrast through CEST at picomolar concentrations (Figure 4, e-f)[39]. Other proteins active as contrast agents for ^{129}Xe MRI and other hyperpolarized nuclei have also been reported[40,41]. GVs can also be imaged directly by MRI without ^{129}Xe, owing to the difference in the magnetic susceptibility of air and water, allowing GVs to be visualized using susceptibility-weighted imaging.[42]

In addition to reporters connected to gene expression, biomolecules have also been engineered as MRI sensors – allowing dynamic tracking of processes such as neurotransmission and kinase signaling. One class of such sensors, inspired by pioneering synthetic approaches[43], comprises iron-containing metalloproteins in which the accessibility of an open iron coordination site to water is modulated by the binding of small molecules, thereby altering T_1 contrast[44]. Directed evolution allows the tuning of this small molecule binding site for selective interactions with neurotransmitters, such as dopamine and serotonin. The resulting reporters have been used to image the dynamics of neurotransmitter release and reuptake in rodent brains[45]. Other biomolecular sensor constructs, based on T_2

and CEST mechanisms, have been developed to image signals such as kinase and protease activity[46].

Biomolecular tools for magnetic control

Magnetic fields exert forces on magnetically active materials such as superparamagnetic and ferromagnetic particles[6]. Depending on the particle type, these forces can be sufficient to guide the movement of materials or cells in the body and actuate receptor signaling (Figure 5a). In addition, rapidly alternating magnetic fields can generate heat in particles whose magnetization oscillates with the applied field, which in turn can be used to control temperature-dependent processes (Figure 5b).

Most strategies for magnetic control of cell function have relied on synthetic magnetic nanoparticles as transducers of the magnetic field. For example, superparamagnetic iron oxide nanoparticles have been used to cluster cell surface receptors or apply directly actuating forces on integrin and notch[47] (Figure 5c). In addition, superparamagnetic particles have been used in combination with alternating fields to activate temperature-sensitive ion channels such as TRPV1[48] (Figure 5d). This approach enabled remote control of neural signaling *in vivo* in mice surgically implanted with such particles[49] (Figure 5e-f). Additionally, cells containing iron oxide particles have been concentrated at certain locations *in vivo*[50,51].

Translating these approaches into more versatile, fully-genetic constructs is challenging due to the unsolved problem of heterologous biosynthesis of strongly magnetic nanomaterials. Although superparamagnetic and ferromagnetic iron oxide nanocrystals are made by magnetotactic bacteria[52], the genes encoding their specialized organelle machinery for such synthesis have so far been transferred only to their close genetic relatives. The magnetic nanostructures formed in commensal microbes and mammalian cells, such as ferritin, tend to be paramagnetic or weakly superparamagnetic. Efforts to increase the magnetic strength of ferritin through genetic engineering have so far come up short of qualitatively altering its magnetic character.

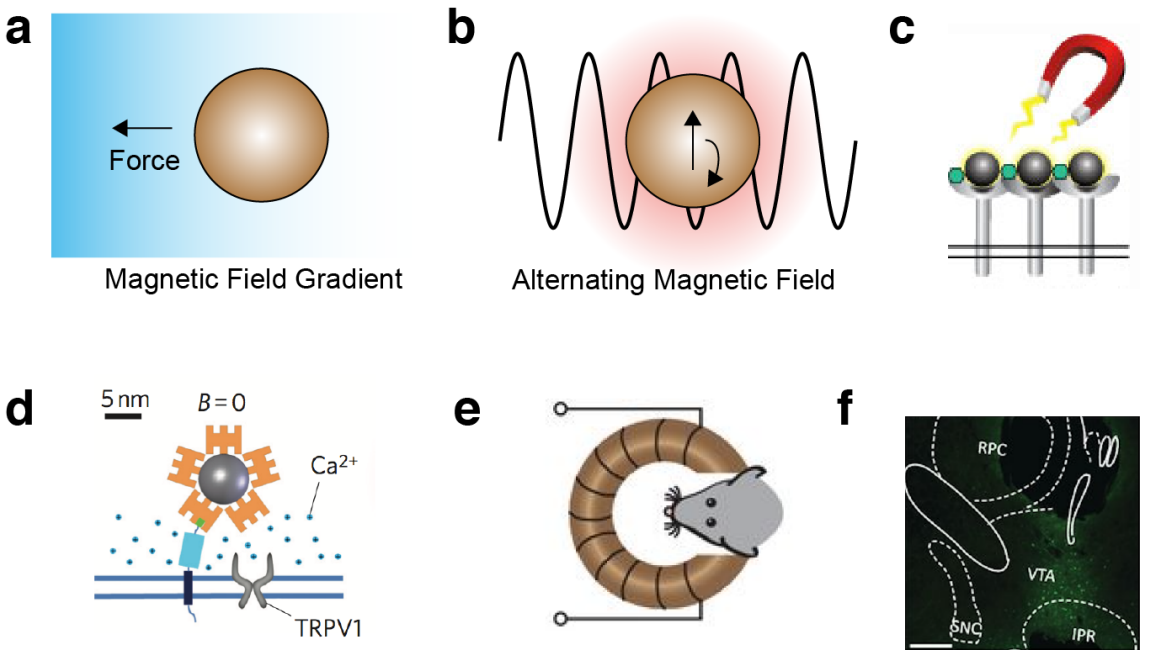

Figure 5 | Biomolecular tools for magnetic control. (**a**) Magnetic field gradients exert a force on magnetic particles. (**b**) Alternating magnetic fields heat magnetic particles by inducing oscillations in the magnetic moment of the nanoparticle. (**c**) Magnetic fields can induce the clustering of magnetic particles, and receptors to which they are bound[47]. (**d**) Coupling magnetic nanoparticles to the heat-sensitive ion channel TRPV1 enables magnetic control of calcium influx to the cell[48]. (**e**) Remote deep brain stimulation using alternating magnetic fields applied to mice with implanted magnetic nanoparticles and virally transduced TRPV1[49]. (**f**) Expression of the neural activity marker cFos in the ventral tegmental area (VTA) of the mouse brain after injection with TRPV1-encoding virus, magnetic nanoparticles and the application of alternating field stimulation[49].

Despite this physical limitation, some groups have reported that fusions of ferritin to temperature- and mechanically-sensitive ion channels allow neurons expressing these channels to be activated remotely using both alternating and static magnetic fields[53,54]. These reports are somewhat surprising based on classical theoretical estimates of the forces and temperatures that could be produced by ferritin[55]. Experimental quantification of the temperature generated by ferritin also revealed no temperature increase in alternating magnetic fields.[56] However, it is possible that as-yet unknown alternative mechanisms are at play.

Outlook

The development of biomolecular tools for non-invasive cellular imaging and control is in its infancy. Inspired by the history and impact of fluorescent and optogenetic proteins, many opportunities exist to develop acoustic and magnetic technologies connected to a variety of cellular processes. For example, biomolecular ultrasound imaging is a new field animated 6 years ago with the development of GVs as its first biomolecular reporter. Much remains to be learned about the acoustic properties of these molecules and how they can be tuned at the genetic level to increase imaging sensitivity, or engineered to respond dynamically as sensors of cellular signaling. In addition, more work is needed to transfer the machinery encoding GVs to a greater number of species. This work takes place against a backdrop of other exciting developments in ultrasound, exemplified by super-resolution imaging[4] and the recent invention of functional ultrasound (fUS), a technique for imaging neural activity non-invasively with improved spatiotemporal resolution compared to functional MRI (< 100 μm and < 10 ms) using transducers that can be mounted on freely moving animals[57].

Biomolecular MRI is only slightly more mature, with an expanding variety of contrast mechanisms but no clear frontrunner to become the go-to molecule for *in vivo* cellular imaging. Recently developed aquaporin-based reporter genes offer unique advantages in terms of their simplicity and biocompatibility, while GVs have the potential to bring the advantages of hyperpolarization to boosting the *in vivo* sensitivity of cellular MRI. Engineering both of these molecules and accompanying *in vivo* imaging methods for maximum sensitivity and potential use as dynamic sensors are major avenues for future research. In addition, an outstanding grand challenge is the engineering of heterologous magnetite biosynthesis, which would provide powerful MRI contrast, as well as opportunities for actuation. In parallel with these molecular efforts, progress is being made on improving the information content of MRI images. For example, we recently used nitrogen vacancy diamond magnetometry, an optical technique for imaging magnetic fields, to map the nanoscale magnetic field in cells containing iron oxide nanoparticles and connect these maps to the T_2 contrast seen by MRI[58]. This study demonstrated experimentally that the spatial arrangement of magnetic materials inside cells strongly influences contrast, guiding the development of magnetic cellular reporters and sensors and imaging parameters for their specific identification *in vivo*.

Complementing these evolving imaging technologies, much additional work on genetically encodable agents is needed to control cellular responses with acoustic or magnetic energy.

For example, there is a lack of mammalian thermal bioswitches that are orthogonal to pleotropic heat shock pathways and tunable to different temperature thresholds analogously to the system we developed for microbial remote control. In addition to regulating gene expression, tools are needed to connect thermal inputs directly to signaling pathways. Similarly, for ultrasound actuation based on mechanical forces, use in mammals will require eliminating the need for synthetic microbubbles to produce constructs that can be fully genetically encoded. Likewise, the synthetic magnetic particles used in well-accepted magnetic control techniques using thermal, mechanical, or clustering mechanisms must be replaced with genetically encodable materials. The potential use of ferritin for this purpose requires further study to reconcile its encouraging empirical performance and predicted lack of efficacy based on previously studied physical properties.

In summary, going deeper into the body to study cellular function within its native *in vivo* context requires engineering interactions between deeply penetrant forms of energy and biomolecules to enable non-invasive imaging and control. Several recent advances have provided exciting proofs or concept for this approach, and inform the development of new classes of biomolecular tools. Many depths remain to be plumbed.

References

1. Piraner, D. I. *et al.* Going Deeper: Biomolecular Tools for Acoustic and Magnetic Imaging and Control of Cellular Function. *Biochemistry* vol. 56 5202–5209 (2017).
2. Donaldson, G. P., Lee, S. M. & Mazmanian, S. K. Gut biogeography of the bacterial microbiota. *Nat. Rev. Microbiol.* **14**, 20–32 (2015).
3. Foster, F. S., Pavlin, C. J., Harasiewicz, K. A., Christopher, D. A. & Turnbull, D. H. Advances in ultrasound biomicroscopy. *Ultrasound Med. Biol.* **26**, 1–27 (2000).
4. Errico, C. *et al.* Ultrafast ultrasound localization microscopy for deep super-resolution vascular imaging. *Nature* **527**, 499–502 (2015).
5. Humphrey, V. F. Ultrasound and matter-Physical interactions. *Progress in Biophysics and Molecular Biology* (2007) doi:10.1016/j.pbiomolbio.2006.07.024.
6. Pankhurst, Q. A., Connolly, J., Jones, S. K. & Dobson, J. Applications of magnetic nanoparticles in biomedicine. *J. Phys. D. Appl. Phys.* **36**, R167–R181 (2003).
7. Tasci, T. O. *et al.* Focused RF hyperthermia using magnetic fluids. *Med. Phys.* **36**, 1906–1912 (2009).
8. Abou-Elkacem, L., Bachawal, S. V & Willmann, J. K. Ultrasound molecular imaging: Moving toward clinical translation. *Eur. J. Radiol.* **84**, 1685–93 (2015).
9. Sheeran, P. S., Luois, S. H., Mullin, L. B., Matsunaga, T. O. & Dayton, P. A. Design of ultrasonically-activatable nanoparticles using low boiling point perfluorocarbons. *Biomaterials* **33**, 3262–3269 (2012).
10. Chen, F. *et al.* Exosome-like silica nanoparticles: a novel ultrasound contrast agent for stem cell imaging. *Nanoscale* **9**, 402–411 (2017).
11. Pfeifer, F. Distribution, formation and regulation of gas vesicles. *Nature Reviews Microbiology* (2012) doi:10.1038/nrmicro2834.
12. Shapiro, M. G. *et al.* Biogenic gas nanostructures as ultrasonic molecular reporters. *Nat. Nanotechnol.* **9**, 311–316 (2014).
13. Cherin, E. *et al.* Acoustic behavior of Halobacterium salinarum gas vesicles in the high frequency range: experiments and modeling. *Ultrasound Med. Biol.* 1–15 (2017) doi:10.1016/j.ultrasmedbio.2016.12.020.
14. Maresca, D. *et al.* Nonlinear ultrasound imaging of nanoscale acoustic biomolecules. *Appl. Phys. Lett.* **110**, 073704 (2017).
15. Lakshmanan, A. *et al.* Molecular Engineering of Acoustic Protein Nanostructures. *ACS Nano* **10**, 7314–7322 (2016).
16. Bourdeau, R. *et al.* Acoustic reporter genes for non-invasive imaging of microbes in mammalian hosts.
17. Farhadi, A., Ho, G. H., Sawyer, D. P., Bourdeau, R. W. & Shapiro, M. G. Ultrasound imaging of gene expression in mammalian cells. *Science (80-.).* **365**, 1469–1475 (2019).
18. Wang, L. V & Yao, J. A practical guide to photoacoustic tomography in the life

sciences. *Nat. Methods* **13**, 627–638 (2016).

19. Jathoul, A. P. *et al.* Deep in vivo photoacoustic imaging of mammalian tissues using a tyrosinase-based genetic reporter. *Nat. Photonics* **9**, 239–246 (2015).

20. Yao, J. *et al.* Multiscale photoacoustic tomography using reversibly switchable bacterial phytochrome as a near-infrared photochromic probe. *Nat. Methods* **13**, 1–9 (2015).

21. Hynynen, K. MRIgHIFU: A tool for image-guided therapeutics. *J. Magn. Reson. Imaging* **34**, 482–493 (2011).

22. Kruse, D. E., Mackanos, M. a, O'Connell-Rodwell, C. E., Contag, C. H. & Ferrara, K. W. Short-duration-focused ultrasound stimulation of Hsp70 expression in vivo. *Phys. Med. Biol.* **53**, 3641–60 (2008).

23. Aït-Aïssa, S., Porcher, J. M., Arrigo, A. P. & Lambré, C. Activation of the hsp70 promoter by environmental inorganic and organic chemicals: Relationships with cytotoxicity and lipophilicity. *Toxicology* **145**, 147–157 (2000).

24. Piraner, D. I., Abedi, M. H., Moser, B. A., Lee-Gosselin, A. & Shapiro, M. G. Tunable thermal bioswitches for in vivo control of microbial therapeutics. *Nat. Chem. Biol.* **13**, 75–80 (2016).

25. Piraner, D. I., Wu, Y. & Shapiro, M. G. Modular Thermal Control of Protein Dimerization. *ACS Synth. Biol.* **8**, 2256–2262 (2019).

26. Abedi, M. H., Lee, J., Piraner, D. I. & Shapiro, M. G. Thermal Control of Engineered T-cells. *ACS Synth. Biol.* **9**, 1941–1950 (2020).

27. Heureaux, J., Chen, D., Murray, V. L., Deng, C. X. & Liu, A. P. Activation of a bacterial mechanosensitive channel in mammalian cells by cytoskeletal stress. *Cell. Mol. Bioeng.* **7**, 307–319 (2014).

28. Ibsen, S., Tong, A., Schutt, C., Esener, S. & Chalasani, S. H. Sonogenetics is a non-invasive approach to activating neurons in Caenorhabditis elegans. *Nat. Commun.* **6**, 1–12 (2015).

29. Hynynen, K., McDannold, N., Vykhodtseva, N. & Jolesz, F. a. Noninvasive MR imaging-guided focal opening of the blood-brain barrier in rabbits. *Radiology* **220**, 640–646 (2001).

30. Poon, C., McMahon, D. & Hynynen, K. Noninvasive and targeted delivery of therapeutics to the brain using focused ultrasound. *Neuropharmacology* **4**, 519–526 (2016).

31. Szablowski, J. O., Lee-Gosselin, A., Lue, B., Malounda, D. & Shapiro, M. G. Acoustically targeted chemogenetics for the non-invasive control of neural circuits. *Nat. Biomed. Eng.* **2**, 475–484 (2018).

32. Gilad, A. A. *et al.* MRI Reporter Genes. *J Nucl Med* **49**, 1905–1908 (2008).

33. Mukherjee, A., Davis, H. C., Ramesh, P., Lu, G. J. & Shapiro, M. G. *Biomolecular MRI Reporters: evolution of new mechanisms*. *Progress in Nuclear Magnetic Resonance Spectroscopy* (2017). doi:10.1016/j.pnmrs.2017.05.002.

34. Farrar, C. T. *et al.* Establishing the Lysine-rich Protein CEST Reporter Gene as a

CEST MR Imaging Detector for Oncolytic Virotherapy. *Radiology* **275**, 746–754 (2015).

35. Oskolkov, N. *et al.* Biophysical characterization of human protamine-1 as a responsive CEST MR contrast agent. *ACS Macro Lett.* **4**, 34–38 (2015).

36. Mukherjee, A., Wu, D., Davis, H. C. & Shapiro, M. G. Non-invasive imaging using reporter genes altering cellular water permeability. *Nat. Commun.* **7**, 13891 (2016).

37. Schilling, F. *et al.* MRI measurements of reporter-mediated increases in transmembrane water exchange enable detection of a gene reporter. *Nat. Biotechnol.* 1–6 (2016) doi:10.1038/nbt.3714.

38. Barskiy, D. A. *et al.* NMR Hyperpolarization Techniques of Gases. *Chem. - A Eur. J.* 725–751 (2016) doi:10.1002/chem.201603884.

39. Shapiro, M. G. *et al.* Genetically encoded reporters for hyperpolarized xenon magnetic resonance imaging. *Nat. Chem.* **6**, 629–34 (2014).

40. Wang, Y., Roose, B. W., Palovcak, E. J., Carnevale, V. & Dmochowski, I. J. A Genetically Encoded ??-Lactamase Reporter for Ultrasensitive 129Xe NMR in Mammalian Cells. *Angew. Chemie - Int. Ed.* **55**, 8984–8987 (2016).

41. Patrick, P. S. *et al.* Detection of transgene expression using hyperpolarized ^{13}C urea and diffusion-weighted magnetic resonance spectroscopy. *Magn. Reson. Med.* **73**, 1401–1406 (2015).

42. Lu, G. J. *et al.* Acoustically modulated magnetic resonance imaging of gas-filled protein nanostructures. *Nat. Mater.* **17**, 456–463 (2018).

43. Li, W. H., Fraser, S. E. & Meade, T. J. A calcium-sensitive magnetic resonance imaging contrast agent. *J. Am. Chem. Soc.* **121**, 1413–1414 (1999).

44. Shapiro, M. G. *et al.* Directed evolution of a magnetic resonance imaging contrast agent for noninvasive imaging of dopamine. *Nat. Biotechnol.* **28**, 264–270 (2010).

45. Lee, T., Cai, L. X., Lelyveld, V. S., Hai, A. & Jasanoff, A. Molecular-level functional magnetic resonance imaging of dopaminergic signaling. *Science* **344**, 533–535 (2014).

46. Airan, R. D. *et al.* MRI biosensor for protein kinase A encoded by a single synthetic gene. *Magn. Reson. Med.* **68**, 1919–1923 (2012).

47. Mannix, R. J. *et al.* Nanomagnetic actuation of receptor-mediated signal transduction. *Nat. Nanotechnol.* **3**, 36–40 (2008).

48. Huang, H., Delikanli, S., Zeng, H., Ferkey, D. M. & Pralle, A. Remote control of ion channels and neurons through magnetic-field heating of nanoparticles. *Nat. Nanotechnol.* **5**, 602–606 (2010).

49. Chen, R., Romero, G., Christiansen, M. G., Mohr, A. & Anikeeva, P. Wireless magnetothermal deep brain stimulation. *Science* **347**, 1477–80 (2015).

50. Muthana, M. *et al.* Directing cell therapy to anatomic target sites in vivo with magnetic resonance targeting. *Nat. Commun.* **6**, 8009 (2015).

51. Felfoul, O. *et al.* Magneto-aerotactic bacteria deliver drug-containing nanoliposomes

to tumour hypoxic regions. *Nat. Nanotechnol.* **11**, 1–5 (2016).

52. Faivre, D. & Schüler, D. Magnetotactic Bacteria and Magnetosomes. *Chem. Rev.* **108**, 4875–4898 (2008).

53. Stanley, S. A., Sauer, J., Kane, R. S., Dordick, J. S. & Friedman, J. M. Remote regulation of glucose homeostasis in mice using genetically encoded nanoparticles. *Nat Med* **21**, 92–98 (2015).

54. Wheeler, M. A. *et al.* Genetically targeted magnetic control of the nervous system. *Nat Neurosci* **19**, 756–761 (2016).

55. Meister, M. Physical limits to magnetogenetics. *Elife* **5**, 1–14 (2016).

56. Davis, H. C. *et al.* Nanoscale Heat Transfer from Magnetic Nanoparticles and Ferritin in an Alternating Magnetic Field. *Biophys. J.* **118**, 1502–1510 (2020).

57. Sieu, L.-A. *et al.* EEG and functional ultrasound imaging in mobile rats. *Nat Methods* **12**, 831–834 (2015).

58. Davis, H. C. *et al.* Mapping the Microscale Origins of MRI Contrast with Subcellular NV Diamond Magnetometry. (2016).

59. Iordanova, B. & Ahrens, E. T. In vivo magnetic resonance imaging of ferritin-based reporter visualizes native neuroblast migration. *Neuroimage* **59**, 1004–1012 (2012).

Chapter 2

GENETICALLY ENCODED ACTUATORS FOR ACOUSTIC INVERSION, MANIPULATION, AND PATTERNING OF ENGINEERED CELLS

This chapter is in large part a reformatted version of the manuscript entitled "Genetically encoded actuators for acoustic inversion, manipulation and patterning of engineered cells" by Wu D, Baresch D, Cook C, Ma Z, Malounda D, Maresca D, Abundo M.P., Lee J, Shivaei S, Mittelstein D.R., Qiu T, Fischer P and Shapiro M.G. currently in revision. A pre-print version can be found on *bioRxiv*[1]. Under the supervision of Mikhail Shapiro, my contributions to the work were to conceive, design, and conduct the experiments, analyze and interpret the data, and write the manuscript.

Abstract

The ability to selectively manipulate and control the spatial arrangement of genetically defined cells is critical for the fields of living materials, biomedicine, and synthetic biology. Ultrasound has the ability to manipulate a variety of objects remotely and en masse with high spatial and temporal precision via acoustic radiation force (ARF). However, this capability is currently disconnected from intracellular genetic programs. Here, we show that gas vesicles (GVs) – a unique class of genetically encoded gas-filled protein nanostructures – can serve as genetically encodable actuators for ARF, enabling the selective acoustic inversion and manipulation of engineered cells. Due to their differential density and compressibility relative to water, GVs are effectively moved with acoustic standing waves despite their nanometer dimensions. When expressed inside genetically engineered cells, GVs amplify the ARF experienced by the cells by a factor of ten and invert their acoustic contrast, allowing the cells to be selectively manipulated with sound waves based on their genotype. This enables dynamic patterning, focal trapping, translation, and holographic bioprinting of specific cells with acoustic fields. In addition, the unique material properties of purified GVs enable new modes of acoustic interaction, including force inactivation, multiplexed manipulation, and endosomal labeling. Unlike fluorescent proteins, which have no intrinsic ability to serve as actuators for cellular manipulation, GVs provide a direct link between gene expression and mechanical

actuation, creating a new paradigm for molecular and cellular control in a broad range of contexts.

Introduction

The ability to remotely pattern, actuate, and apply force to genetically specified cells would have many applications in biomedicine and synthetic biology, ranging from the fabrication of biological living materials[2] to drug delivery[3] and noninvasive control of cellular function[4–6]. Ultrasound offers unique advantages in such contexts over optical, magnetic, and printing-based approaches due to its functionality in opaque media, non-invasiveness, relatively high spatial precision on the μm scale, and rapid, reconfigurable field formation. Acoustic radiation force (ARF) allows ultrasound to manipulate materials whose density or compressibility differ from their surrounding medium. This capability has been used to manipulate, pattern, and sort synthetic particles and cells, for example by using acoustic standing waves to create stable attractors for such objects or to separate them in microfluidic devices[7]. However, due to the similarity of acoustic contrast factor among endogenous cellular materials, it is challenging to connect ARF-based actuation directly to intracellular gene expression. Doing so would require a genetically encodable agent capable of drastically altering the acoustic properties of a cell.

To address this need, we hypothesized that gas vesicles (GVs) – a unique class of biologically assembled air-filled protein nanostructures – could experience strong ARF and enable the selective acoustic manipulation of GV-expressing cells. GVs are genetically encoded protein-shelled nanostructures with hydrodynamic diameters on the order of 250 nm (**Figure 1, a-b**) which evolved in aquatic photosynthetic microbes as a means to achieve buoyancy for improved access to sunlight[8]. GVs consist of a physically stable, hollow compartment enclosed by a 2 nm-thick protein shell that is permeable to gas but excludes

liquid water. Based on their unique physical properties, GVs were recently developed as genetically encodable and engineerable contrast agents for non-invasive imaging[9–14]. However, the ability of GVs to serve as actuators of ARF has not been tested.

We hypothesized that GVs' differential density and compressibility relative to aqueous media would allow these nanostructures to experience significant ARF (**Figure 1c**), and that cells genetically engineered to express GVs would experience a drastically different radiation force due to changes in their acoustic properties (**Figure 1, d-e**). We further hypothesized that the resulting forces would act in the opposite direction from other biomaterials, which are generally denser than water, allowing selective acoustic

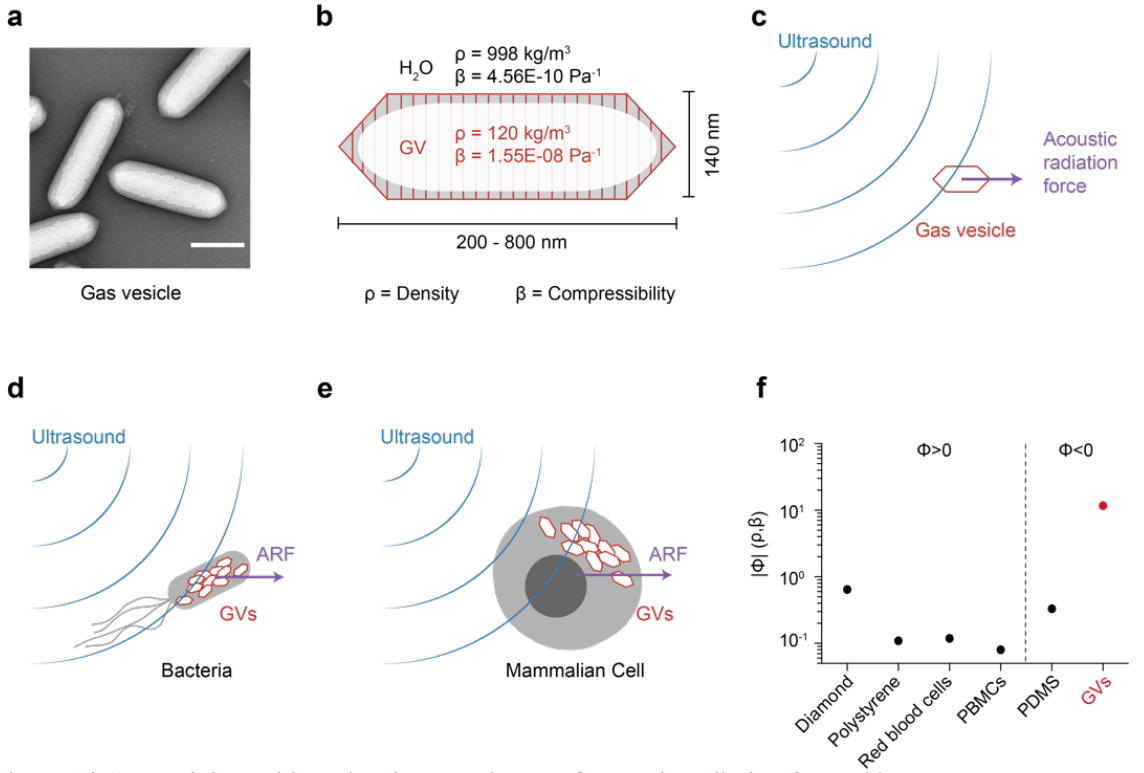

Figure 1 | Gas vesicles as biomolecular transducers of acoustic radiation force. (a) Transmission electron microscopy image of representative GVs from *Anabaena flos-aquae*. **(b)** Schematic drawing of a GV, showing its effective density (ρ) and compressibility (β) relative to that of the surrounding water. **(c)** Illustration of a GV experiencing acoustic radiation force due to applied ultrasound. **(d)** Illustration of a bacterium experiencing enhanced acoustic radiation force due to GVs inside the cell. **(e)** Illustration of a mammalian cell experiencing a unique acoustic radiation force due to the intracellular GVs. **(f)** Estimated magnitude of the acoustic contrast factor, |Φ|, of GVs and several common materials used in acoustic manipulation. Materials to the left and right of the vertical dashed line exhibit positive and negative acoustic contrast in water, respectively. PBMCs, peripheral blood mononuclear cell. PDMS, polydimethylsiloxane.

manipulation. This would connect mechanical actuation directly to the expression of a specific gene – a capability not provided by other genetic labels such as fluorescent proteins. In this study, we test these fundamental hypotheses and demonstrate the use of GVs in the selective acoustic trapping, translation, patterning and holographic bioprinting of genetically engineered cells. In addition, we show that the physical properties of purified GVs provide new capabilities for acoustic multiplexing, pressure measurement, and endocytic cell labeling.

Results

Gas vesicles experience direct acoustic radiation force

To estimate the expected ARF acting on GVs, we modeled them as spherical particles with an effective density of 120 kg/m^3 (ref. [15]) and compressibility of 1.55E-8 Pa^{-1} (ref. [16]). Because both of these values are radically different from water (**Figure 1b**), we predicted that GVs would have a strongly negative acoustic contrast in aqueous media, with a contrast factor of –11.7 (**Figure 1f,** Eq. 1 in Methods). While cells and most biological components exhibit positive acoustic contrast in aqueous solution, a few materials – such as microbubbles, polydimethylsiloxane (PDMS) elastomer microparticles and lipids – exhibit a negative contrast factor, allowing them to migrate up pressure gradients and efficiently separate from positive-contrast materials, as demonstrated in several important applications[17–23]. We hypothesized that GVs could be manipulated in a similar manner by responding directly to ARF at typical frequencies and energy densities of several MHz and ~10-100 J/m^3 (ref. [24]). Despite their nanometer dimensions, we anticipated that GVs' exceptionally large contrast factor would allow them to overcome the challenges of sub-micron particle actuation caused by the volumetric scaling of ARF and the competing process of acoustic streaming[25].

To test the ability of GV nanostructures to be manipulated with ARF, we purified GVs from the cyanobacterium *Anabaena flos-aquae* (Ana), chemically labeled them with a fluorescent dye, and imaged them in suspension inside a microfluidic channel coupled to a bulk piezoelectric resonator operating at 3.8 MHz (**Figure 2a**). The channel width of 200 μm represents a half-wavelength at this frequency, resulting in a pressure node at its center and antinodes (areas of highest pressure) at each wall (**Figure 2b**). As expected based on

their negative acoustic contrast, GVs readily migrated to the pressure anti-nodes upon ultrasound application (**Figure 2, c-d**). As a control, we imaged GVs that were collapsed before the experiment with hydrostatic pressure (**Supplementary Figure 1**). Neither collapsed GVs nor similarly-sized polystyrene tracer nanoparticles – included as an additional control and indicator of fluid motion – migrated in the acoustic field, confirming the absence of streaming.

Next, we quantified the ARF acting on GV particles in solution using single-particle tracking (**Figure 2d**). The Brownian motion of each particle before ultrasound application was used to determine its mobility and hydrodynamic size (**Figure 2e,** Eq. 2 & 5 in Methods). For the same particle, its motion within the acoustic field during ultrasound application was fitted to an equation accounting for the spatial field profile (Eq. 4 in Methods), allowing us to determine the peak particle velocity (**Figure 2f**). The maximum ARF acting on GV particles was then determined by a balance with hydrodynamic drag, and measured to be 24.5 ± 1.7 fN under the acoustic parameters used in this measurement (**Figure 2g**). In contrast, control particles showed no substantial ARF.

Colloidal association of individual GVs within the microfluidic channel resulted in tracked particles having a range of hydrodynamic radii larger than expected from a single GV. Therefore, to estimate the ARF acting on a single GV, we plotted the dependence of the ARF on the hydrodynamic radius of the clusters and fitted it with a power law function accounting for fractal clustering[26,27] (**Figure 2h**, Eq. 6 in Methods, force-mobility exponent = 1.39 ± 0.06; R^2 = 0.744). Given the acoustic energy applied in this experiment (0.25 ± 0.02 J/m^3, **Supplementary Figure 2**), this single-particle force corresponds to an acoustic contrast factor of –15 ± 9, consistent with our theoretical estimate of –11.7 (**Figure 1e**). Using this contrast factor, we can predict the ARF on a single GV across a range of typical acoustic parameters[24] (**Figure 2i**), with the expected force spanning from 0.01 to 10 pN. Forces of this magnitude are more than sufficient to overcome Brownian motion, as shown in our experiments, and are relevant to many biomolecular and cellular interactions[28]. Overall, these results establish GVs as a genetically encodable biomolecular nanomaterial that can be manipulated with acoustic fields.

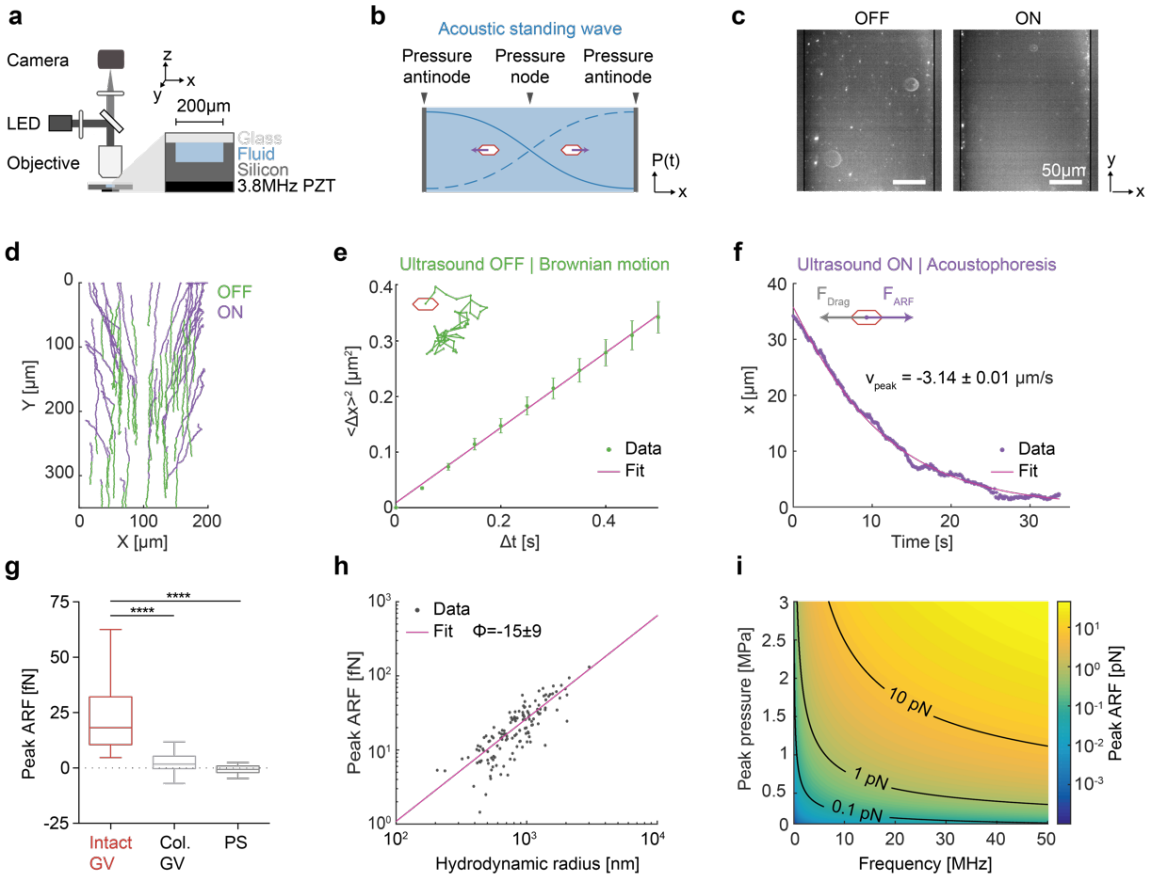

Figure 2 | Gas vesicles experience direct acoustic radiation force. (a) Diagram of the acoustic standing wave setup. A piezoelectric element is coupled to an etched silicon channel whose width is half the acoustic wavelength to generate a standing wave along the *x*-direction. The channel depth is 47 µm. Particles suspended in an aqueous solution are imaged using an epifluorescence microscope. LED, light-emitting diode. PZT, lead zirconate titanate. **(b)** Illustration of the expected migration direction of GVs towards the pressure antinodes of an acoustic standing wave, due to their negative acoustic contrast. **(c)** Fluorescence images of GVs inside the microfluidic channel before ultrasound (OFF) and 100 seconds after ultrasound has been turned on (ON). **(d)** Representative single particle trajectories of GVs before (blue) and during (green) ultrasound application. **(e)** Illustration of Brownian motion (left) and representative single-particle mean square displacement curve used to determine the diffusivity of the particle (right). **(f)** Illustration of particle acoustophoresis (left) and representative single-particle trajectory in the *x* direction during ultrasound application, used to determine the peak particle velocity (right). **(g)** Peak acoustic radiation force of intact GVs (24.5 ± 1.7 fN, n=140), pressure-collapsed GVs (2.0 ± 0.7 fN, N=98), and 200-nm polystyrene particles (-0.6 ± 0.4 fN, N=78). Box-and-whisker plots show the 5-95 percentile, the 25-75 percentile and the median of the distribution. Mann-Whitney test (****: $p<0.0001$). **(h)** Peak ARF of GV particles as a function of hydrodynamic radius, fitted to a fractal clustering model (force-mobility exponent = 1.39±0.06; $R^2 = 0.744$). **i**, Predicted ARF on a single GV across a range of acoustic parameters.

Heterologous expression of GVs enables selective manipulation of engineered bacteria

Having established the ability of GVs to experience strong ARF, we tested the ability of these genetically encodable nanostructures to act as a driver of ARF response in genetically engineered cells. This possibility is based on the fact that GV expression significantly reduces the average density of the cell, resulting, for example, in the floatation of GV-expressing bacteria in water[13]. In combination with an anticipated increase in average cellular compressibility, this is expected to change the acoustic contrast of the cells from +0.07 to –1.1, inverting the sign of their acoustic contrast from positive to negative and increasing its magnitude by more than 10-fold.

We first tested this hypothesis by heterologously expressing intracellular GVs in *E. coli* using a recently developed genetic construct, bacterial acoustic reporter genes (bARG1), comprising of a combination of 13 genes from *A. flos-aquae* and *B. megaterium* (**Figure 3, a-b**).[13] After enriching for high expression using centrifugation, which uses buoyancy as an indicator of GV formation, the cells were labeled with a fluorescent dye to enable live cell tracking. bARG1-expressing cells or control cells with pressure-collapsed intracellular GVs were then subjected to acoustic standing waves under static flow conditions using the microfluidic device depicted in **Figure 2a**. Remarkably, while control cells showed no response to the applied acoustic field, the genetically modified bARG1-expressing cells containing intact intracellular GVs quickly migrated to pressure antinodes at the channel wall (**Figure 3c** and **Supplementary Movie 1**). This result confirms that GV expression results in cells having a negative contrast factor, which is opposite from normal cells (**Figure 1f**), and shows that the magnitude of this contrast factor is substantially larger than for wildtype controls, since under the same acoustic conditions, the control cells did not migrate to the pressure node. This is consistent with the fact that small cells such as bacteria are challenging to manipulate with ARF in their native form[29].

To quantify the ARF enhancement provided by GV expression, we performed single-cell tracking on bARG1-expressing cells containing intact or collapsed intracellular GVs in the presence or absence of applied ultrasound and analyzed the resulting cellular trajectories using the method described above for GVs. We found that while control cells have an acoustic contrast factor of 0.10 ± 0.02, similar to that of wildtype cells, GV expression provides the engineered cells with an acoustic contrast factor of -1.0 ± 0.2, consistent with

our theoretical estimate of -1.1, and representing a 10-fold enhancement in magnitude compared to controls (**Figure 3d**).

After establishing that GVs can strongly amplify cellular ARF, we next hypothesized that cells expressing GVs can be selectively actuated within a heterogenous cell mixture (**Figure 3e**). To test this hypothesis, we implemented a genetic circuit placing the expression of

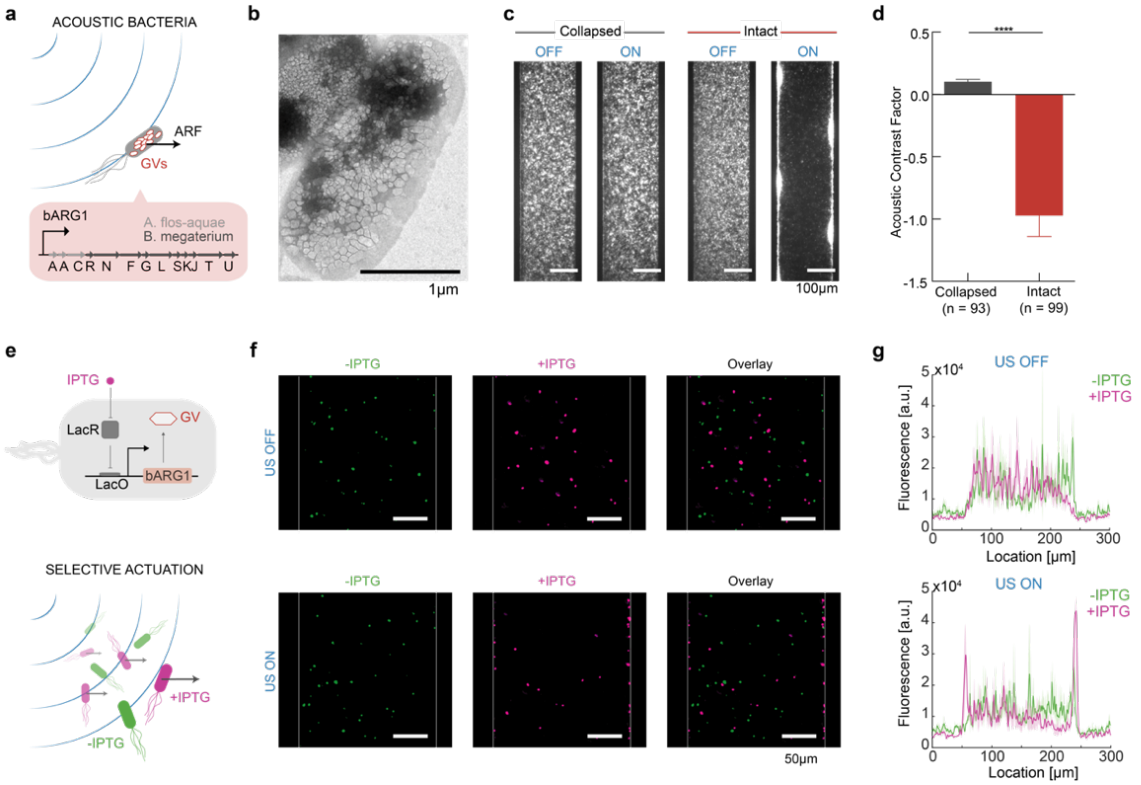

Figure 3 | Gas vesicle expression in bacteria inverts and magnifies their response to ARF. (a) Schematic drawing of genetically modified *E.coli* experiencing an enhanced ARF due to the expression of intracellular GVs as bacterial acoustic reporter genes, bARG1. **(b)** TEM image of *E.coli* containing intracellular GVs upon expression of *arg1*. **(c)** Fluorescence images of *E.coli* inside the microfluidic channel with either intact or collapsed intracellular GVs, either in the presence or absence of applied ultrasound. **(d)** Acoustic contrast factor of *E.coli* with intact GVs (-1.0±0.2, n = 93) and collapsed GVs (0.10±0.02, n = 99). Mann-Whitney test (****: p<0.0001). **(e)** Top, schematic drawing of a bacterial genetic circuit where GV expression is controlled by the inducer Isopropyl β- d-1-thiogalactopyranoside(IPTG). LacR, Lac repressor; LacO, Lac operator. Bottom, schematic drawing of selective acoustic actuation based on cellular genotype. **(f)** Fluorescence images of a heterogenous cell mixture containing induced (+IPTG) and non-induced (-IPTG) bARG1 *E.coli*, either in the presence or absence of applied ultrasound. **(g)** Projected fluorescence signal from either the induced or non-induced *E.coli,* either in the presence or absence of applied ultrasound. Solid line and shaded region correspond to the mean and the standard error of the mean (n = 3).

GVs under the control of chemical induction by isopropyl β-d-1-thiogalactopyranoside (IPTG), and created a cell mixture containing induced and non-induced cells where each population was separately labeled with a fluorescent dye. When we applied ultrasound to this cell mixture under static flow conditions, we observed that only the cells that have been induced with IPTG were actuated, while the non-induced cells showed no response to the applied acoustic field (**Figure 3f-g**). These results demonstrate the ability of GVs to connect an acoustophoretic phenotype to the output of a genetic program, providing the means to selectively manipulate cells based on a variety of cellular states.

Dynamic patterning and rapid biofabrication with engineered bacteria

Having established that GV-expressing cells experience strong ARF towards areas of high acoustic pressure, we asked whether this capability would enable the trapping and spatial patterning of living cells. Considerable interest exists in the use of engineered cells as patterned components of living materials for biomedical uses such as tissue engineering, and as self-healing and actively reconfigurable materials in non-biomedical applications[30,31]. However, few methods exist to dynamically configure the location of cells in 3-D space. In contrast, ARF in the form of engineered standing and traveling waves has been used to create complex 2-D and 3-D arrangements[17,32–35].

We hypothesized that ARF combined with GV expression would allow engineered cells to be patterned in a precise and rapid manner. To test this basic concept, we generated a standing wave pattern of repeating pressure antinodes in a specially designed acoustic chamber by using an unfocused 5 MHz transducer reflected by glass (**Figure 4a**). Imaging the cells using fluorescence microscopy, we observed that engineered cells readily adopted the desired pattern in solution, and that changing the ultrasound frequency allows the spatial pattern of these cells to be dynamically

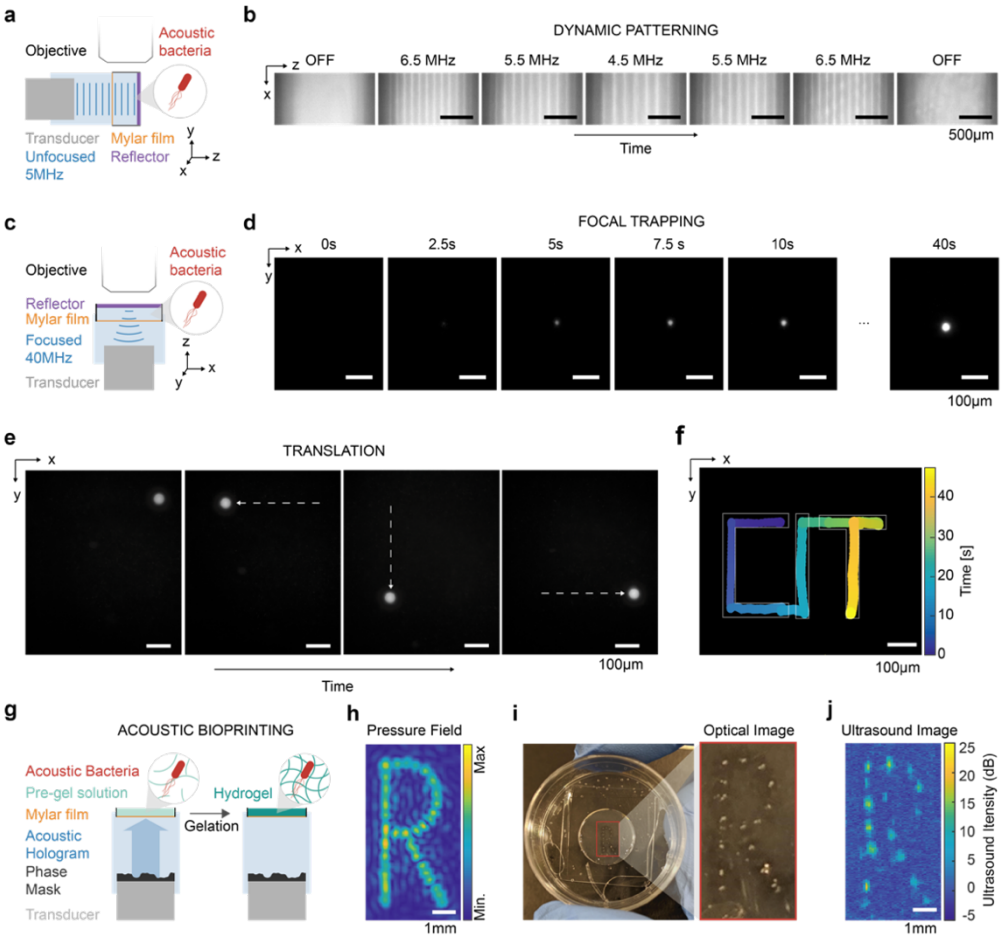

Figure 4 | Dynamic patterning and one-step bioprinting with acoustic bacteria. **(a)** Diagram of the acoustic chamber setup for frequency-controlled spatial patterning. A transducer is aligned orthogonal to a glass reflector using a 3D-printed holder. The sound wave passes through a mylar membrane, is reflected by the glass reflector, and forms a standing wave near the reflector. The sample region containing acoustic *E.coli* is imaged using an epifluorescence microscope. **(b)** Sequential fluorescence images of acoustic *E.coli* in the presence of an acoustic standing wave at varying frequencies. Frequencies were changed every 50 seconds. **(c)** Diagram of the acoustic chamber setup for image-guided trapping and positioning of acoustic *E.coli*. Imaging is performed along the axis of a focused 40 MHz transducer. **(d)** Sequential fluorescence images of the formation of a cluster of acoustic *E.coli* at the ultrasound focus. **(e)** Fluorescence images of a cluster of acoustic *E.coli* positioned at distinct locations in the x-y plane. The positioning is controlled by the translation of the transducer in the x-y plane using a micromanipulator and is guided by real-time fluorescence imaging of the bacteria. **(f)** Overlaid positions of the cell cluster, color-coded by time, to form a spatiotemporal pattern writing out "CIT". **(g)** Diagram of the process for acoustic biofabrication. A transducer and phase mask is aligned such that the acoustic hologram is formed inside the sample chamber containing acoustic *E.coli* suspended in low-melt agarose solution. The gelation of the agarose is triggered to immobilize the acoustically patterned *E.coli*. **(h)** Simulated pressure amplitude generated by the acoustic hologram. **(i)** Acoustically patterned *E.coli* embedded in agarose gel. **(j)** Ultrasound image of acoustically patterned *E.coli*.

reconfigured on the timescale of seconds (**Figure 4b**, **Supplementary Figure 3** and **Supplementary Movie 2**).

Another method of acoustic manipulation involves the confinement of acoustic particles at the focus of an ultrasound transducer[36–39], allowing the particles to be concentrated and transported between discrete locations in space, analogous to an optical trap. To determine whether focal trapping is possible with engineered acoustic cells, we generated a trap using a 40 MHz focused ultrasound transducer reflected on glass (**Figure 4c**). This configuration is expected to exert radial ARF on the cells towards the center of the ultrasound focus. As expected, GV-expressing cells within this acoustic field coalesced into a cellular cluster upon ultrasound application (**Figure 4d** and **Supplementary Movie 3)** and could then be moved around in space by laterally translating the ultrasound transducer, generating a desired spatiotemporal pattern (**Figure 4, e-f** and **Supplementary Movie 4**).

Acoustic manipulation can also be used for rapid fabrication of heterogeneous materials by concentrating acoustic particles in spatial patterns defined by the acoustic field, and subsequently immobilizing the pattern with cross-linking chemistry[17,40–42]. Negative contrast agents have an intrinsic advantage in this application due to their migration to acoustic pressure maxima, which are more easily patterned in complex spatial arrangements.[40] We hypothesized that living materials[30,31] containing GV-expressing acoustic bacteria could be fabricated using this method (**Figure 4g**). To test this possibility, we created an acoustic hologram using a single-element 3.5MHz transducer and a 3D-printed phase mask designed to produce an "R"-shaped pressure profile (**Figure 4h, Supplementary Figure 5**). We applied this hologram to acoustic bacteria suspended in an agarose solution that can be solidified at cold temperatures to form a gel. As expected, the bacteria were immobilized inside the gel in the desired spatial pattern (**Figure 4i**). As an added feature, the spatial distribution of GV-expressing cells could be imaged with ultrasound (**Figure 4j**), providing a means to verify patterning in optically opaque media. These results demonstrate the ability of GVs to enable the acoustic trapping, patterning and dynamic rearrangement of engineered bacteria, and the rapid biofabrication of living materials.

GVs enable selective manipulation of mammalian cells

Having established GVs as a genetically encodable acoustic actuator in bacteria, we examined the ability of GVs to similarly alter the acoustic properties of mammalian cells (**Figure 5a**). To test this concept, we engineered human HEK293T cancer cells to express GVs as part of a chemically inducible genetic program (mARG1)[43] (**Figure 5b**). When we applied ultrasound to these cells in our microfluidic channel under static flow conditions, we observed that a large fraction of the engineered population displayed a negative contrast factor by moving to the pressure antinodes at the channel walls (**Figure 5, c-d**). In contrast, control cells expressing the fluorescent protein mCherry or GV-expressing cells in which

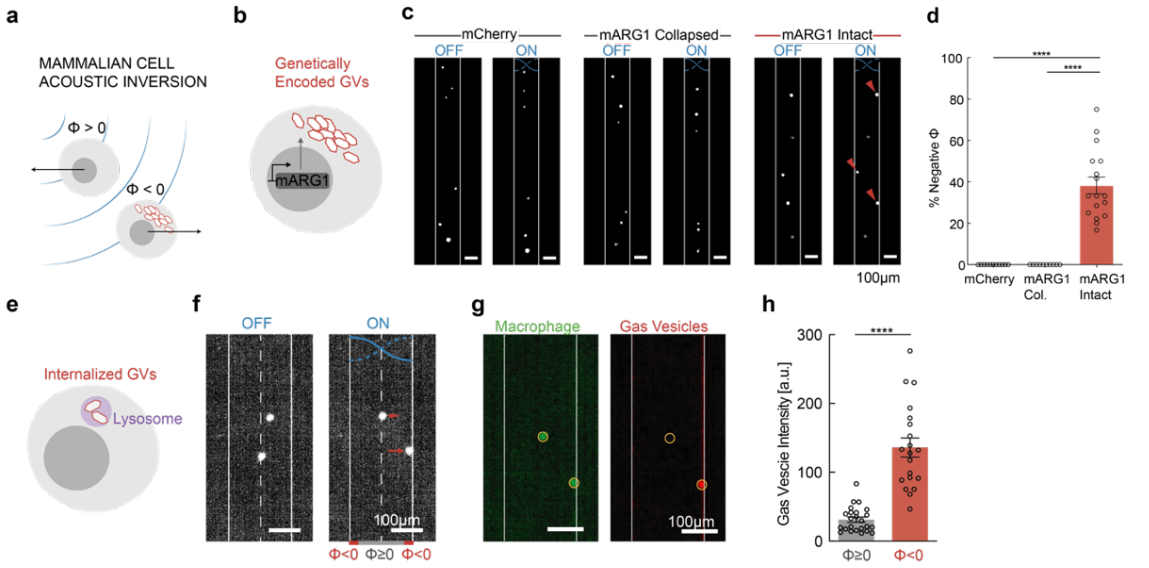

Figure 5 | Gas vesicles invert cellular response to ARF in mammalian cells. (a) Schematic drawing of mammalian cells experiencing an inversion of their acoustic contrast factor due to intracellular GVs. **(b)** Schematic drawing of genetically modified mammalian cells expressing intracellular GVs as mammalian acoustic reporter genes (mARG1). **(c)** Fluorescence images of mammalian cells inside the microfluidic channel with either intact mARG1 GVs, collapsed mARG1 GVs or mCherry, either in the presence or absence of applied ultrasound. **(d)** Percentage of cells that have negative contrast factor with either intact mARG1 GVs (38±4% , n = 17), collapse mARG1 GVs (0%, n = 10), or mCherry (0%, n =11). Mann-Whitney test (****: $p<0.0001$). **(e)** Schematic drawing of GVs internalized in the lysosomal compartment of a mammalian cell. **(f)** Fluorescence images of macrophages with internalized GVs inside the microfluidic channel either in the presence or absence of applied ultrasound. Cells that move to the walls (solid line) have negative contrast factor, while those that move to the center (dashed line) have positive acoustic contrast. **(g)** Images of fluorescence from either macrophages or GVs in the applied acoustic field. Circular ROIs indicate the location of the macrophage. **(h)** Fluorescence intensity of GVs at the location of the macrophages that have either negative or non-negative contrast factors. Mann-Whitney test (****: $p<0.0001$).

GVs were pre-collapsed with hydrostatic pressure migrated to the pressure node in the middle of the channel (**Figure 5, c-d**), as expected from their positive contrast factor.

After demonstrating the ability of GVs to provide mammalian cells with genetically encoded acoustic actuation, we also tested the ability of these biomolecules to serve as externally applied acoustic labels. For this purpose, we incubated fluorescently-tagged GVs with murine macrophages, leading to the endosomal uptake of the GV particles (**Figure 5e**). After applying ultrasound under static flow conditions, we observed that a distinct sub-population of the macrophages moved towards the pressure antinodes, indicating an inversion of their acoustic contrast (**Figure 5f**). Visualizing the separate fluorescence channels corresponding to the macrophages and the GVs revealed that the cells with a negative contrast factor had significantly higher GV content than the positive-contrast cells (**Figure 5, g-h**). In this setting, the GVs enabled mammalian cells to be separated acoustically based on a specific biological function – endocytosis. Taken together, these results demonstrate the ability of GVs to enable selective manipulation of mammalian cells on the basis of gene expression or biological activity.

Gas vesicle ARF-silencing allows multiplexed actuation and *in situ* pressure measurement

Finally, after establishing the basic ability of GVs to respond to ARF and serve as genetically encodable cellular actuators, we examined one additional property of these nanostructures: their ability to be collapsed at specific, tunable acoustic pressures (**Figure 6, a-b**)[9,14]. Since GV collapse causes the rapid dissolution of their gas contents, we hypothesized that *in situ* collapse inside acoustofluidic devices would provide a means to instantaneously convert GVs experiencing ARF into an ARF-silent state. This would provide an additional means to spatially pattern GVs inside microfluidic channels, enable them to serve as probes for *in situ* pressure measurement and be differentially manipulated in space based on their genetically determined collapse pressure thresholds.

To test the ability of GVs to be patterned based on *in situ* collapse, we imaged an engineered variant of Ana GVs (AnaΔC), whose acoustic collapse pressure (**Figure 6b**) has been tuned to be lower than wild-type Ana GVs by removing the outer scaffolding protein GvpC[14]. We applied three different driving voltages to the piezoelectric element coupled to our microfluidic channel while the GV sample was infused into the channel at a steady flow rate, and imaged the steady-state distribution of GVs inside the channel. We predicted

that GVs in regions with acoustic pressures lower than their critical collapse pressure would migrate towards regions of higher pressure due to ARF, while GVs in regions with pressure above their critical threshold would collapse and therefore remain stationary,

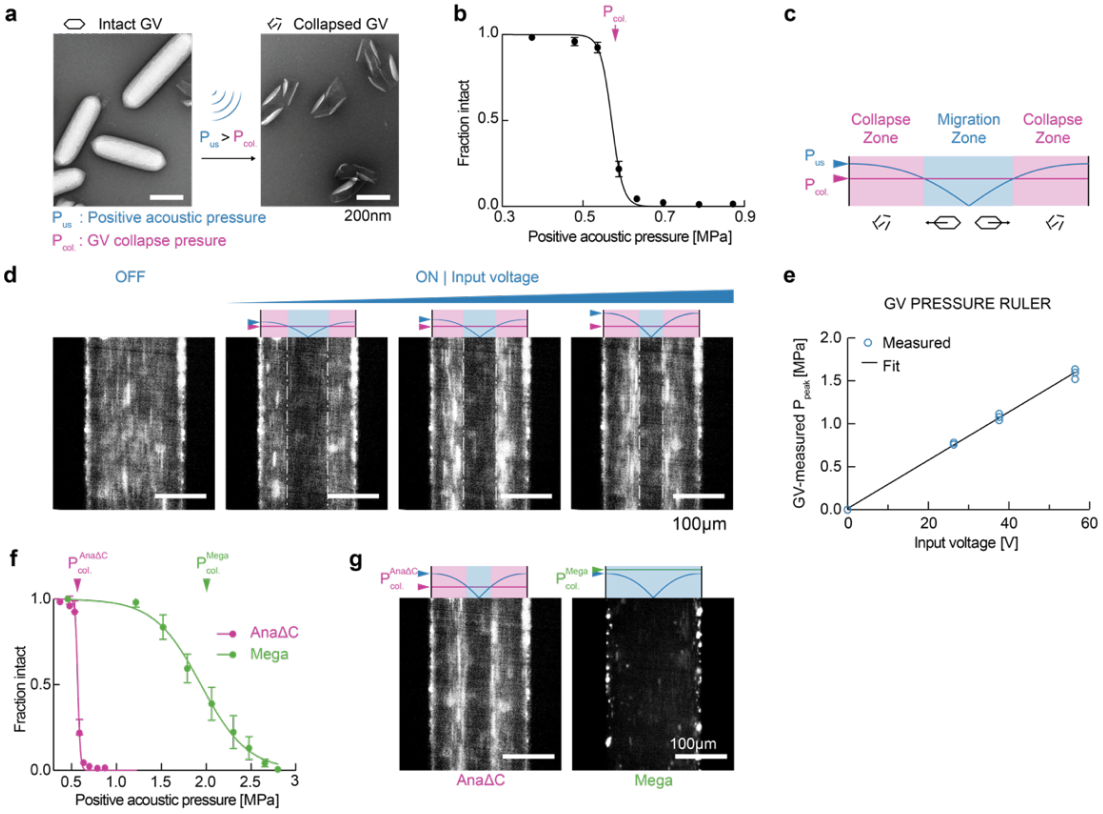

Figure 6 | ARF-silencing of GVs allows *in situ* patterning, pressure sensing and multiplexed acoustic manipulation. **(a)** TEM images of intact and collapsed Ana GVs. Collapse occurs when the positive acoustic pressure exceeds the critical collapse pressure of the GV. **(b)** Acoustic collapse profile of AnaΔC GVs. The critical collapse pressure is determined to be the pressure at which 50% of the GVs have been collapsed. Data adapted from ref.[14]. **(c)** Illustration of the expected behavior of GVs inside a microfluidic channel with a half-wavelength standing wave. GVs in regions with acoustic pressures lower than their critical collapse pressure migrate towards regions of higher pressure due to ARF, while GVs in regions with pressure above their critical threshold collapse and therefore remain stationary. The boundary between laterally migrating and stationary GVs indicates a pressure corresponding to the GVs' critical collapse pressure. P_{US} indicates the temporal peak pressure. **(d)** Fluorescence images of GVs inside a microfluidic channel in the presence of an acoustic field driven with increasing voltage. **(e)** Maximal pressure in the acoustic device as a function of input voltage, determined using videos of the corresponding conditions in (d). **(f)** Acoustic collapse pressure curves of AnaΔC and Mega GVs. Data adapted from refs.[14,46]. **(g)** Fluorescence images of either AnaΔC or Mega GV solutions experiencing the same acoustic field, with the peak driving pressure of 1.2 MPa selected to be above the critical collapse pressure of AnaΔC GVs, but below that of Mega GVs.

resulting in the formation of distinct bands (**Figure 6c**). Indeed, this pattern was observable starting with the lowest applied voltage (**Figure 6d**). As we increased the driving voltage, the location of the material interface shifted toward the middle of the channel, consistent with the expected increase in acoustic pressure across the channel (**Figure 6d** and **Supplementary Movie 5**).

The ability of GVs to assume a pressure-dependent spatial arrangement provides a convenient approach to measuring acoustic pressure inside microfluidic channels. Whereas conventional methods to calibrate such devices by tracking the ARF-induced motion of single-particle standards are laborious[44,45], it is relatively straightforward to locate the boundary between migrating and stationary GVs (**Figure 6c**). Since this boundary corresponds to the GVs' known crucial collapse pressure, and the pressure across the channel follows a known sinusoidal function, imaging the location of GV collapse reveals the standing wave pressure profile inside the channel. This allowed us to easily calibrate the peak acoustic pressure in our acoustofluidic device as a function of the driving voltage (**Figure 6e**).

After demonstrating ARF-silencing of a single GV type, we hypothesized that multiple GV types with different characteristic collapse pressures could be arranged in distinct patterns. Such differential manipulation would be desirable, for example, to enable separate visualization or multiplexed separation of analytes. To test this possibility, we imaged either AnaΔC GVs or heterologously expressed *B. megaterium* GVs (Mega GVs), which have critical collapse pressures of 0.6 MPa and 1.9 MPa, respectively (**Figure 6f**). These GVs in solution were infused into the channel at a steady flow rate and subjected to a standing wave with a maximum acoustic pressure of 1.6 MPa, which should collapse AnaΔC but not Mega GVs. As expected, we observed that the two GV populations followed distinct migration patterns inside the acoustic field (**Figure 6g**). These results demonstrate a unique mode of acoustic manipulation enabled by GVs' genetically engineerable collapse mechanics.

Discussion

Taken together, our results establish GVs as the first genetically encodable biomolecules to enable selective cellular manipulation and patterning with ultrasound. Due to their

unique physical properties, GVs have an exceptionally large, negative acoustic contrast factor in aqueous environments, allowing these nanostructures to experience strong ARF despite their sub-micron size. The expression of GVs inside engineered cells greatly enhances and changes the sign of the force experienced by these cells due to ultrasound, enabling the selective acoustic manipulation and patterning of these cells based on their genotype.

This technology is expected to find applications in several areas of biomaterials and biotechnology. First, the ability of GVs and GV-expressing cells to be patterned and manipulated dynamically in 3-D space will enable the development of protein- and cell-based materials for applications in tissue engineering[2], living materials[30,31], and stimuli-responsive "smart" materials[47]. In these applications, ultrasound has intrinsic advantages compared to optical, magnetic, or printing-based approaches due to its compatibility with opaque media, fine spatial resolution, non-invasive access, simultaneous assembly, and rapid reconfigurability. GV-expressing cells have a unique advantage in such applications due to their negative contrast, simplifying the acoustic field needed for complex patterning. Second, the development of acoustofluidic[7,48] devices combining ultrasound with microfluidic channels creates opportunities for GVs to drive the separation of cells based on their gene expression or other biological activity. In these applications, GVs carry a major advantage over fluorescent proteins. Whereas fluorophores provide no intrinsic actuation capability – requiring a separate mechanical step after a fluorescent readout as done one cell at a time in fluorescence-activated cell sorting – the expression or uptake of GVs provides a direct handle for selective acoustic manipulation. This allows cellular patterning or separation to be done *en masse*.

The ability of GVs to connect an acoustophoretic phenotype to the output of genetic circuits in both bacterial and mammalian cells will allow their expression to designate specific cells for separation, trapping, and patterning using ultrasound. Both endogenous and engineered promoters can be connected to gene expression, allowing the formation of GVs to indicate a wide variety of cellular states, based on which the cells can now be selectively manipulated. Alternatively, GVs can be used as exogenous cellular labels. To this end, GVs are readily functionalized with moieties providing the ability to bind specific biomolecular targets[9,14]. In addition, compared to synthetic materials used to externally functionalize cells for acoustic manipulation[22,23], the ability of GVs to be internalized by

mammalian cells to enable selective actuation, and subsequently be lysosomally degraded by the same cells, could provide a unique strategy for "traceless" labeling and cellular actuation.

These capabilities for selective actuation could be extended from *in vitro* devices to inside living animals or patients using emerging approaches for *in vivo* ARF[49]. In addition, GVs could be used as a nanoscale actuator to locally apply specific forces to biological systems. The fN to low pN forces that can be achieved by GVs, while not sufficient to rupture cells[50], are comparable to forces in processes such as cell-matrix adhesion and the gating of ion channels[28], which may be useful for studies of mechanosensation or for engineered mechanisms of non-invasive cellular control[6].

Additional studies are needed to fully characterize and further expand the capabilities of GVs as transducers of ARF. First, it will be useful to build on the fundamental demonstrations in this work by applying GVs to specific biological problems, taking advantage of their potential for biomolecular and genetic engineering. Second, while the basic gradient trapping of GVs and engineered cells is expected to generalize to more complex acoustic fields, it would be useful to test the acoustic manipulation of these objects using traveling acoustic waves to overcome the need for acoustic reflectors[38]. Third, the theoretical model of GV acoustic contrast could be improved to provide more detailed insights. The calculations performed in this study approximated that GVs have spherical geometry and that their shell has a constant density and compressibility as a function of applied acoustic pressure. In reality, GVs are anisotropic cylindrical nanostructures that can undergo reversible buckling under applied acoustic pressure[51,52]. This buckling behavior is expected to enhance the effective compressibility of GVs and thereby the ARF they experience. Theoretical analysis of GV ARF with more realistic geometry and experiments using a broader range of pressures encompassing the buckling regime could inform the engineering and use of these biomolecules in ARF applications. Fourth, it will be useful to explore the inter-particle interactions arising between GVs and GV-expressing cells in an applied acoustic field, as this may influence their clustering, separation, and motion. Fifth, while acoustic streaming was not a major factor under the acoustic conditions used in our study, it would be useful to examine the interaction of GV ARF and acoustic streaming at higher acoustic frequencies and pressures.[32] Based on these additional physical insights, it may be possible to genetically engineer new GV phenotypes with size, shape, and

mechanical properties enhancing their exceptional response to ARF and further propelling the fantastic voyage of engineered molecules and cells in biomedicine and biomaterials.

Methods

Estimation of acoustic contrast factor. Acoustic contrast factors were calculated using the equation:

$$\phi = \frac{1}{3}\left[\frac{5\rho_p - 2\rho_0}{2\rho_p + \rho_0} - \frac{\beta_p}{\beta_0}\right] \quad [1]$$

where ρ_p and ρ_0 are the density of the particle and the fluid, respectively, β_p and β_0 the compressibility of the particle and the fluid, respectively. Values of ρ_p and β_p for GVs were obtained from literature [15,16]. Values of ρ_p and β_p for the acoustic *E.coli* were obtained by assuming that 10% of the intracellular space was occupied by GVs[13], and calculating the volume-averaged density and compressibility according to $\rho_{acoustic\ cell} = 0.9\ \rho_{wildtype\ cell} + 0.1\ \rho_{GV}$ and $\beta_{acoustic\ cell} = 0.9\ \beta_{wildtype\ cell} + 0.1\ \beta_{GV}$. The assumption of 10% was based on the GV occupancy needed for cells to have a density less than water, which provided a lower-bound on the GV expression for the cell population that we enriched using centrifugation.

Preparation of gas vesicles. GVs from *Anabaena flos-aquae* (Ana), *Bacillus megaterium* (Mega), and Ana GVs with GvpC removed (AnaΔC) were prepared as previously described.[53] Dylight415-Co1 N-hydroxysuccinimide ester (Thermo Fisher Scientific) was reacted with GVs in PBS for 2 hours at 10,000:1 molar ratio, protected from light, on a rotating rack. 10 mM Tris buffer was then added to the solution to quench unreacted dye. Labeled GVs were subjected to dialysis and buoyancy purification. Pre-collapsed GVs controls were prepared by application of hydrostatic pressure in a capped syringe. The acoustic collapse profiles of GVs were characterized as previously described[14]. Briefly, GVs embedded in an ultrasound phantom was imaged using ultrasound after subjecting the sample to increasing acoustic pressure. The fraction intact was calculated from the ultrasound image intensity of the sample at each pressure step normalized to the initial sample intensity.

Preparation of acoustic *E.coli.* GV-expressing cells were produced by transforming a pET28a plasmid containing the bARG1 gene cluster[13] (Addgene #106473) into BL21(A1) *E. coli* (Thermo Fisher Scientific). The transformed cells were first grown overnight at 37 °C in LB media supplemented with 1% glucose, and subsequently diluted 1:100 into LB media supplemented with 0.2% glucose. When the optical density at 600 nm (OD600) of the culture reached between 0.4 and 0.6, 400 μM IPTG and 0.5% l-arabinose were added to induce the expression of GVs. The expression proceeded at 30 °C for 22 hours. High-expressing cells were enriched by centrifugation-assisted floatation at 300 g. Cell density was measured after collapsing any intracellular GVs to eliminate their contribution to optical scattering. *E.coli* with pre-collapsed GVs were prepared by application of hydrostatic pressure to the cell culture in a capped syringe. Fluorescently labeled bacteria were prepared by incubating the cells with 10 μM of Baclight Green bacterial stain (Thermo Fisher Scientific) for 40 minutes at room temperature, protected from light, and followed by two rounds of buoyancy purification to remove excess dye. *E.coli* Nissle 1917 cells were transformed by electroporation of the bARG1 gene under the T5 promoter. Transformed cells were cultured similar to above and were either induced with 3μM IPTG or grown without induction. Induced and noninduced cells were labeled with 10μM of Baclight Green and Baclight Red bacterial stain, respectively, and excess dye was removed using 2 rounds of dialysis with 6-8kD dialysis tubing (Spectrum Labs).

Preparation of acoustic mammalian cells. HEK293T cells containing mARG1 or mCherry driven by the Tetracycline-inducible promoter were cultured in DMEM supplemented with 10% Tetracycline-free FBS and Penicillin/Streptomycin, and induced with 1μg/mL Doxycycline and 5mM Sodium Butyrate for 12 days. Special care was taken to prepare fresh induction media every day. Cells were harvested by trypsinization, resuspended in PBS supplemented with 2% FBS and 100μL/mL DNase, filtered through a 40-μm cell strainer, and introduced into the microfluidic device.

RAW264.7 cells constitutively expressing GFP were seeded on Fibronectin-coated glass coverslips and cultured in DMEM with 10% FBS and Penicillin/Streptomycin. When the cells reached 70-80% confluency, the coverslip was washed with PBS, and placed upside

down onto a 300μL droplet of DMEM containing fluorescently labeled GVs, allowing the GVs to float towards the cells. The cells were incubated with the GV solution at 37°C for 1 hour, washed with PBS, trypsinized, resuspended in PBS with 2% FBS and 100μL/mL DNase, filtered through a 40-μm cell strainer, and introduced into the microfluidic device.

Acoustofluidic setup. The acoustofluidic channel was designed in SolidWorks, and fabricated in a clean room facility following a protocol modified from one previously described[54]. Briefly, AZ1518 positive photoresist (Merck) was patterned onto a <100> silicon wafer (University Wafer) using a photomask, and developed in AZ340 solution. Fifty cycles of deep-reactive ion etching (PlasmaTherm, SLR Series) were used to etch the channels into the wafer. The channel depth was measured using a profilometer (P15, KLA-Tencor). The photoresist was then removed, and the wafer was cleaned with piranha solution. A Borofloat 33 borosilicate glass wafer was anodically bonded to the silicon overnight at 500V, 400°C using a custom setup. Inlet holes were drilled through the glass layer using a diamond drill bit (Drilax) and joined with microfluidic connectors (Idex Health & Science) using Epoxy (Gorilla). A custom PZT-5A piezoelectric element (American Piezo Company) was attached to the silicon beneath the channel using cyanoacrylate (Loctite). The input signal to the PZT was programmed in MATLAB and generated using an arbitrary waveform generator (Tabor Electronics). The output waveform was validated by an oscilloscope (Keysight Technologies) before being amplified by an RF power amplifier (Amplifier Research) and connected to the PZT. The samples inside the channel were imaged using a custom-built upright epifluorescence microscope with an LED source (Thorlabs) and a sCMOS camera (Zyla 5.5, Andor).

Single-particle tracking experiment and analysis. Fluorescently labeled GVs, suspended in buffer (DI water, 0.01% v/v Tween-20), were introduced into the acoustofluidic channel via a syringe. The background flow was naturally slowed until particles stayed within the field of view longer than the acquisition time of approximately 2 minutes. The particles were then imaged at 20 frames per second for approximately 20 seconds before ultrasound was turned on. The ultrasound was then turned on (3.75 ± 0.1MHz sweep, 1 ms sweep

repetition time, 3.8V peak-to-peak, continuous wave) for approximately 100 seconds. Pressure-collapsed GVs, and 200-nm diameter fluorescent polystyrene particles (Thermo Fisher Scientific) were subjected to the same procedure.

Particle detection was performed in ImageJ using the MOSAIC ParticleTracker plugin to obtain time-dependent particle coordinates in the direction towards the walls, $x(t)$. Particle trajectories were exported and analyzed in MATLAB using custom scripts. The coordinates were split into before-ultrasound and during-ultrasound groups. Only particles with trajectories in both groups were included in the analysis.

Trajectories during the Brownian period were used to calculate the mean-squared-displacement, $< \Delta x >^2$, for different time durations, Δt. Linear regression was used to extract the diffusion coefficient, D, for each particle following the one-dimensional diffusion relationship $< \Delta x >^2 = 2D\Delta t$. The mobility, μ, of the particle was then obtained using the Einstein relation:

$$D = \mu k_B T \quad [2]$$

where k_B is the Boltzmann constant, and T the temperature.

Trajectories recorded during the ultrasound period were fitted to an equation of motion accounting for the sinusoidal pressure profile to obtain the peak particle velocity in the acoustic field. Given the profile of the pressure in the channel $P(x,t) = P_{peak}\cos(kx)\sin(\omega t)$, where k is the wave number and ω the angular frequency, the radiation force, F_{ARF}, acting on the particles is:

$$F_{ARF} = 4\pi a^3 \phi k E_{ac} sin(2kx) = F_{peak}\sin(2kx) \quad [3]$$

here a is the particle radius, ϕ the acoustic contrast factor, $E_{ac} = \frac{1}{4}{P_{peak}}^2 * \beta_0$ the acoustic energy density, and F_{peak} the peak ARF[24].

At low Reynolds number, $F_{ARF} = F_{drag} \propto v_p$, where F_{drag} is the drag force and v_p the particle velocity. Therefore, $v_p = v_{peak} \sin(2kx)$, where v_{peak} is the peak particle velocity. The particle position, $x_p(t)$, over time within an acoustic field is thus related to the peak velocity by:

$$x_p(t) = \frac{1}{k} cot^{-1}\left[\cot(x(0)k)\ \exp\left(2ktv_{peak}\right)\right] \quad [4]$$

Fitting the particle trajectory to this equation allowed us to obtain v_{peak}. Combining the particle mobility μ and the peak velocity v_{peak}, the peak ARF was calculated using $\mu = \frac{v_{peak}}{F_{peak}}$.

The hydrodynamic radius a_H of the particles was determined using the Stokes-Einstein equation:

$$D = \frac{k_B T}{6\pi\eta a_H} \quad [5]$$

where η is the solution viscosity. Fitting the force measurements to a fractal clustering model[26,27]

$$F_{peak} = m{a_H}^n \quad [6]$$

to obtain the scaling coefficient m, and the force-mobility exponent n, the peak ARF for a single GV, F_{peak_sGV}, was calculated by substituting the average hydrodynamic radius of a GV[53], $a_{H\_sGV} = 125\, nm$. The acoustic contrast factor of a single GV, ϕ_{sGV}, was then obtained using the equation:

$$F_{peak_{sGV}} = 4\pi\phi_{sGV}ka^3_{H_{sGV}}E_{ac} \quad [7]$$

where E_{ac} is the acoustic energy density of the applied ultrasound, as determined by a separate calibration. Finally, this equation is used to predict the peak ARF for a single GV at various acoustic parameters.

Fluorescently labeled acoustic *E.coli* cells were suspended in PBS and subjected to the same ultrasound procedure as the GV particles. The hydrodynamic radius of *E.coli* was determined using the Stokes-Einstein equation (Eq. 5), and the acoustic contrast factor was determined using the acoustophoretic motion of the *E.coli* in a similar manner as described for GVs.

Acoustic GV collapse in microfluidic channel. A syringe pump was used to introduce fluorescently labeled AnaΔC GVs into the acoustofluidic chip at a controlled flow rate of 0.5 µl/min. Fluorescence images were acquired while the PZT was driven at three different voltages. The acoustic energy density for the three trials was kept constant by choosing the appropriate duty cycle according to $Duty\ Cycle\ *\ Voltage^2 = constant$. A video of the steady-state pattern was acquired and projected onto the x-axis to determine the locations of the discontinuity in the fluorescence signal. The location was marked with the critical collapse pressure of AnaΔC of 0.6 MPa, and the acoustic pressure in the entire channel was calculated by assuming a sinusoidal pressure profile with antinodes at each wall.

Fluorescently labeled Mega GVs were introduced into the channel in a similar manner and subjected an acoustic field with a peak acoustic pressure of 1.2 MPa, as measured using the collapse profile of AnaΔC.

Acoustic manipulation of cells in microfluidic channel. Fluorescently labeled *arg1*-expressing *E. coli* and pre-collapsed controls, prepared as described above, were suspended in PBS and loaded into the acoustofluidic channel described above. Continuous wave ultrasound was applied at 3.75 MHz, 7.6 V peak-to-peak. Images of the channel were acquired for 10 seconds during ultrasound application as described above.

Dynamic patterning of acoustic bacteria. An acoustic setup was built to generate a standing wave with reconfigurable wavelengths, by reflecting the sound generated by a single-element transducer (V310, Olympus) off a glass coverslip (VWR). A holder was designed in SolidWorks and 3D-printed (3D Systems) to facilitate the alignment of the transducer with the reflector and to create a sample chamber sandwiched between the reflector and an acoustically transparent mylar membrane (Chemplex, 2.5 μM thickness). The acoustic setup was placed into a water bath to provide acoustic coupling between the transducer and the sample chamber, and fluorescently labeled *arg1*-expressing *E. coli* prepared as above were suspended in PBS and loaded into the sample chamber. Ultrasound (continuous wave) was applied to the sample, and fluorescent images were acquired with the imaging plane parallel to the sound propagation axis. The ultrasound frequency was varied between 4.5 and 6.5 MHz in 1 MHz steps every 50 seconds.

Image-guided positioning of acoustic bacteria. For radial acoustic trapping and movement, a sample dish was created allowing the placement of the image plane orthogonal to the sound propagation axis. The glass bottom of a 35-mm glass-bottom petri dish (Matsunami) was removed using a glass cutter and replaced with a Mylar film. *arg1*-expressing *E. coli* prepared as above and suspended in PBS were added to the center of the dish, and sealed using a glass coverslip. A 40 MHz focused single-element transducer (V390-SU/RM, Olympus) was mounted onto a micromanipulator and positioned beneath the dish. To align the transducer with the glass reflector, the transducer first emitted 5-cycle pulses and received the echo from the glass coverslip. The amplitude of this echo was maximized by adjusting the position of the transducer using the micromanipulator. To trap the acoustic bacteria, the transducer was then driven with a continuous wave 40 MHz input while fluorescent images were acquired. After a cell cluster was formed in the center of the acoustic focus (**Supplementary Figure 4**), the transducer was moved in the x-y plane using the micromanipulator, guided by the optical image, to form the desired positioning sequence.

Acoustic Biofabrication

Acoustic phase masks were designed in MATLAB using the iterative angular spectrum approach, 3D printed in VeroClear using a PolyJet printer (Stratasys), coupled to a 3.5MHz unfocused transducer (Olympus), and positioned in a water bath below a Petri dish holder. Acoustic bacteria was suspended in 0.25% low-melt agarose solution (GoldBio) supplemented with 20mg/mL LB medium, and maintained at 37°C using a heat block to prevent gelation. The bacteria solution was added onto a mylar-bottom petri dish described above, which is then placed into the Petri dish holder above the phase mask. Ultrasound was applied while the agarose solution cooled to its gelation temperature of 26°C. The acoustically fabricated material was then imaged using a cell phone camera and ultrasound imaging.

Statistical analysis. Statistical methods are described in each applicable figure caption. Measured values are stated in the text as the mean ± the standard error of the mean. Standard error propagation methods were used where appropriate.

References

1. Wu, D. *et al.* Genetically encoded nanostructures enable acoustic manipulation of engineered cells. *bioRxiv* 691105 (2019) doi:10.1101/691105.
2. Moroni, L. *et al.* Biofabrication strategies for 3D in vitro models and regenerative medicine. *Nature Reviews Materials* vol. 3 21–37 (2018).
3. Mura, S., Nicolas, J. & Couvreur, P. Stimuli-responsive nanocarriers for drug delivery. *Nat. Mater.* **12**, 991–1003 (2013).
4. Deisseroth, K. Optogenetics. *Nat. Methods* **8**, 26–29 (2011).
5. Piraner, D. I. *et al.* Going Deeper: Biomolecular Tools for Acoustic and Magnetic Imaging and Control of Cellular Function. *Biochemistry* **56**, 5202–5209 (2017).
6. Maresca, D. *et al.* Biomolecular Ultrasound and Sonogenetics. *Annu. Rev. Chem. Biomol. Eng.* **9**, 229–252 (2018).
7. Ozcelik, A. *et al.* Acoustic tweezers for the life sciences. *Nature Methods* vol. 15 1021–1028 (2018).
8. Walsby, A. E. Gas vesicles. *Microbiol. Rev.* **58**, 94–144 (1994).
9. Shapiro, M. G. *et al.* Biogenic gas nanostructures as ultrasonic molecular reporters. *Nat. Nanotechnol.* **9**, 311–316 (2014).
10. Shapiro, M. G. *et al.* Genetically encoded reporters for hyperpolarized xenon magnetic resonance imaging. *Nat. Chem.* **6**, 629–634 (2014).

11. Lu, G. J. *et al.* Acoustically modulated magnetic resonance imaging of gas-filled protein nanostructures. *Nat. Mater.* **17**, 456–463 (2018).

12. Lu, G. J. *et al.* Genetically Encodable Contrast Agents for Optical Coherence Tomography. *ACS Nano* acsnano.9b08432 (2020) doi:10.1021/acsnano.9b08432.

13. Bourdeau, R. W. *et al.* Acoustic reporter genes for noninvasive imaging of microorganisms in mammalian hosts. *Nature* **553**, 86–90 (2018).

14. Lakshmanan, A. *et al.* Molecular Engineering of Acoustic Protein Nanostructures. *ACS Nano* **10**, 7314–7322 (2016).

15. Walsby, A. E. & Bleything, A. The Dimensions of Cyanobacterial Gas Vesicles in Relation to Their Efficiency in Providing Buoyancy and Withstanding Pressure. *Microbiology* **134**, 2635–2645 (1988).

16. Walsby, A. E. The elastic compressibility of gas vesicles. *Proc. R. Soc. London - Biol. Sci.* **216**, 355–368 (1982).

17. Melde, K., Mark, A. G., Qiu, T. & Fischer, P. Holograms for acoustics. *Nature* **537**, 518–522 (2016).

18. Petersson, F., Nilsson, A., Holm, C., Jönsson, H. & Laurell, T. Separation of lipids from blood utilizing ultrasonic standing waves in microfluidic channels. *Analyst* **129**, 938–943 (2004).

19. Petersson, F., Nilsson, A., Holm, C., Jönsson, H. & Laurell, T. Continuous separation of lipid particles from erythrocytes by means of laminar flow and acoustic standing wave forces. *Lab Chip* **5**, 20–22 (2005).

20. Johnson, L. M. *et al.* Elastomeric microparticles for acoustic mediated bioseparations. *J. Nanobiotechnology* **11**, (2013).

21. Cushing, K. W. *et al.* Elastomeric negative acoustic contrast particles for affinity capture assays. *Anal. Chem.* **85**, 2208–2215 (2013).

22. Shields, C. W., Johnson, L. M., Gao, L. & López, G. P. Elastomeric negative acoustic contrast particles for capture, acoustophoretic transport, and confinement of cells in microfluidic systems. *Langmuir* **30**, 3923–3927 (2014).

23. Kokhuis, T. J. A. *et al.* Intravital microscopy of localized stem cell delivery using microbubbles and acoustic radiation force. *Biotechnol. Bioeng.* **112**, 220–227 (2015).

24. Bruus, H. Acoustofluidics 7: The acoustic radiation force on small particles. *Lab on a Chip* vol. 12 1014–1021 (2012).

25. Barnkob, R., Augustsson, P., Laurell, T. & Bruus, H. Acoustic radiation- and streaming-induced microparticle velocities determined by microparticle image velocimetry in an ultrasound symmetry plane. *Phys. Rev. E - Stat. Nonlinear, Soft Matter Phys.* (2012) doi:10.1103/PhysRevE.86.056307.

26. Sorensen, C. M. The mobility of fractal aggregates: A review. *Aerosol Science and Technology* vol. 45 755–769 (2011).

27. Johnson, C. P., Li, X. & Logan, B. E. Settling velocities of fractal aggregates. *Environ. Sci. Technol.* **30**, 1911–1918 (1996).

28. Roca-Cusachs, P., Conte, V. & Trepat, X. Quantifying forces in cell biology. *Nature Cell Biology* vol. 19 742–751 (2017).

29. Van Assche, D. *et al.* Gradient acoustic focusing of sub-micron particles for separation of bacteria from blood lysate. *Sci. Rep.* **10**, 3670 (2020).

30. Nguyen, P. Q., Courchesne, N. M. D., Duraj-Thatte, A., Praveschotinunt, P. & Joshi, N. S. Engineered Living Materials: Prospects and Challenges for Using Biological Systems to Direct the Assembly of Smart Materials. *Advanced Materials* vol. 30 1704847 (2018).

31. Gilbert, C. & Ellis, T. Biological Engineered Living Materials: Growing Functional Materials with Genetically Programmable Properties. *ACS Synth. Biol.* **8**, 1–15 (2019).

32. Li, H., Friend, J. R. & Yeo, L. Y. Microfluidic colloidal island formation and erasure induced by surface acoustic wave radiation. *Phys. Rev. Lett.* **101**, (2008).

33. Collins, D. J. *et al.* Two-dimensional single-cell patterning with one cell per well driven by surface acoustic waves. *Nat. Commun.* **6**, (2015).

34. Marzo, A. & Drinkwater, B. W. Holographic acoustic tweezers. *Proc. Natl. Acad. Sci.* (2018) doi:10.1073/pnas.1813047115.

35. Kang, B. *et al.* High-resolution acoustophoretic 3D cell patterning to construct functional collateral cylindroids for ischemia therapy. *Nat. Commun.* **9**, 5402 (2018).

36. Wu, J. R. Acoustical tweezers. *J. Acoust. Soc. Am.* **89**, 2140–3 (1991).

37. Lee, J. *et al.* Single beam acoustic trapping. *Appl. Phys. Lett.* **95**, 073701 (2009).

38. Baresch, D., Thomas, J. L. & Marchiano, R. Observation of a Single-Beam Gradient Force Acoustical Trap for Elastic Particles: Acoustical Tweezers. *Phys. Rev. Lett.* (2016) doi:10.1103/PhysRevLett.116.024301.

39. Marzo, A. *et al.* Holographic acoustic elements for manipulation of levitated objects. *Nat. Commun.* **6**, 8661 (2015).

40. Melde, K. *et al.* Acoustic Fabrication via the Assembly and Fusion of Particles. *Adv. Mater.* **30**, (2018).

41. Ma, Z. *et al.* Acoustic Holographic Cell Patterning in a Biocompatible Hydrogel. *Adv. Mater.* 1904181 (2019) doi:10.1002/adma.201904181.

42. Cheng, K. W. *et al.* Fast three-dimensional micropatterning of PC12 cells in rapidly crosslinked hydrogel scaffolds using ultrasonic standing waves. *Biofabrication* **12**, 015013 (2020).

43. Farhadi, A., Ho, G. H., Sawyer, D. P., Bourdeau, R. W. & Shapiro, M. G. Ultrasound imaging of gene expression in mammalian cells. *Science (80-.).* **365**, 1469–1475 (2019).

44. Barnkob, R., Augustsson, P., Laurell, T. & Bruus, H. Measuring the local pressure amplitude in microchannel acoustophoresis. *Lab Chip* **10**, 563–570 (2010).

45. Augustsson, P., Barnkob, R., Wereley, S. T., Bruus, H. & Laurell, T. Automated and temperature-controlled micro-PIV measurements enabling long-term-stable

microchannel acoustophoresis characterization. *Lab Chip* **11**, 4152–4164 (2011).

46. Farhadi, A. *et al.* Recombinantly expressed gas vesicles as nanoscale contrast agents for ultrasound and hyperpolarized MRI. *AIChE J.* **64**, 2927–2933 (2018).

47. Badeau, B. A. & DeForest, C. A. Programming Stimuli-Responsive Behavior into Biomaterials. *Annu. Rev. Biomed. Eng.* **21**, 241–265 (2019).

48. Lenshof, A., Magnusson, C. & Laurell, T. Acoustofluidics 8: Applications of acoustophoresis in continuous flow microsystems. *Lab Chip* **12**, 1210–1223 (2012).

49. Dayton, P., Klibanov, A., Brandenburger, G. & Ferrara, K. Acoustic radiation force in vivo: A mechanism to assist targeting of microbubbles. *Ultrasound Med. Biol.* **25**, 1195–1201 (1999).

50. Gonzalez-Rodriguez, D. *et al.* Mechanical Criterion for the Rupture of a Cell Membrane under Compression. *Biophys. J.* **111**, 2711–2721 (2016).

51. Maresca, D. *et al.* Nonlinear ultrasound imaging of nanoscale acoustic biomolecules. *Appl. Phys. Lett.* **110**, 073704 (2017).

52. Cherin, E. *et al.* Acoustic Behavior of Halobacterium salinarum Gas Vesicles in the High-Frequency Range: Experiments and Modeling. *Ultrasound Med. Biol.* **43**, 1016–1030 (2017).

53. Lakshmanan, A. *et al.* Preparation of biogenic gas vesicle nanostructures for use as contrast agents for ultrasound and MRI. *Nat. Protoc.* (2017) doi:10.1038/nprot.2017.081.

54. Shields, C. W. *et al.* Fabrication and Operation of Acoustofluidic Devices Supporting Bulk Acoustic Standing Waves for Sheathless Focusing of Particles. *J. Vis. Exp.* (2016) doi:10.3791/53861.

Supplementary Information

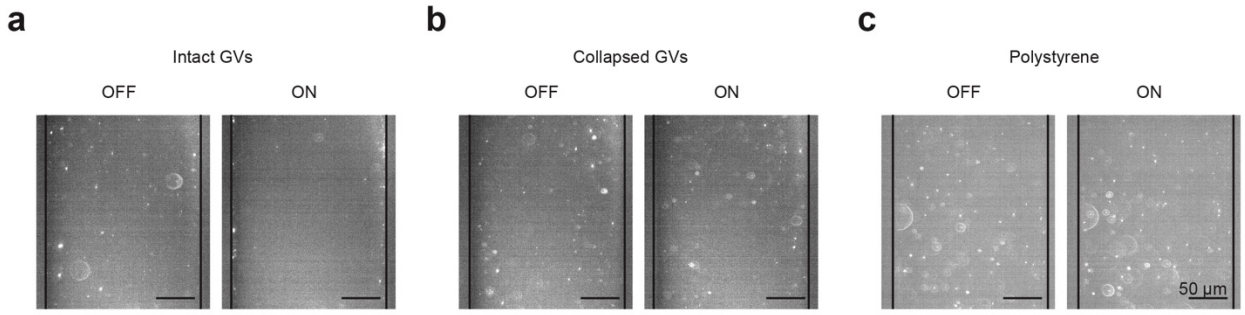

Supplementary Figure 1 | Control particles do not experience substantial ARF. Fluorescence images of intact GVs (**a**) pressure-collapsed GVs (**b**) and polystyrene nanoparticles (**c**) inside the microfluidic channel before ultrasound (OFF) and 100 seconds after ultrasound has been turned on (ON). Device and acoustic conditions are as described in Figure 2.

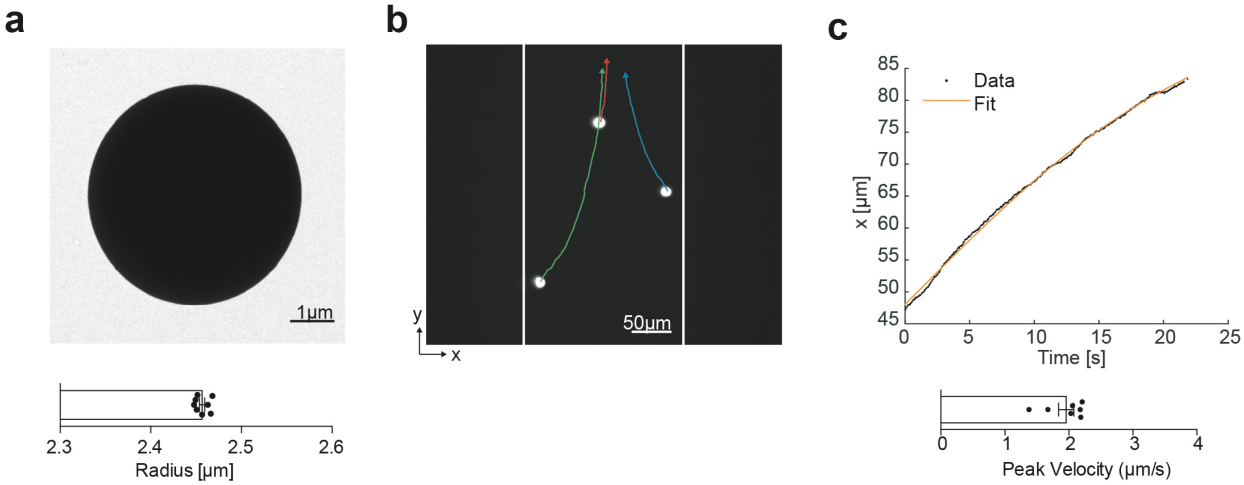

Supplementary Figure 2 | Calibration of the acoustic energy inside the acoustofluidic channel. (a) Representative TEM image of a polystyrene particle (top) and quantification of the particle radius (bottom, 2.457±0.003 µm, mean±S.E.M., n=7). **(b)** Fluorescence image and overlaid acoustophoretic trajectory of polystyrene particles inside the acoustofluidic channel. The white lines demarcate the edges of the channel. Arrows indicated direction of particle movement. **(c)** Representative single-particle trajectory in the *x*-direction during ultrasound stimulation (top), and quantification of the peak particle velocity (bottom, 2.0±0.1 µm/s, mean±S.E.M., n=7). The acoustic energy is determined using the radius, peak velocity, and the acoustic contrast factor of polystyrene particles (**Figure1e**)

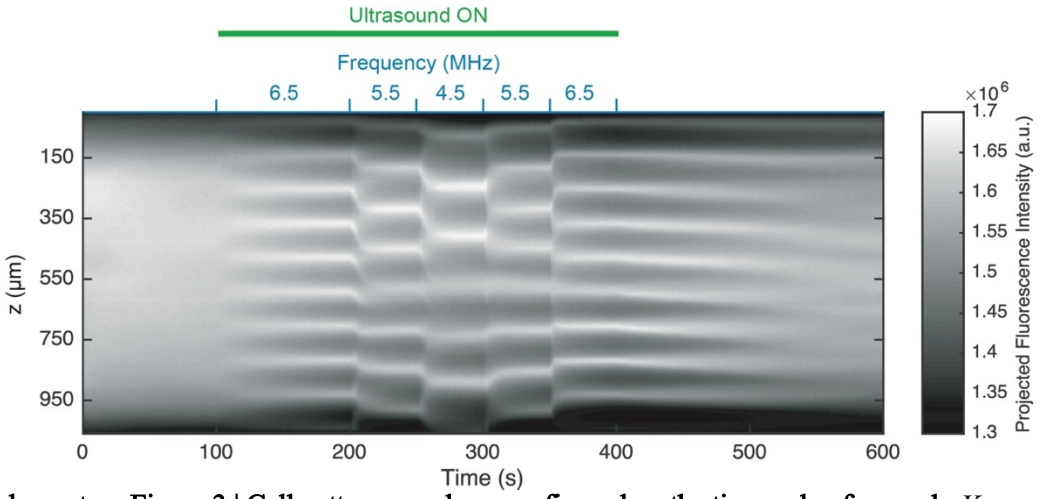

Supplementary Figure 3 | Cell patterns can be reconfigured on the timescale of seconds. Kymograph of projected fluorescence signal from *arg1*-expressing *E.coli* during the application of ultrasound at different ultrasound frequencies. Conditions as described in Figure 5, a-b.

Supplementary Figure 4 | Bacteria cluster formation requires intact intracellular GVs. Fluorescence images of *arg1*-expressing *E.coli* with intact (+) and collapsed (-) intracellular GVs before and 40 seconds after ultrasound application.

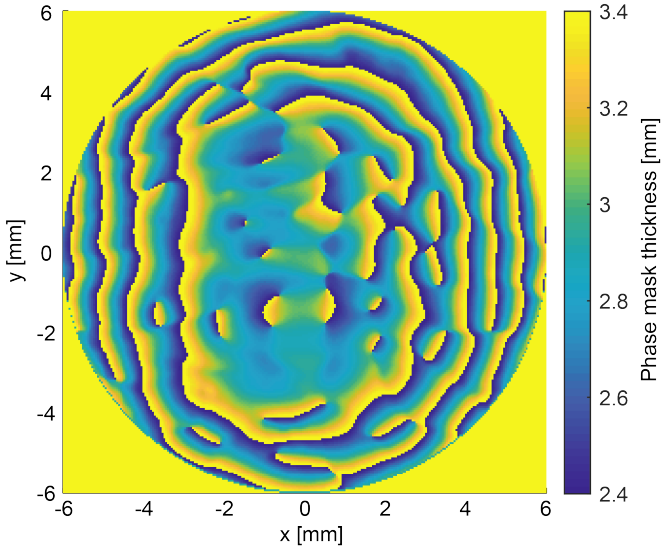

Supplementary Figure 5 | Hologram phase mask. Thickness map of the 3D-printed phase mask designed to produce an "R"-shaped pressure profile.

Chapter 3

NON-INVASIVE IMAGING USING REPORTER GENES ALTERING CELLULAR WATER PERMEABILITY

This chapter is in large part a reformatted version of the manuscript entitled " Non-invasive imaging using reporter genes altering cellular water permeability" published by Mukherjee, A.*, Wu, D.*, Davis H.C., and Shapiro M.G., in *Nature Communications*[70]. Under the supervision of Mikhail Shapiro, my contributions to the work was to help design and conduct the experiments in addition to analyzing and interpreting the data, in particular, experiments related to the demonstration of aquaporins as a reporter gene *in vivo.*

Abstract

Noninvasive imaging of gene expression in live, optically opaque animals is important for multiple applications, including monitoring of genetic circuits and tracking of cell-based therapeutics. Magnetic resonance imaging (MRI) could enable such monitoring with high spatiotemporal resolution. However, existing MRI reporter genes based on metalloproteins or chemical exchange probes are limited by their reliance on metals or relatively low sensitivity. Here we introduce a new class of MRI reporters based on the human water channel aquaporin 1. We show that aquaporin overexpression produces contrast in diffusion-weighted MRI by increasing tissue water diffusivity without affecting viability. Low aquaporin levels or mixed populations comprising as few as 10% aquaporin-expressing cells are sufficient to produce MRI contrast. We characterize this new contrast mechanism through experiments and simulations, and demonstrate its utility *in vivo* by imaging gene expression in tumors. Our results establish an alternative class of sensitive, metal-free reporter genes for noninvasive imaging.

Introduction

The ability to image gene expression within the context of living mammalian organisms is critical for basic biological studies and the development of cellular and genetic therapeutics. However, most genetically encoded reporters, based on fluorescent and luminescent proteins[1-3] have limited utility in this context due to the poor penetration of light into deep tissues[4, 5]. In contrast to optical techniques, magnetic resonance imaging (MRI) enables the

acquisition of *in vivo* images with excellent depth penetration and high spatial and temporal resolution. Consequently, there is intense interest in the development of genetically encoded reporters for MRI[6-26]. Previous efforts to develop such reporters have focused primarily on two classes of proteins. In one class, metalloproteins and metal ion transporters are overexpressed to enrich the paramagnetic content of cells, thereby enhancing nuclear relaxation rates and producing contrast in T_1 or T_2-weighted MRI[9, 12-19, 25-27]. In the second strategy, proteins with large numbers of basic or acidic amino acids are used to generate contrast through chemical exchange saturation transfer (CEST) between protein-bound and aqueous protons[6, 8, 21, 22, 28]. Each of these pioneering approaches has significant limitations. Metal-based reporters can be hindered by metal ion bioavailability and toxicity[29-35], while CEST reporters tend to require high expression levels to achieve observable contrast[6,21,22]. Hence, a major need exists for new MRI reporter genes that do not require metals and can be detected at low levels of expression.

Here, we introduce an entirely new class of nonmetallic MRI reporter genes that work by modulating water diffusivity across cell membranes. Diffusion-weighted imaging (DWI) is a well-established MRI technique used in applications ranging from basic biophysical studies to the diagnosis of diseases such as stroke[36-43]. Diffusion-weighting is commonly achieved by applying a pair of pulsed magnetic field gradients, which dephase nuclear spins in proportion to how far they diffuse in the time interval between the two pulses[41,44,45]. Accordingly, water molecules that diffuse more freely have more severely dephased proton spins and appear darker in DWI (**Figure 1a**). In biological tissues, the effective diffusion coefficient of water depends on several parameters, including its local diffusivity in intracellular and extracellular compartments, the relative volume fraction occupied by cells, and the transport of water across the plasma membrane[46-50]. Noting the strong influence of the last factor[46,51,52], we hypothesized that facilitating the transmembrane diffusion of water by overexpressing water-permeable channels would result in enhanced contrast in DWI.

Toward this end, aquaporins are a highly conserved family of tetrameric integral membrane proteins that mediate the selective exchange of water molecules across the plasma membrane in a wide range of cell types[53-58]. Previously, endogenous aquaporin expression has been correlated with water diffusivity and DWI signals in several disease states. However[52,57,58], to the best of our knowledge, aquaporins have not hitherto been described as MRI reporter genes. In this work, we introduce human aquaporin 1 (AQP1) as a new

genetically encoded reporter for diffusion weighted MRI. This reporter requires no metals, is nontoxic in several cell lines and *in vivo* tumors, produces contrast orthogonal to paramagnetic and CEST reporters and is detectable when expressed at low levels and in small subsets of cells. We characterize the imaging performance and mechanisms of AQP1 through live cell experiments and Monte Carlo models, and demonstrate its utility by imaging tumor gene expression *in vivo*.

Results

Aquaporins serve as reporters for diffusion-weighted MRI

To evaluate AQP1 as a genetically encoded reporter for diffusion-weighted MRI (**Figure 1a**), we used lentiviral transfection to generate CHO, U87 glioblastoma, and Neuro 2a neuroblastoma cell lines stably overexpressing this channel, and corresponding control cells expressing the green fluorescent protein (GFP). Expression of AQP1 and GFP were driven by identical constitutive CMV promoters in U87 and Neuro 2a cells. To implement chemogenetic control of gene expression, we used a doxycycline-regulated CMV promoter in CHO cells engineered to stably express the tetracycline transactivator (rtTA) protein. Pellets of AQP1-expressing and GFP-expressing CHO, U87 glioblastoma, and Neuro2A neuroblastoma cells were then imaged using DWI. A key parameter in diffusion-weighted pulse sequences is the effective diffusion time, Δ_{eff}, corresponding to the time interval between dephasing and rephasing gradient pulses[36,37,45,46,49,59]. Long Δ_{eff} times are important for probing the effects of water exchange between intracellular and extracellular pools because longer times allow a larger proportion of cytoplasmic water molecules to interact with the cell membrane and experience the effects of restriction and exchange[36,37,48,49,59]. Correspondingly, Monte Carlo simulations of a packed cellular lattice suggested that the effects of an aquaporin-mediated increase in water diffusion would be most pronounced at Δ_{eff} > 100 ms (**Supplementary Figure 1**). We accessed these longer diffusion times using stimulated echo DWI[46,59,60]. Pellets of AQP1-expressing cells appeared much darker in diffusion-weighted images compared to GFP controls for all cell types (**Figure 1b**), corresponding to dramatic increases in their apparent diffusion coefficients (ADC, **Figure 1c**). Measured with Δ_{eff} = 398 ms, AQP1-expressing CHO, U87 and Neuro 2a cells showed 187 ± 12%, 82 ± 5% and 95 ± 3% increases in ADC, respectively, relative to GFP controls

($P < 10^{-4}$, $n \geq 4$, t-test). The relative increase in ADC was less pronounced using a shorter diffusion time (Δ_{eff} = 18 ms, **Supplementary Figure 2**), consistent with a contrast mechanism based on water exchange across the cell membrane. The larger change in ADC in CHO cells compared to Neuro2A and U87 is a likely consequence of the lower basal ADC in control CHO cells (377.57 ± 20.86 μm^2 s^{-1} at Δ_{eff} = 398 ms) compared to control Neuro2A and U87 cells (539.69 ± 11 and 479.25 ± 21.23 μm^2 s^{-1}, respectively). To establish orthogonality to

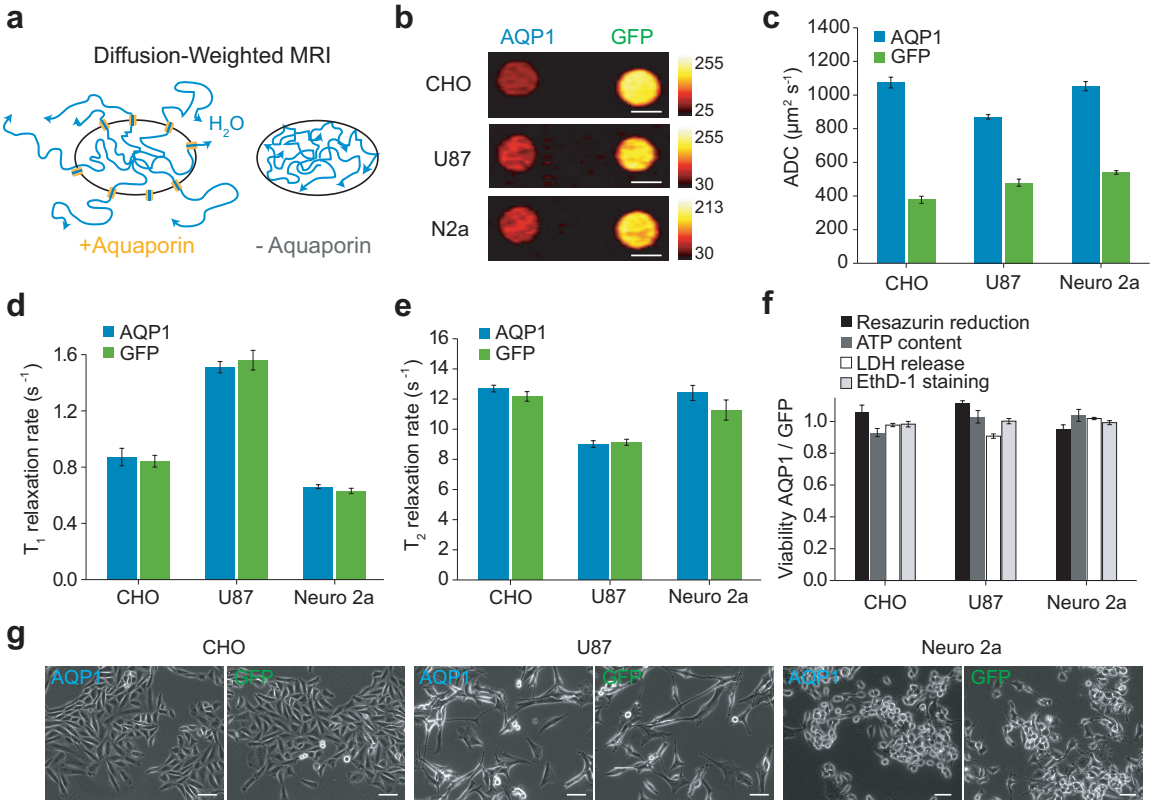

Figure 1 | AQP1 functions as a genetically encoded reporter for diffusion weighted MRI. (a) Illustration of the impact of aquaporin expression on water diffusion across the cell membrane and the resulting decrease in diffusion weighted signal intensity. **(b)** Diffusion weighted images of CHO, U87, and N2a cell pellets expressing AQP1 or GFP, acquired using a b-value of ~ 1000 s mm^{-2}. Scale bars, 3 mm. **(c)** ADC of water in CHO, U87, and N2a cells expressing AQP1 relative to GFP controls, measured at Δ_{eff} = 398 ms. Transgene expression in CHO cells was induced with 1 μg/mL doxycycline, while U87 and N2a cells express AQP1 from a constitutive promoter. n = 4 (U87, N2a), 5 (CHO) biological replicates. **(d)** Longitudinal (T_1) and **(e)** transverse (T_2) relaxation rates in cells expressing AQP1 or GFP. n = 3 (N2a, CHO) or 4 (U87) biological replicates. **(f)** Cell viability upon AQP1 or GFP expression. n = 12 (resazurin assay), 6 (ATP content), 4 (LDH release), and 3 (ethidium staining) biological replicates. Error bars ± SEM. **(g)** Phase contrast images of CHO, U87, and N2a cells expressing AQP1 or GFP.

paramagnetic reporters, we measured the T_1 and T_2 relaxation rates of cells expressing AQP1. Overexpression of this protein did not affect T_1 or T_2 relaxation (**Figure 1, d-e,** n.s. $P > 0.24$, $n = 3$, t-test), suggesting that AQP1 could be used in combination with genetically encoded T_1 or T_2 contrast agents for multiplexed imaging. Importantly, AQP1 overexpression was nontoxic in all cell lines, as determined using four different assays, including ethidium homodimer staining, measurement of cytosolic ATP content, metabolic activity, and lactate dehydrogenase release (**Figure 1f**). In addition, no changes in cell morphology were observed under phase contrast microscopy as a result of AQP1 expression (**Figure 1g**). We note that we were also able to obtain a significant increase in ADC by transfecting cells with another human aquaporin, AQP4 (**Supplementary Figure 3**). However, the percentage increase in ADC for the AQP4 expressing cells (44 ± 6% in CHO cells, $P = 6.2 \times 10^{-3}$, $n = 3$, t-test) was smaller compared to AQP1. Therefore, we focused on AQP1 for the remainder of this work.

AQP1 is a sensitive reporter gene with a large dynamic range

Next, we sought to establish the sensitivity of AQP1 to image varying degrees of gene expression. Our Monte Carlo simulations suggested that ADC values are sensitive to a broad range of cell membrane permeabilities (Supplementary **Figure 1b**), providing AQP1 with significant dynamic range. To realize this experimentally, we expressed AQP1 in a dose-

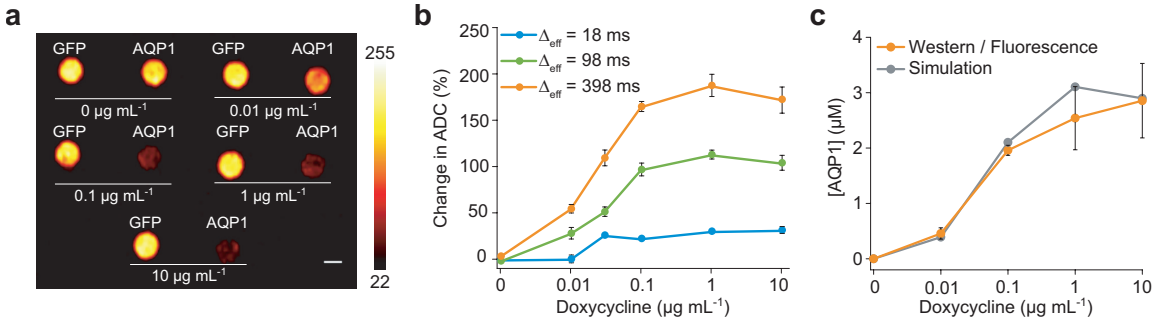

Figure 2 | AQP1 reports gene expression over a large dynamic range. (a) Diffusion weighted images (acquired at Δ_{eff} = 398 ms, b = 2089 s mm^{-2}) of CHO cells expressing AQP1 or GFP (control) and treated with varying doses of doxycycline to induce transgene expression. Scale bar indicates 3 mm. **(b)** Percent change in ADC of water in AQP1-expressing CHO cells (relative to control cells expressing GFP) as a function of doxycycline concentration, measured at different diffusion times. n = 4 biological replicates. Error bars ± SEM. **(c)** Levels of AQP1 expression on the membrane of CHO cells at different levels of doxycycline induction, estimated based on quantitative Western blotting and relative expression of a co-transcribed GFP reporter, compared to values calculated from Monte Carlo simulations based on the ADC results in (b). n ≥ 3 biological replicates. Error bars ± SEM.

dependent fashion by supplementing CHO cells with varying concentrations of doxycycline and imaged them with DWI (**Figure 2, a-b**). The corresponding levels of AQP1 expression were quantified via western blotting and measurements of IRES-linked GFP fluorescence (**Figure 2c, Supplementary Figure 4**). A significant increase in ADC was observed across all levels of induction, with differences of 54 ± 5% to 187 ± 12% ($P \leq 6.8 \times 10^{-3}$, $n \geq 3$, t-test) compared to controls at doxycycline concentrations of 0.01 to 1 μg mL^{-1}. Notably, the 54% change in contrast corresponds to an estimated AQP1 expression level of just 457 ± 102 nM, consistent with simulation predictions (**Figure 2c**). This high sensitivity and large dynamic range will facilitate the use of AQP1 as a reporter gene in a variety of biomedical applications.

AQP1 expression is observable in cells in a mixed population

The ability to specifically detect small numbers of genetically labelled cells in an otherwise unlabeled population would enable the use of genetically encoded reporters in applications such as *in vivo* tracking of cell-based therapeutics[16, 61, 62]. Having shown that AQP1 can appreciably increase water diffusion even at low levels of expression (**Figure 2**), we tested whether apparent water diffusion could be significantly increased if AQP1 expression was restricted to a small subset of cells in a mixed population. Intuitively, the relationship between the aquaporin-expressing fraction and water diffusion is expected to be nonlinear, since in small-fraction scenarios, cells expressing aquaporin would be surrounded mostly by cells without enhanced water permeability, and the impact of aquaporin expression on overall tissue diffusivity would thereby be diminished (**Figure 3a**). However, our Monte Carlo simulations predicted that AQP1-expressing fractions as small as 10% should be sufficient to measurably increase the apparent diffusivity (**Figures 3b, Supplementary Figure 1c**). To verify this experimentally, we imaged mixed populations of AQP1-expressing and GFP-expressing CHO cells in varying proportions (**Figure 3c**). Notably, this revealed significant contrast and increase in ADC in cell populations containing just 10% AQP1-expressing cells (21.44 ± 5.21% increase relative to all-GFP controls, $P = 0.03$, $n = 4$, t-test, **Figure 3d**). This data suggests that, contrary to initial intuition, diffusional reporter genes such as AQP1 are suitable for imaging gene expression in heterogeneous or infiltrating cell populations.

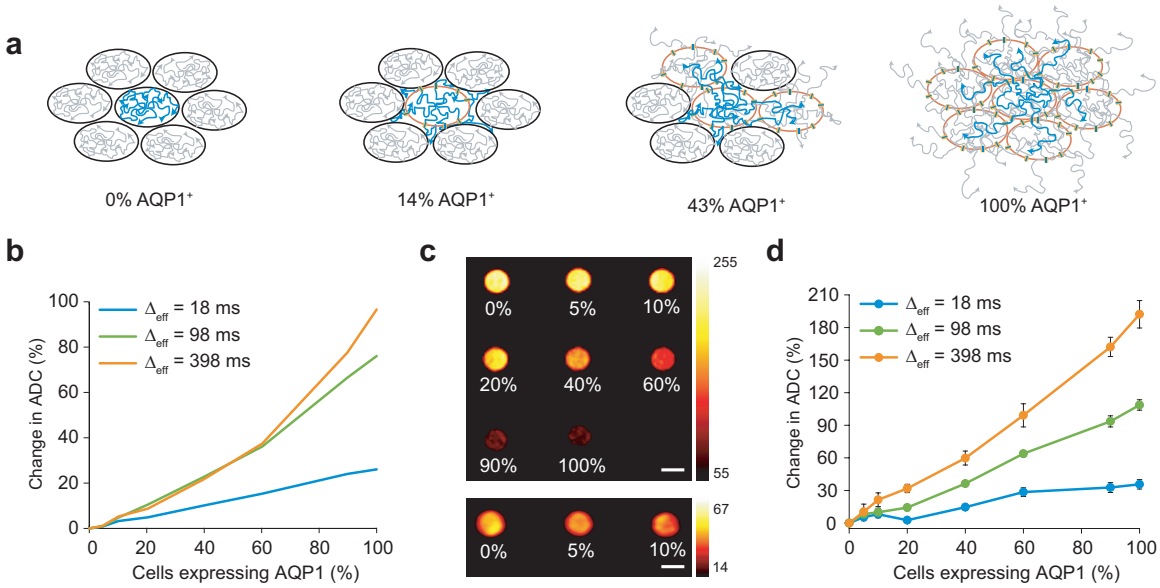

Figure 3 | AQP1 expression is observable in mixed cell populations. (a) Illustration of the effect of an increasing fraction of AQP1-labeled cells in a tissue on the overall diffusivity of water. **(b)** Monte Carlo simulation predictions of change in ADC as a function of the fraction of cells expressing AQP1 in a mixed cellular lattice. **(c)** Top: diffusion weighted MRI (acquired at Δeff = 198 ms, b = 2,334 s mm-2) of cells comprising AQP1-labeled cells mixed with GFP-labeled control cells in varying proportions. Bottom: image of mixed populations containing 0, 5, and 10% AQP1-expressing cells acquired using Δeff = 398 ms, b = 8000 s mm-2to maximize contrast for the low AQP1 fraction scenario, smoothed with a Gaussian filter (radius 1.5 pixels). Scale bars represent 3 mm. **(d)** Percent change in ADC in mixed AQP1/GFP cell pellets as a function of the fraction of AQP1-expressing cells. N = 4 biological replicates. Error bars ± SEM.

AQP1 enables gene expression imaging in tumor xenografts

To demonstrate the ability of AQP1 to report gene expression *in vivo*, we stereotaxically implanted AQP1 and GFP-transfected CHO cells in the right and left striatum of 5-7 week old immunodeficient mice. CHO cell xenografts[63,64] were used to enable doxycycline-based regulation of gene expression in the tumors. Tumors were allowed to develop for a period of 5 days, following which we induced transgene expression using intraperitoneal injections of doxycycline. Mice were imaged using diffusion weighted MRI before and 24 to 48 hours after induction, as outlined in **Figure**

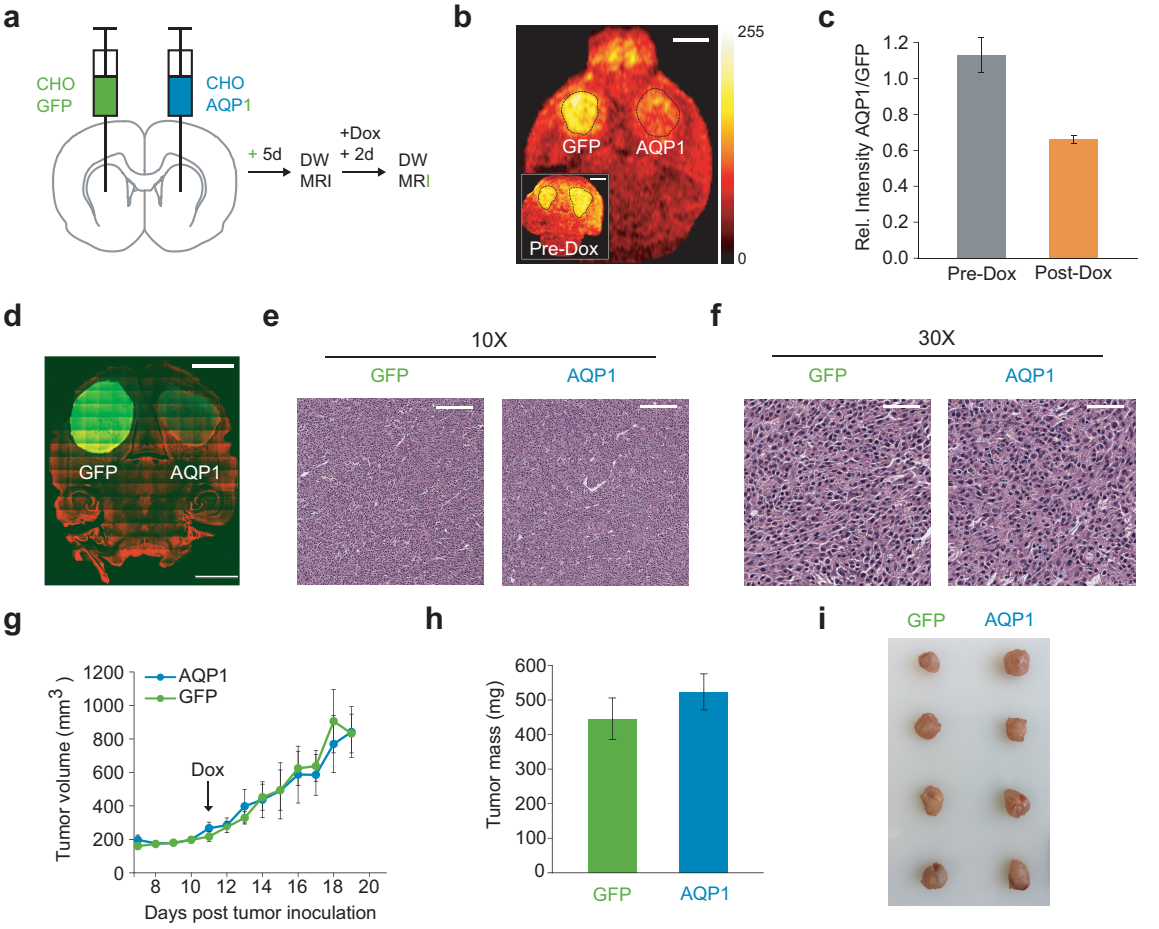

Figure 4 | AQP1 enables the imaging of gene expression in intracranial tumor xenografts. (a) Experimental approach to establishing bilateral tumors in the striatum, inducing transgene expression, and performing diffusion weighted MRI. **(b)** Representative diffusion weighted image of a horizontal brain slice with bilateral tumor xenografts, 48 hours after doxycycline injection. Inset shows a diffusion weighted image of the same mouse acquired before doxycycline injection. Images were acquired at Δ_{eff} = 98 ms and b-value = 1000 s mm^{-2}. Dashed lines indicate the tumor ROI(s). Scale bar represents 2 mm. **(c)** Average diffusion weighted image intensity of AQP1-expressing tumors relative to contralateral GFP-expressing tumors before and after doxycycline induction. n = 5 biological replicates. Error bars ± SEM. **(d)** Confocal fluorescence image of a representative 100 µm section of a mouse brain implanted with GFP and AQP1 tumors. The AQP1 tumor appears dimmer due to diminished GFP translation from the IRES sequence. Cell nuclei are counterstained using TO-PRO iodide (red). Scale bar represents 2 mm. **(e)** Low (10X) and **(f)** high (30X) magnification images of 5 µm hematoxylin-eosin stained sections of intracranial tumor xenografts expressing AQP1 and GFP. Scale bars represent 30 µm and 10 µm, respectively. **(g)** Longitudinal measurements of tumor growth in bilateral subcutaneous xenografts induced using doxycycline to express AQP1 or GFP 11 days following tumor inoculation. **(h)** Mean end-point tumor mass and **(i)** images of AQP1 and GFP expressing subcutaneous tumors harvested 9 days after doxycycline induction of gene expression. n = 4 biological replicates. Error bars ± SEM.

4a. As expected, AQP1-expressing tumors are readily distinguishable from contralateral

GFP-expressing cells in diffusion weighted images acquired after induction (**Figure 4b**), with the average diffusion weighted signal intensity in AQP1 tumors decreasing by 39.4 ± 6.5% after doxycycline injection compared to GFP controls ($P = 0.0155$, $n = 5$, pairwise t-test) (**Figure 4c, Supplementary Figure 5**). We found that a diffusion time (Δ_{eff}) of 98 ms provided the optimal balance of AQP1-dependent contrast and acquisition times for *in vivo* experiments. AQP1 and GFP expression in the bilateral tumors was confirmed by fluorescence imaging of fixed brain tissue slices (**Figure 4d**). Hematoxylin-eosin staining revealed no sign of necrosis in either the AQP1 or GFP expressing tumors, indicating that the increase in ADC in AQP1 xenografts is caused by AQP1 expression rather than necrosis or other changes in tumor morphology (**Figure 4, e-f**).

To quantitatively evaluate whether AQP1 overexpression affects tumor growth *in vivo*, we measured growth curves and terminal tumor masses in subcutaneous xenografts established using the same cell lines as the intracranial tumors and induced the same way with doxycycline. The AQP1 and GFP tumors proliferated at similar rates following doxycycline induction and reached statistically indistinguishable end-point masses (**Figure 4, g-i,** n.s. $P > 0.5$, $n = 4$, pair-wise t-test). The ability of AQP1 to produce robust induction-dependent MRI contrast in tumor xenografts without affecting tumor growth suggests that this reporter gene could be useful for longitudinal imaging of gene expression *in vivo*.

Discussion

Our results establish aquaporins, and specifically AQP1, as the first genetically encoded reporter for diffusion weighted MRI. AQP1-dependent contrast is readily observed in cell cultures, including cells known to have higher levels of endogenous aquaporins (*e.g.*, U87 glioblastoma cells[65]) as well as *in vivo* tumor xenografts, and AQP1 expression has no adverse effect on cell proliferation and viability. Aquaporins have several distinct advantages relative to existing MRI reporter genes. First, as a metal-free reporter, aquaporins are not limited by metal bioavailability and do not require the administration of metal ions or chelates. Second, AQP1-dependent contrast can be detected at reasonably low concentrations (~0.5 μM), which makes it a sensitive MRI reporter gene. Although CEST reporters operating on hyperpolarized xenon can achieve even higher molecular sensitivity[24, 66], their use requires elaborate equipment for xenon hyperpolarization and administration, and in the

case of gas vesicles, the expression of complex multi-gene clusters. Additionally, successful CEST experiments require sophisticated pulse sequences, whereas diffusion weighted imaging is implemented as a standard technique on clinical MRI scanners. Finally, as a human protein that works without sequence modifications, aquaporin can serve as a fully autologous reporter gene, overcoming concerns about potential immunogenicity faced by xenogeneic and engineered reporters.

AQP1 expression does not affect transverse and longitudinal relaxation rates in cells, which creates the possibility of multiplexed magnetic resonance imaging of gene expression by combining aquaporins with existing T_1, T_2, or CEST reporters. In addition, it is conceivable that increased water diffusion in AQP1 expressing cells could enhance the relaxivity of co-localized T_1 or T_2 agents by facilitating paramagnetic relaxation of a larger fraction of water molecules.

One potential limitation of aquaporin as a reporter gene is its negative contrast enhancement, as AQP1 expression results in image darkening in diffusion weighted MRI. Although negative contrast agents are widely established in MRI, their use warrants a certain degree of caution in light of potential confounding signal dropout from lesions, abscesses, and susceptibility artifacts. In the case of aquaporin, confounds from T_1 and T_2 relaxation can be accounted for by mapping ADC rather than acquiring single diffusion-weighted images. To distinguish aquaporin expression from tissue structures with high background diffusivity, such as fluid-filled cysts and necrotic lesions, it may be necessary to combine information from ADC measurements at several Δ_{eff} times and from T_1 and/or T_2 weighted images. Chemogenetic toggling of aquaporin expression, trafficking, or degradation could also help identify reporter gene-dependent signals. Finally, although we have demonstrated the application of AQP1 as a nontoxic MRI reporter in three different cell lines and *in vivo* tumors, the broader utility of this reporter gene in the context of different cell types and tissue architectures (*e.g.*, epithelial cells, neurons) and alternative biological applications remains to be investigated in future studies.

Given the ubiquity of DWI and stimulated echo pulse sequences, the imaging of aquaporin-based reporters can be implemented immediately by laboratories with standard MRI equipment. Beyond this, imaging performance could potentially be improved further using alternative pulse sequences specifically designed to produce contrast sensitive to

transmembrane water exchange[60], the further development of which will be stimulated by this work. In addition, we anticipate that the performance of aquaporins as MRI reporters can be further enhanced through molecular engineering of variants with improved or stimulus-gated permeability to enable functional imaging of biologically relevant markers. Overall, the high performance, biocompatibility, and engineering capacity of aquaporin reporter genes will enable this remarkably simple new approach to biomolecular MRI to impact many areas of biology and medicine.

Methods

Construction of aquaporin and GFP expressing cell lines

Human *AQP1* (NM_198098.1) and *AQP4* (NM_001650.4) cDNAs were ordered from OriGene (Rockville, MD) and subcloned into a lentiviral vector downstream of a constitutive CMV or doxycycline-regulated CMV promoter (Clontech) and an N-terminal FLAG tag. The doxycycline-regulated CMV was used specifically to place AQP1 or GFP under the control of doxycycline using a commercially available CHO cell line (Clontech) that expresses the rtTA transactivator. Enhanced GFP was fused downstream of aquaporin via an IRES sequence. Lentiviral packaging was performed in HEK 293T cells by transfecting 22 μg of packaging plasmid to expresses the capsid genes from a CMV promoter along with 22 μg of insert plasmid harboring the gene of interest (*AQP1-IRES-EGFP*, *AQP4-IRES-EGFP*, or *GFP*) flanked by LTR sequences, and 4.5 μg of VSV-G plasmid that expresses the vesicular stomatitis virus G protein to enable broad tropism of the lentiviral particles. Transfection was achieved using 25 kDa linear polyethyleneimine (Polysciences, Warrington, PA) at a concentration of 2.58 mg PEI/mg DNA. Approximately 24 hours post transfection, the culture medium was supplemented with sodium butyrate at 10 mM concentration to induce expression of the packaging genes. Virus production was allowed to proceed for 48–60 hours following which the virus-laden supernatant was collected, centrifuged at 500 x g to remove residual HEK 293T cells, mixed with 1/10th the volume of Lenti-X concentrator (Clontech, Mountain View, CA), and incubated at 4°C for at least 24 hours. Lentiviral particles were subsequently sedimented by centrifugation at 1500 x g for 45 minutes at 4°C and resuspended in 1–2 mL of Dulbecco's Modified Eagle Medium. Resuspended viral particles were immediately used to transfect CHO, CHO-TetON,

Neuro2A, or U87 cells to generate stable cell lines. For this, the cells were first grown to 70-80% confluency in 6-well plates. Spent medium was aspirated from the wells and replaced with 1 mL lentivirus suspension together with 8 μg/mL polybrene. The cells were spinfected at 2000 x g for 90 minutes at 30°C, following which the plates were returned to the 37°C incubator for 48 hours to allow gene expression. Control cell lines were generated in the same way to express enhanced GFP from a constitutive or doxycycline-regulated CMV promoter. Cell lines were obtained from American Type Cell Culture Collection (U87, N2a, HEK 293T, CHO) or from Clontech (CHO TetON) and used without further validation. Further, we note that none of the cell lines used in the paper are listed in the database of cross-contaminated cell lines maintained by the International Cell Line Authentication Committee (ICLAC) as of 10/26/2016. Some of the cell lines were periodically checked for Mycoplasma contamination using the MycoAlert detection kit from Lonza.

Determination of cell viability

Cell viability was determined using four different approaches including staining with ethidium homodimer-1 (Thermo Fisher) and measurement of resazurin reduction (CellTiter-Blue assay, Promega), ATP content (CellTiter-Glo assay, Promega), and lactate dehydrogenase release (CytoOne, Promega). For ethidium homodimer-1 staining, AQP1- and GFP-expressing cells were grown in 6-well plates for 48 hours, trypsinized, and resuspended in 100 μL PBS supplemented with ethidium homodimer-1 at 4 μM final concentration. The cell-dye mixture was allowed to incubate at 4°C for 1 hour in a rotary shaker. Subsequently, 10 μL of the cell suspension was loaded in a disposable hemocytometer (C-chip DHC S02, Incyto), and the total number of cells was estimated by imaging the hemocytometer chamber using bright field microscopy. Dead cells stained red and were estimated using fluorescence imaging with a Cy3 filter set. Viability was calculated as the fraction of cells that did not stain using ethidium homodimer-1. For the remaining cytotoxicity assays, AQP1- and GFP-expressing cells were grown in 96-well plates for 24-48 hours and treated with the assay reagents as described by the manufacturer. Fluorescence (resazurin reduction and lactate dehydrogenase release) or luminescence (ATP content assay) readouts were measured using a SpectraMax fluorescence plate reader using an excitation wavelength of 560 nm and with the emission filter set to 590 nm for fluorescence and with an open filter slot with a 1 second integration time for luminescence.

Quantification of AQP1 expression

AQP1 expression was quantified via western blotting and relative fluorescence measurements. AQP1 expression was induced in CHO cells by treating the cells with doxycycline for 48 hours. Membrane fractions were isolated using ProteoExtract native membrane protein extraction kit (EMD Millipore, Billerica, MA) or MEM-PER Plus membrane protein extraction kit (ThermoFisher) and concentrated ~30-fold using a 10 kDa centrifugal filter. Alternatively, proteins were concentrated using trichloroacetic acid precipitation (ProteoExtract protein precipitation kit). Proteins were denatured at 37°C for at least 1 hour followed by 95 °C for 5 minutes and resolved on a denaturing SDS PAGE gel, transferred to a PVDF membrane, and probed using mouse anti-FLAG primary antibodies (0.5 μg mL^{-1} final concentration) and horseradish peroxidase conjugated goat anti-mouse IgG secondary antibodies (0.4 μg mL^{-1} final concentration). Primary and secondary antibodies were purchased from Sigma (catalog number F1365) and Santa Cruz Biotech (catalog number sc-2005). Signal detection was achieved using the Clarity chemiluminescent substrate (Biorad, Hercules, CA) using an exposure time of 1–10 s. AQP1 expression was quantified from a calibration curve of known quantities (100 to 400 ng) of FLAG-tagged bacterial alkaline phosphatase (Sigma Aldrich) that was simultaneously loaded, stained, and imaged on the same blot (**Supplementary Figure 4a**). As AQP1 expression in cells induced with 0.01 μg mL^{-1} doxycycline was below the chemiluminescence detection limit of our western blot, we estimated AQP1 concentration in this case by quantifying doxycycline dependent fluorescence of IRES-linked GFP. In particular, we measured GFP fluorescence in cells induced using various concentrations of doxycycline to derive a dose-response curve for transcriptional regulation by doxycycline. Based on this, we estimated a relative response ratio of 0.18 ± 0.03 ($n = 4$) between GFP expression in low (0.01 μg mL^{-1}) and high (1 μg mL^{-1}) doxycycline conditions. As *AQP1* and *GFP* are co-transcribed into a single polycistronic construct, we expect the doxycycline dose-response curve to be conserved for the *AQP1* mRNA as well. This enabled us to extrapolate the concentration of AQP1 in the low doxycycline scenario by multiplying the measured AQP1 concentration at high doxycycline induction (2.54 ± 0.46 μM based on Western blotting, $n = 5$) by the response ratio of 0.18. For the fluorescence measurements, doxycycline treated cells were lysed using RIPA buffer and GFP fluorescence was measured in the cell lysates using a SpectraMax fluorescence plate reader with excitation wavelength set to 450 nm. Fluorescence emission

was quantified by integrating the emission spectrum between 480 and 610 nm. Prior to fluorescence measurements, lysate concentrations were adjusted to ensure equal total protein levels across samples.

Diffusion weighted MRI of cell pellets

For diffusion weighted MRI, cells were grown for 48 hours, trypsinized, resuspended in 100 µL PBS, and centrifuged at 500 x g for 5 minutes in 0.2 mL PCR tubes to produce a compact pellet. Subsequently, the tubes were loaded in wells molded in a 1% agarose phantom and imaged using a Bruker 7T horizontal bore MRI scanner equipped with a 7.2 cm diameter bore transceiver coil for RF excitation and detection. Diffusion weighted images were acquired on a 1.5 or 2 mm thick horizontal slice through the cell pellets using a stimulated echo DWI sequence with the following parameters: echo time, T_E = 24.5 ms, repetition time, T_R = 2 s, number of excitations = 1 – 3, gradient duration, δ = 7 ms, matrix size = 256 x 256, and FOV = 3.5 x 6.5 cm^2. The gradient interval (Δ) was varied from 20 to 400 ms to generate effective diffusion times ($\Delta_{eff} = \Delta - \delta/3$) of 18–398 ms in each experiment. Single axis diffusion gradients were applied, and gradient strength was varied to generate b-values in the range 0–800 s/mm^2. For each value of Δ_{eff}, ADC was calculated from the slope of the logarithmic decay in MRI signal intensity versus b-value. Images were analyzed using custom macros in ImageJ (NIH). A linear 8-bit color scale was used to facilitate the visualization of the relevant contrast in each figure. Least squares regression fitting was performed using Origin 2016 or Matlab version 9 (2016).

T_1 and T_2 weighted MRI of cell pellets

T_1 weighted images were acquired using a rapid acquisition with relaxation enhancement (RARE) sequence with the following parameters: T_E = 9.6 ms, RARE factor = 4, N_{EX} = 2, matrix size = 128 x 256, FOV = 8 x 5 cm^2, slice thickness = 1.5 mm, and receiver bandwidth = 50,505.1 Hz. Variable T_R times were used including 146.19, 321.47, 519.98, 748.83, 1018.9, 1348.72, 1771.99, 2363.81, 3355.44, and 7500 ms. T_1 values were estimated from the following equation:

$$\frac{S}{S_0} = 1 - e^{\frac{-T_R}{T_1}} \qquad (1)$$

where S_0 is the equlibrium magnetization. T_2 weighted images were acquired using a Car-Purcell-Meiboom-Gill pulse sequence with the following parameters: T_E = 11 ms, T_R = 1.5 s, number of echoes = 63, number of excitations = 4, matrix size = 256 x 256, FOV = 8 x 5 cm^2, slice thickness = 1.5 mm, and receiver bandwidth = 50,505.1 Hz. T_2 relaxation rates were estimated by fitting the first 19 echoes to the signal decay equation:

$$\frac{S}{S_0} = e^{\frac{-T_E}{T_2}} \qquad (2)$$

All images were analyzed using custom macros in ImageJ (NIH) and least squares regression fitting was performed using OriginLab. We report average T_1 and T_2 measurements for n = 4.

Mouse xenograft model

To prepare cells for intracranial tumor implantation, AQP1 and GFP expressing CHO-rtTA cells were grown for 48 hours, trypsinized, centrifuged at 500 x g for 10 minutes, and resuspended in 100 µL serum-free Dulbecco's Modified Eagle Medium. Female NOD/SCID/gamma mice between 5 and 7 weeks of age (Jackson Laboratory, Bar Harbor, ME) were anaesthetized with 2.5% isoflurane, and 10^5 AQP1 expressing CHO cells were injected stereotaxically into the right striatum. Coordinates of the injection sites with respect to bregma were: 1 mm anterior, 2 mm lateral, and 1–3 mm ventral from the surface of the calvaria. The same number of control GFP expressing CHO cells were implanted in the left striatum of the same animal.

For longitudinal measurements of tumor volume, subcutaneous xenografts were established by injecting 3 x 10^6 AQP1 and GFP CHO cells (prepared as described above and resuspended in Matrigel) into the right and left hind limbs of female NOD/SCID/gamma mice. Gene expression was induced by intraperitoneal injection of 75 µg doxycycline 11 days following tumor inoculation. Tumor size was measured daily using callipers, and tumor volume was calculated as 0.52 x (short axis)^2 x (long axis). A sample size of n = 4 biological replicates was deemed adequate for a power (expressed as 1-β) of 0.80, calculated based on the difference in AQP1 and GFP groups observed *in vitro*. Additionally, the tumor models are well established and tumor growth is stable, which obviated the need for a larger sample size. No surviving animals were excluded from the final analysis. Tumor inoculation sites were not randomized, and investigators were not blinded to the experiments. All animal

experiments were approved by the Institutional Animal Care and Use Committee of the California Institute of Technology.

Diffusion weighted MRI of brain tumor xenografts

Diffusion weighted imaging of mouse xenografts was performed using a Bruker 7T horizontal bore MRI scanner. RF excitation was delivered by a 7.2 cm diameter bore volume coil, and detection was achieved using a 3 cm diameter surface coil. Mice were anaesthetized using 1-2% isoflurane. Respiration and temperature were continuously monitored using a pressure transducer (Biopac Systems) and fiber optic rectal thermometer (Neoptix). Warm air was circulated to maintain body temperature at 30°C. Tumor formation was confirmed by acquiring diffusion weighted images 5 days following xenograft implantation, after which mice were intraperitoneally injected with 75 μg doxycycline to induce expression of AQP1 and GFP in the tumors. A second set of diffusion weighted images was acquired 24-48 hours following doxycycline injection. Preliminary diffusion weighted images to locate the tumors were first acquired on horizontal slices using a 3D echo planar imaging (EPI) stimulated echo DWI sequence with the following parameters: T_R = 2.5 or 3 s, T_E = 25.7 ms, δ= 7 ms, Δ = 100 ms, b = 1000 s/mm^2, number of excitations = 9, matrix size = 16 x 128 x 128, FOV = 1.59 x 1.29 x 0.74 cm^3. After identifying an appropriate tumor-bearing slice, 2D EPI diffusion weighted images were acquired at the slice using similar parameters but with a slice thickness of 1-2 mm, T_R = 5 s, number of excitations = 144–256.

Histological analyses of brain tissue

Mouse tumors were evaluated for gene expression and signs of necrosis via fluorescence imaging of 100 μm thick histological sections and hematoxylin-eosin staining of 5 μm thick paraffin–embedded sections. For histological analyses, mice were anaesthetized by intraperitoneal injection of ketamine (100 mg kg^{-1} of body weight) and xylazine (10 mg kg^{-1} of body weight), and transcardially perfused first with PBS containing heparin (10 units mL^{-1}, Sigma Aldrich, St. Louis, MO) and subsequently with 4% w/v paraformaldehyde (Sigma Aldrich, St. Louis, MO). Following perfusion, the brain was harvested and fixed in 4% w/v paraformaldehyde for 2 hours at room temperature and washed 3 times with PBS. Axial brain sections of 100 μm-thickness were obtained using a vibratome (Leica Biosystems, Buffalo Grove, IL). Free-floating sections were incubated for 30 minutes at room temperature with a 1 μM solution of TO-PRO-3 Iodide nuclear stain in PBS (Thermo Fisher Scientific,

Waltham, MA). Stained sections were washed three times with PBS and mounted on glass slides with ProLong Diamond Antifade Mountant (Thermo Fisher Scientific, Waltham, MA) and imaged using a confocal microscope with GFP and Cy5 specific filter sets. Hematoxylin-eosin staining was performed by the Translational Pathology Core Laboratory in the University of California, Los Angeles.

Monte Carlo simulations of water diffusion in cells

We developed a model for restricted water diffusion and exchange in cells, building on the previously described Karger and Szafer models of tissue water diffusion[48, 67, 68]. We modelled cell pellets as a face-centered cubic lattice packed with 108 spherical cells (**Supplementary Figure 1a**) with water molecules distributed randomly throughout the lattice at $t = 0$. Cell radii were sampled from a normal distribution with a mean of 6.8 μm and a standard deviation of 1.2 μm. We set the simulation time step $\tau = 50\ \mu s$ and at each time step, water molecules were propagated in a 3D random walk with step size given by $N\sqrt{\pi/2}\sqrt{2D\tau}$ in each direction. Here, N is sampled from a random normal distribution and D is the free diffusion coefficient of water at 12.9°C (the bore temperature of our MRI scanner) in the intracellular compartment (554.7 $\mu m^2\ s^{-1}$) or in the extracellular space (1664.2 $\mu m^2\ s^{-1}$)[69]. If a water molecule encounters a membrane, the propagation step is recalculated and the molecule either transmitted or reflected off the membrane with a probability given by

$$\text{probability} = 1 - 4P\sqrt{\frac{\tau}{6D}} \qquad (3)$$

wherein P is the membrane permeability and D is the free diffusion coefficient of water in the intracellular compartment. Diffusion paths were simulated in Python, and the apparent diffusion coefficient (ADC) was calculated using Matlab as described in the Szafer model[48]:

$$ADC(\Delta) = -\lim_{q\to 0^+}\frac{ln<e^{-q\frac{\sum x^2}{2}}>}{q\Delta} \qquad (4)$$

where $\sum x^2$ represents the sum square displacement of a water molecule from its starting position, and q is given by $(\gamma\delta g)^2$ where γ is the gyromagnetic ratio, g is the gradient strength, and δ is the duration of the pulsed diffusion gradient. We note that b-value is calculated as:

$$b = q.(\Delta - \delta/3) \qquad (5)$$

In the first set of simulations (ADC *vs.* permeability), we varied the cell permeability from .034 to 0.39 μm/ms and calculated ADC(Δ) for each value of cell permeability. In the second set of simulations (ADC *vs.* fraction of AQP1-expressing cells) the permeability of AQP1-expressing cells and control cells were fixed at 0.14 μm ms^{-1} and 0.039 μm ms^{-1} respectively, in accordance with previously published values[55]. We incrementally varied the fraction of cells expressing AQP1, and for each composition, simulated 3 x 10^4 (nonunique) random arrangements of AQP1 expressing and control cells to exclude geometry or arrangement dependent bias in the results. ADC(Δ) was estimated corresponding to varying fractions of AQP1 expressing cells in the population.

Estimation of AQP1 expression from Monte Carlo simulations

Based on the simulated trend of ADC as a function of cell permeability, we calculated permeability values of CHO cells induced with various concentrations of doxycycline and for which ADC values had been experimentally measured. Permeability values calculated in this fashion ranged from 0.074 μm ms^{-1} to 0.55 μm ms^{-1} corresponding to 0.01 μg mL^{-1} and 1 μg mL^{-1} doxycycline concentrations. Next, permeability values were converted to volumetric flow rates by taking their product with the average surface area of a CHO cell (380 μm^2). AQP1 concentration was estimated based on the previously reported unit channel conductance of 6 x 10^{-5} $\mu m^3 ms^{-1}$ [53, 55].

Statistical analysis

For statistical significance testing, we used two-sided homoscedastic t-tests with a significance level of type I error set at 0.05 for rejecting the null hypothesis. Paired-sample t-tests were used where indicated. Homogeneity of variances between data sets was verified using Bartlett's test or F-test, though we note that the statistical significance of our results remains conserved upon using the Welch's t-test for heteroscedastic distributions. Normal distribution of data sets was verified using the Kolmogorov-Smirnov test with a significance level of 0.01.

References

1. Rao, J., Dragulescu-Andrasi, A. & Yao, H. Fluorescence imaging in vivo: recent advances. *Current opinion in biotechnology* **18**, 17-25 (2007).
2. Contag, C.H. & Bachmann, M.H. Advances in in vivo bioluminescence imaging of gene expression. *Annual review of biomedical engineering* **4**, 235-260 (2002).
3. Chudakov, D.M., Matz, M.V., Lukyanov, S. & Lukyanov, K.A. Fluorescent proteins and their applications in imaging living cells and tissues. *Physiological reviews* **90**, 1103-1163 (2010).
4. Ntziachristos, V., Ripoll, J., Wang, L.V. & Weissleder, R. Looking and listening to light: the evolution of whole-body photonic imaging. *Nature biotechnology* **23**, 313-320 (2005).
5. Naumova, A.V., Modo, M., Moore, A., Murry, C.E. & Frank, J.A. Clinical imaging in regenerative medicine. *Nature biotechnology* **32**, 804-818 (2014).
6. Bar-Shir, A. et al. Human protamine-1 as an MRI reporter gene based on chemical exchange. *ACS chemical biology* **9**, 134-138 (2013).
7. Louie, A.Y. et al. In vivo visualization of gene expression using magnetic resonance imaging. *Nature biotechnology* **18**, 321-325 (2000).
8. Bar-Shir, A. et al. Transforming thymidine into a magnetic resonance imaging probe for monitoring gene expression. *Journal of the American Chemical Society* **135**, 1617-1624 (2013).
9. Zurkiya, O., Chan, A.W. & Hu, X. MagA is sufficient for producing magnetic nanoparticles in mammalian cells, making it an MRI reporter. *Magnetic resonance in medicine* **59**, 1225-1231 (2008).
10. Cohen, B., Dafni, H., Meir, G., Harmelin, A. & Neeman, M. Ferritin as an endogenous MRI reporter for noninvasive imaging of gene expression in C6 glioma tumors. *Neoplasia* **7**, 109-117 (2005).
11. Cohen, B. et al. MRI detection of transcriptional regulation of gene expression in transgenic mice. *Nature medicine* **13**, 498-503 (2007).
12. Patrick, P.S. et al. Dual-modality gene reporter for in vivo imaging. *Proceedings of the National Academy of Sciences* **111**, 415-420 (2014).
13. Patrick, P.S. et al. Development of Timd2 as a reporter gene for MRI. *Magnetic resonance in medicine* **75**, 1697-1707 (2016).
14. Matsumoto, Y., Chen, R., Anikeeva, P. & Jasanoff, A. Engineering intracellular biomineralization and biosensing by a magnetic protein. *Nature communications* **6** (2015).
15. Genove, G., DeMarco, U., Xu, H., Goins, W.F. & Ahrens, E.T. A new transgene reporter for in vivo magnetic resonance imaging. *Nature medicine* **11**, 450-454 (2005).
16. Iordanova, B. & Ahrens, E.T. In vivo magnetic resonance imaging of ferritin-based reporter visualizes native neuroblast migration. *Neuroimage* **59**, 1004-1012 (2012).

17. Deans, A.E. et al. Cellular MRI contrast via coexpression of transferrin receptor and ferritin. *Magnetic resonance in medicine* **56**, 51-59 (2006).

18. Bartelle, B.B., Mana, M.D., Suero-Abreu, G.A., Rodriguez, J.J. & Turnbull, D.H. Engineering an effective Mn-binding MRI reporter protein by subcellular targeting. *Magnetic resonance in medicine* **74**, 1750-1757 (2015).

19. Bartelle, B.B., Szulc, K.U., Suero-Abreu, G.A., Rodriguez, J.J. & Turnbull, D.H. Divalent metal transporter, DMT1: A novel MRI reporter protein. *Magnetic resonance in medicine* **70**, 842-850 (2013).

20. Westmeyer, G.G. & Jasanoff, A. Genetically controlled MRI contrast mechanisms and their prospects in systems neuroscience research. *Magnetic resonance imaging* **25**, 1004-1010 (2007).

21. Airan, R.D. et al. MRI biosensor for protein kinase A encoded by a single synthetic gene. *Magnetic resonance in medicine* **68**, 1919-1923 (2012).

22. Gilad, A.A. et al. Artificial reporter gene providing MRI contrast based on proton exchange. *Nature biotechnology* **25**, 217-219 (2007).

23. Gilad, A.A., Winnard, P.T., van Zijl, P. & Bulte, J.W. Developing MR reporter genes: promises and pitfalls. *NMR in biomedicine* **20**, 275-290 (2007).

24. Shapiro, M.G. et al. Genetically encoded reporters for hyperpolarized xenon magnetic resonance imaging. *Nature chemistry* **6**, 629-634 (2014).

25. Shapiro, M.G., Szablowski, J.O., Langer, R. & Jasanoff, A. Protein nanoparticles engineered to sense kinase activity in MRI. *Journal of the American Chemical Society* **131**, 2484-2486 (2009).

26. Shapiro, M.G. et al. Directed evolution of a magnetic resonance imaging contrast agent for noninvasive imaging of dopamine. *Nature biotechnology* **28**, 264-270 (2010).

27. Matsumoto, Y. & Jasanoff, A. Metalloprotein-based MRI probes. *FEBS letters* **587**, 1021-1029 (2013).

28. Sherry, A.D. & Woods, M. Chemical exchange saturation transfer contrast agents for magnetic resonance imaging. *Annual review of biomedical engineering* **10**, 391 (2008).

29. Olanow, C.W. Manganese-induced parkinsonism and Parkinson's disease. *Annals of the New York Academy of Sciences* **1012**, 209-223 (2004).

30. Caravan, P., Ellison, J.J., McMurry, T.J. & Lauffer, R.B. Gadolinium (III) chelates as MRI contrast agents: structure, dynamics, and applications. *Chemical reviews* **99**, 2293-2352 (1999).

31. Silva, A.C., Lee, J.H., Aoki, I. & Koretsky, A.P. Manganese-enhanced magnetic resonance imaging (MEMRI): methodological and practical considerations. *NMR in Biomedicine* **17**, 532-543 (2004).

32. Cacheris, W.P., Quay, S.C. & Rocklage, S.M. The relationship between thermodynamics and the toxicity of gadolinium complexes. *Magnetic resonance imaging* **8**, 467-481 (1990).

33. Wolf, G. & Baum, L. Cardiovascular toxicity and tissue proton T1 response to manganese injection in the dog and rabbit. *American journal of roentgenology* **141**, 193-197 (1983).

34. Brücher, E., Tircsó, G., Baranyai, Z., Kovács, Z. & Sherry, A.D. Stability and toxicity of contrast agents. *The Chemistry of Contrast Agents in Medical Magnetic Resonance Imaging, Second Edition*, 157-208 (2013).

35. Pereira, S.M., Moss, D., Williams, S.R., Murray, P. & Taylor, A. Overexpression of the MRI reporter genes ferritin and transferrin receptor affect iron homeostasis and produce limited contrast in mesenchymal stem cells. *International journal of molecular sciences* **16**, 15481-15496 (2015).

36. Pfeuffer, J., Flögel, U., Dreher, W. & Leibfritz, D. Restricted diffusion and exchange of intracellular water: theoretical modelling and diffusion time dependence of 1H NMR measurements on perfused glial cells. *NMR in Biomedicine* **11**, 19-31 (1998).

37. Pfeuffer, J., Flögel, U. & Leibfritz, D. Monitoring of cell volume and water exchange time in perfused cells by diffusion-weighted 1H NMR spectroscopy. *NMR in Biomedicine* **11**, 11-18 (1998).

38. Thelwall, P.E., Grant, S.C., Stanisz, G.J. & Blackband, S.J. Human erythrocyte ghosts: exploring the origins of multiexponential water diffusion in a model biological tissue with magnetic resonance. *Magnetic resonance in medicine* **48**, 649-657 (2002).

39. Winston, G.P. The physical and biological basis of quantitative parameters derived from diffusion MRI. *Quantitative imaging in medicine and surgery* **2**, 254-265 (2012).

40. Padhani, A.R. et al. Diffusion-weighted magnetic resonance imaging as a cancer biomarker: consensus and recommendations. *Neoplasia* **11**, 102-125 (2009).

41. Le Bihan, D. Diffusion MRI: what water tells us about the brain. *EMBO molecular medicine* **6**, 569-573 (2014).

42. Le Bihan, D. Looking into the functional architecture of the brain with diffusion MRI. *Nature Reviews Neuroscience* **4**, 469-480 (2003).

43. Schaefer, P.W., Grant, P.E. & Gonzalez, R.G. Diffusion-weighted MR imaging of the brain 1. *Radiology* **217**, 331-345 (2000).

44. Neil, J.J. Diffusion imaging concepts for clinicians. *Journal of Magnetic Resonance Imaging* **27**, 1-7 (2008).

45. Norris, D.G. The effects of microscopic tissue parameters on the diffusion weighted magnetic resonance imaging experiment. *NMR in Biomedicine* **14**, 77-93 (2001).

46. Li, H. et al. Time-dependent influence of cell membrane permeability on MR diffusion measurements. *Magnetic resonance in medicine* **75**, 1927-1934 (2016).

47. van der Weerd, L., Melnikov, S.M., Vergeldt, F.J., Novikov, E.G. & Van As, H. Modelling of self-diffusion and relaxation time NMR in multicompartment systems with cylindrical geometry. *Journal of Magnetic Resonance* **156**, 213-221 (2002).

48. Szafer, A., Zhong, J. & Gore, J.C. Theoretical model for water diffusion in tissues. *Magnetic resonance in medicine* **33**, 697-712 (1995).

49. Sen, P.N. Time-dependent diffusion coefficient as a probe of geometry. *Concepts in Magnetic Resonance Part A* **23**, 1-21 (2004).

50. Fieremans, E. et al. In vivo observation and biophysical interpretation of time-dependent diffusion in human white matter. *NeuroImage* **129**, 414-427 (2016).

51. Sehy, J.V., Banks, A.A., Ackerman, J.J. & Neil, J.J. Importance of intracellular water apparent diffusion to the measurement of membrane permeability. *Biophysical journal* **83**, 2856-2863 (2002).

52. Badaut, J., Fukuda, A.M., Jullienne, A. & Petry, K.G. Aquaporin and brain diseases. *Biochimica et Biophysica Acta (BBA)-General Subjects* **1840**, 1554-1565 (2014).

53. Yang, B. & Verkman, A. Water and glycerol permeabilities of aquaporins 1–5 and MIP determined quantitatively by expression of epitope-tagged constructs inXenopus oocytes. *Journal of Biological Chemistry* **272**, 16140-16146 (1997).

54. Sukstanskii, A., Yablonskiy, D. & Ackerman, J. Effects of permeable boundaries on the diffusion-attenuated MR signal: insights from a one-dimensional model. *Journal of Magnetic Resonance* **170**, 56-66 (2004).

55. Ma, T., Frigeri, A., Tsai, S.-T., Verbavatz, J. & Verkman, A. Localization and functional analysis of CHIP28k water channels in stably transfected Chinese hamster ovary cells. *Journal of Biological Chemistry* **268**, 22756-22764 (1993).

56. Agre, P., Bonhivers, M. & Borgnia, M.J. The aquaporins, blueprints for cellular plumbing systems. *Journal of Biological Chemistry* **273**, 14659-14662 (1998).

57. Badaut, J. et al. Brain water mobility decreases after astrocytic aquaporin-4 inhibition using RNA interference. *Journal of Cerebral Blood Flow & Metabolism* **31**, 819-831 (2011).

58. Fukuda, A.M. et al. Posttraumatic reduction of edema with aquaporin-4 RNA interference improves acute and chronic functional recovery. *Journal of Cerebral Blood Flow & Metabolism* **33**, 1621-1632 (2013).

59. Van Zijl, P. et al. Complete separation of intracellular and extracellular information in NMR spectra of perfused cells by diffusion-weighted spectroscopy. *Proceedings of the National Academy of Sciences* **88**, 3228-3232 (1991).

60. Nilsson, M. et al. Noninvasive mapping of water diffusional exchange in the human brain using filter-exchange imaging. *Magnetic resonance in medicine* **69**, 1572-1580 (2013).

61. Ahrens, E.T. & Bulte, J.W. Tracking immune cells in vivo using magnetic resonance imaging. *Nature Reviews Immunology* **13**, 755-763 (2013).

62. Srivastava, A.K. et al. Advances in using MRI probes and sensors for in vivo cell tracking as applied to regenerative medicine. *Disease Models and Mechanisms* **8**, 323-336 (2015).

63. Yang, M. et al. Multi-organ metastatic capability of Chinese hamster ovary cells revealed by green fluorescent protein (GFP) expression. *Clinical & experimental metastasis* **17**, 417-422 (1999).

64. Richter, G. et al. Interleukin 10 transfected into Chinese hamster ovary cells prevents tumor growth and macrophage infiltration. *Cancer research* **53**, 4134-4137 (1993).

65. Endo, M., Jain, R.K., Witwer, B. & Brown, D. Water channel (aquaporin 1) expression and distribution in mammary carcinomas and glioblastomas. *Microvascular research* **58**, 89-98 (1999).

66. Wang, Y., Roose, B.W., Palovcak, E.J., Carnevale, V. & Dmochowski, I.J. A Genetically Encoded β-Lactamase Reporter for Ultrasensitive 129Xe NMR in Mammalian Cells. *Angewandte Chemie International Edition* **55**, 8984-8987 (2016).

67. Kärger, J. Principles and applications of self-diffusion measurements by nuclear magnetic resonance. *Adv Magn Reson* **12**, 1-89 (1988).

68. Stanisz, G.J., Li, J.G., Wright, G.A. & Henkelman, R.M. Water dynamics in human blood via combined measurements of T2 relaxation and diffusion in the presence of gadolinium. *Magnetic resonance in medicine* **39**, 223-233 (1998).

69. Holz, M., Heil, S.R. & Sacco, A. Temperature-dependent self-diffusion coefficients of water and six selected molecular liquids for calibration in accurate 1H NMR PFG measurements. *Physical Chemistry Chemical Physics* **2**, 4740-4742 (2000).

70. Mukherjee, A., Wu, D., Davis, H. C. & Shapiro, M. G. Non-invasive imaging using reporter genes altering cellular water permeability. *Nature Communications* **7**, 13891 (2016).

Supplementary Information

Methods

Lentiviral packaging and transfection

Lentiviral packaging was performed in HEK 293T cells by transfecting 22 μg of packaging plasmid to express the capsid genes from a CMV promoter along with 22 μg of insert plasmid harboring the gene of interest (AQP1-IRES-EGFP, AQP4-IRES-EGFP, or GFP) flanked by LTR sequences, and 4.5 μg of VSV-G plasmid that expresses the vesicular stomatitis virus G protein to enable broad tropism of the lentiviral particles. Transfection was achieved using 25 kDa linear polyethyleneimine (Polysciences, Warrington, PA) at a concentration of 2.58 mg PEI/mg DNA. Approximately 24 hours post transfection, the culture medium was supplemented with sodium butyrate at 10 mM concentration to induce expression of the packaging genes. Virus production was allowed to proceed for 48–60 hours following which the virus-laden supernatant was collected, centrifuged at 500 x g to remove residual HEK 293T cells, mixed with $1/10^{th}$ the volume of Lenti-X concentrator (Clontech, Mountain View, CA), and incubated at 4°C for at least 24 hours. Lentiviral particles were subsequently sedimented by centrifugation at 1500 x g for 45 minutes at 4°C and resuspended in 1–2 mL of Dulbecco's Modified Eagle Medium. Resuspended viral particles were immediately used to transfect CHO, CHO-TetON, Neuro2A, or U87 cells to generate stable cell lines. For this, the cells were first grown to 70-80% confluency in 6-well plates. Spent medium was aspirated from the wells and replaced with 1 mL lentivirus suspension together with 8 μg/mL polybrene. The cells were spinfected at 2000 x g for 90 minutes at 30°C, following which the plates were returned to the 37°C incubator for 48 hours to allow gene expression.

Determination of cell viability

Cell viability was determined by staining with ethidium homodimer-1 (Thermo Fisher), which stains nucleic acids in cells with compromised membrane integrity. AQP1 and GFP expressing cells were grown in 6-well plates for 48 hours, trypsinized, and resuspended in 100 μL PBS supplemented with ethidium homodimer-1 at a final concentration of 4 μM. The cell-dye mixture was allowed to incubate at 4°C for 1 hour in a rotary shaker. Subsequently, 10 μL of the cell suspension was loaded in a disposable hemocytometer (C-chip DHC S02,

Incyto) and total number of cells was estimated by imaging the hemocytometer chamber using bright field microscopy. Dead cells stained red and were estimated using fluorescence imaging with a Cy3 filter set. Viability was calculated as the fraction of cells that did not stain using ethidium homodimer-1.

Quantification of AQP1 expression

AQP1 expression was quantified via western blotting and relative fluorescence measurements. AQP1 expression was induced in CHO cells by treating the cells with doxycycline for 48 hours. Membrane fractions were isolated using ProteoExtract native membrane protein extraction kit (EMD Millipore, Billerica, MA) or MEM-PER Plus membrane protein extraction kit (ThermoFisher) and concentrated ~30-fold using a 10 kDa centrifugal filter. Alternatively, proteins were concentrated using trichloroacetic acid precipitation (ProteoExtract protein precipitation kit). Proteins were denatured at 37°C for at least 1 hour followed by 95 °C for 5 minutes and resolved on a denaturing SDS PAGE gel, transferred to a PVDF membrane, and probed using mouse anti-FLAG primary antibodies and horseradish peroxidase conjugated goat anti-mouse secondary antibodies. Signal detection was achieved using the Clarity chemiluminescent substrate (Biorad, Hercules, CA) using an exposure time of 1–10 s. AQP1 expression was quantified from a calibration curve of known quantities (100-400 ng) of FLAG-tagged bacterial alkaline phosphatase (Sigma Aldrich) that was simultaneously loaded, stained, and imaged on the same blot (**Figure S4a**). As AQP1 expression in cells induced with 0.01 μg/mL doxycycline was below the chemiluminescence detection limit of our western blot, we estimated AQP1 concentration in this case by quantifying doxycycline dependent fluorescence of IRES-linked GFP. In particular, we measured GFP fluorescence in cells induced using various concentrations of doxycycline to derive a dose-response curve for transcriptional regulation by doxycycline. Based on this, we estimated a relative response ratio of 0.18 ± 0.03 ($n = 4$) between GFP expression in low (0.01 μg/mL) and high (1 μg/mL) doxycycline conditions. As AQP1 and GFP are co-transcribed into a single polycistronic construct, we expect the doxycycline dose-response curve to be conserved for the AQP1 mRNA as well. This enabled us to extrapolate the concentration of AQP1 in the low doxycycline scenario by multiplying the measured AQP1 concentration (2.54 ± 0.46 μM based on Western blotting, $n = 5$) in cells induced using 1 μg/mL doxycycline by the response ratio of 0.18. For the fluorescence measurements, doxycycline-treated cells were lysed using RIPA buffer and GFP

fluorescence was measured in the cell lysates using a SpectraMax fluorescence plate reader with the excitation wavelength set to 450 nm. Fluorescence emission was quantified by integrating the emission spectrum between 480 and 610 nm. Prior to fluorescence measurements, lysate concentrations were adjusted to ensure equal total protein levels across samples.

T_1 and T_2 weighted MRI

T_1 weighted images were acquired using a rapid acquisition with relaxation enhancement (RARE) sequence with the following parameters: T_E = 9.6 ms, RARE factor = 4, N_{EX} = 2, matrix size = 128 x 256, FOV = 8 x 5 cm^2, slice thickness = 1.5 mm, and receiver bandwidth = 50,505.1 Hz. Variable T_R times were used including 146.19, 321.47, 519.98, 748.83, 1018.9, 1348.72, 1771.99, 2363.81, 3355.44, and 7500 ms. T_1 values were estimated from $S/S_0 = 1 - e^{\frac{-T_R}{T_1}}$, where S_0 is the equlibrium magnetization. T_2 weighted images were acquired using a Car-Purcell-Meiboom-Gill pulse sequence with the following parameters: T_E = 11 ms, T_R = 1.5 s, number of echoes = 63, number of excitations = 4, matrix size = 256 x 256, FOV = 8 x 5 cm^2, slice thickness = 1.5 mm, and receiver bandwidth = 50,505.1 Hz. T_2 relaxation rates were estimated by fitting the first 19 echoes to $S/S_0 = e^{\frac{-T_E}{T_2}}$. All images were analyzed using custom macros in ImageJ (NIH) and least squares regression fitting was performed using OriginLab.

Histological analyses of brain tissue

For histological analyses of brain tissue, mice were anaesthetized by intraperitoneal injection of ketamine (100 mg/kg of body weight) and xylazine (10 mg/kg of body weight), and transcardially perfused first with PBS containing heparin (10 units/mL, Sigma Aldrich, St. Louis, MO) and subsequently with 4% w/v paraformaldehyde (Sigma Aldrich, St. Louis, MO). Following perfusion, the brain was harvested and fixed in 4% w/v paraformaldehyde for 2 hours at room temperature and washed 3 times with PBS. Axial brain sections of 100 µm-thickness were obtained using a vibratome (Leica Biosystems, Buffalo Grove, IL). Free-floating sections were incubated for 30 minutes at room temperature with a 1 µM solution of TO-PRO-3 Iodide nuclear stain in PBS (Thermo Fisher Scientific, Waltham, MA). Stained sections were washed three times with PBS and mounted on glass slides with ProLong

Diamond Antifade Mountant (Thermo Fisher Scientific, Waltham, MA) and imaged using a confocal microscope with GFP and Cy5 specific filter sets.

Monte Carlo simulations of water diffusion in cells

We developed a model for restricted water diffusion and exchange in cells, building on the previously described Karger and Szafer[1-3] models of tissue water diffusion. We modelled cell pellets as a face-centered cubic lattice packed with 108 spherical cells (**Figure S1a**) with water molecules distributed randomly throughout the lattice at $t = 0$. Cell radii were sampled from a normal distribution with a mean of 6.8 μm and a standard deviation of 1.2 μm. We set the simulation time step $\tau = 50\,\mu s$ and at each time step, water molecules were propagated in a 3D random walk with step size given by $N\sqrt{\pi/2}\,\sqrt{2D\tau}$ in each direction. Here, N is sampled from a random normal distribution and D is the free diffusion coefficient of water at 12.9°C (the bore temperature of our MRI scanner) in the intracellular compartment (554.7 $\mu m^2/s$) or in the extracellular space (1664.2 $\mu m^2/s$)[4]. If a water molecule encounters a membrane, the propagation step is recalculated and the molecule either transmitted or reflected off the membrane with a probability given by $1 - 4P\sqrt{\tau/6D}$, wherein P is the membrane permeability and D is the free diffusion coefficient of water in the intracellular compartment. Diffusion paths were simulated in Python and the apparent diffusion coefficient (ADC) was calculated using Matlab as described in the Szafer model[1]: $ADC(\Delta) = -\lim_{q\to 0^+} \frac{ln<e^{-q\frac{\sum x^2}{2}}>}{q\Delta}$ where $\sum x^2$ represents the sum square displacement of a water molecule from its starting position, and q is given by $(\gamma\delta g)^2$ where γ is the gyromagnetic ratio, g is the gradient strength and δ is the duration of the pulsed diffusion gradient. We note that b-value is calculated as: $b = q.(\Delta - \delta/3)$. In the first set of simulations (ADC *vs.* permeability), we varied the cell permeability from .034 to 0.39 μm/ms and calculated ADC(Δ) for each value of cell permeability. In the second set of simulations (ADC *vs.* fraction of AQP1-expressing cells), the permeability of AQP1-expressing cells and control cells were fixed at 0.14 μm/s and 0.039 μm/ms respectively, in accordance with previously published values[5]. We incrementally varied the fraction of cells expressing AQP1 and for each composition, simulated 3 x 10^4 (nonunique) random arrangements of AQP1 expressing and control cells to exclude geometry or arrangement dependent bias in the results. ADC(Δ)

was estimated corresponding to varying fractions of AQP1 expressing cells in the population.

Estimation of AQP1 expression from Monte Carlo simulations

Based on the simulated trend of ADC as a function of cell permeability, we calculated permeability values of CHO cells induced with various concentrations of doxycycline and for which ADC values had been experimentally measured. Permeability values calculated in this fashion ranged from 0.074 μm/ms to 0.55 μm/ms corresponding to 0.01 μg/mL and 1 μg/mL doxycycline concentrations. Next, permeability values were converted to volumetric flow rates by taking their product with the average surface area of a CHO cell (380 μm^2). AQP1 concentration was estimated based on the previously reported unit channel conductance of 6 x 10^{-5} $\mu m^3/ms$[5,6].

References

1 Szafer, A., Zhong, J. & Gore, J. C. Theoretical model for water diffusion in tissues. *Magnetic resonance in medicine* **33**, 697-712 (1995).

2 Stanisz, G. J., Li, J. G., Wright, G. A. & Henkelman, R. M. Water dynamics in human blood via combined measurements of T2 relaxation and diffusion in the presence of gadolinium. *Magnetic resonance in medicine* **39**, 223-233 (1998).

3 Kärger, J. Principles and applications of self-diffusion measurements by nuclear magnetic resonance. *Adv Magn Reson* **12**, 1-89 (1988).

4 Holz, M., Heil, S. R. & Sacco, A. Temperature-dependent self-diffusion coefficients of water and six selected molecular liquids for calibration in accurate 1H NMR PFG measurements. *Physical Chemistry Chemical Physics* **2**, 4740-4742 (2000).

5 Ma, T., Frigeri, A., Tsai, S.-T., Verbavatz, J. & Verkman, A. Localization and functional analysis of CHIP28k water channels in stably transfected Chinese hamster ovary cells. *Journal of Biological Chemistry* **268**, 22756-22764 (1993).

6 Yang, B. & Verkman, A. Water and glycerol permeabilities of aquaporins 1–5 and MIP determined quantitatively by expression of epitope-tagged constructs inXenopus oocytes. *Journal of Biological Chemistry* **272**, 16140-16146 (1997).

Supplementary Figures

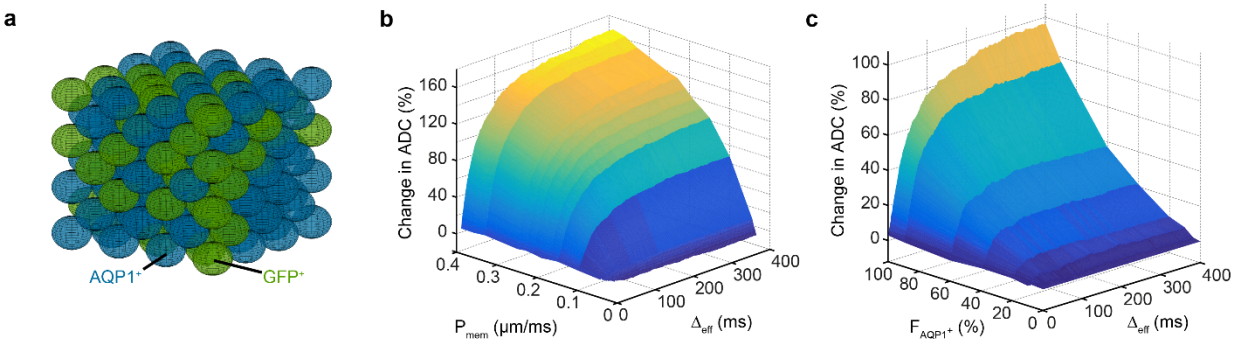

Figure S1. Monte Carlo simulations of water diffusion in $AQP1^+$ and GFP^+ (control) cells as a function of cell membrane permeability (P_{mem}), effective diffusion time (Δ_{eff}), and percentage of AQP1-labeled cells (F_{AQP1+}). **(a)** Mixed populations of $AQP1^+$ and GFP^+ cells were modeled by randomly distributing $AQP1^+$ and GFP^+ cells in the lattice to simulate 3 x 10^4 (nonunique) random arrangements of heterogeneous cell populations corresponding to varying fractions of $AQP1^+$ cells. **(b)** ADC increases with increasing cell permeability in a homogeneous cell population, with the percent change in the ADC (measured relative to control cells with a basal permeability of 0.035 μm/ms[5]) being most pronounced at longer diffusion times. **(c)** ADC increases in a nonlinear fashion with increasing fractions of AQP1-labeled cells in a mixed population comprising $AQP1^+$ and GFP^+ cells.

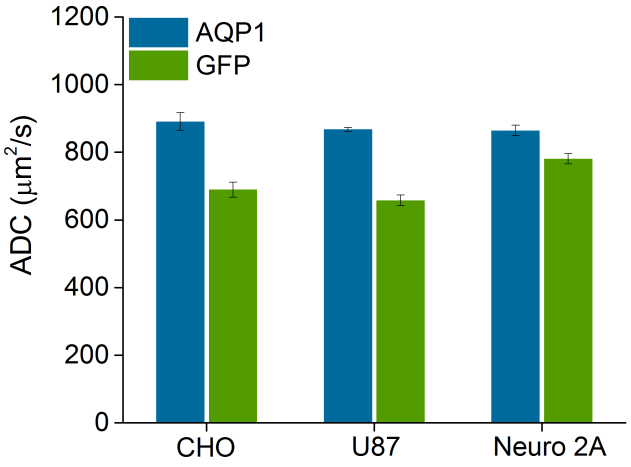

Figure S2. Apparent diffusion coefficient of water in AQP1 and GFP-expressing CHO cells measured at short diffusion times (Δ_{eff} = 18 ms). Percent change in ADC on account of AQP1 expression is smaller at short diffusion times. Error bars represent standard error of mean (SEM) for 4 biological replicates.

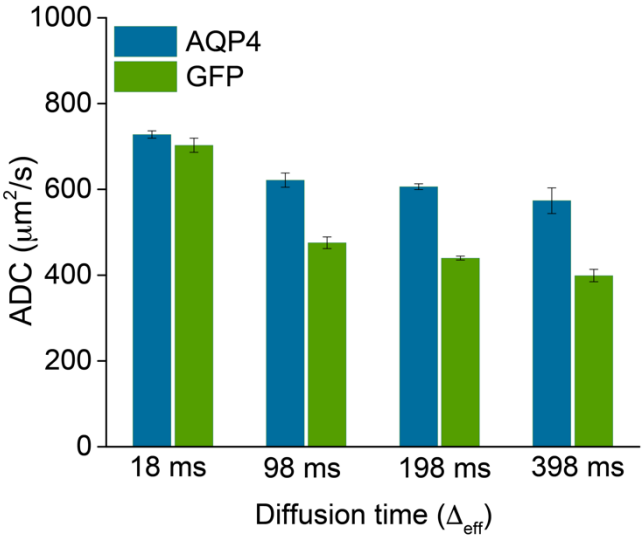

Figure S3. AQP4 is a genetically encoded reporter for diffusion weighted MRI. AQP4 expression enhances water diffusion in CHO cells relative to GFP controls, albeit not to the same extent as AQP1. Error bars represent standard error of mean (SEM) for 4 biological replicates.

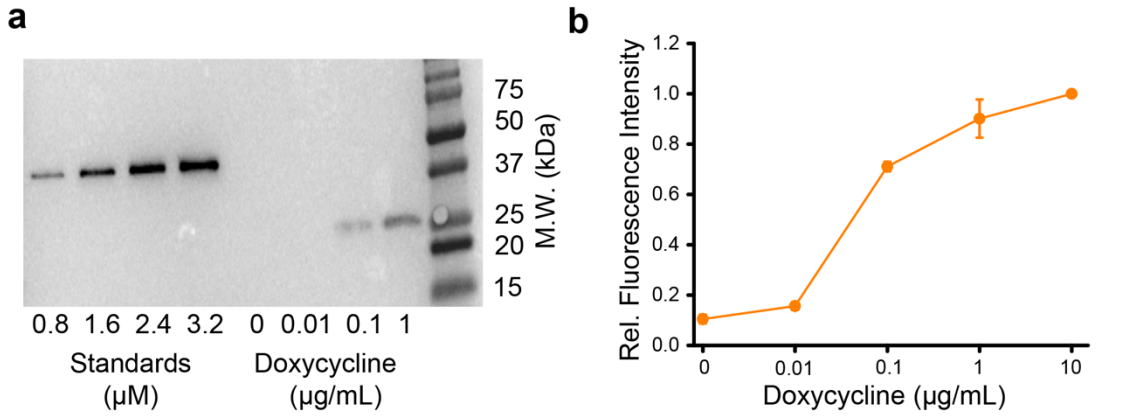

Figure S4. Western blotting of AQP1 expressed on the membrane of CHO cells. **(a)** Representative western blot of FLAG-tagged bacterial alkaline phosphatase standards (indicated in terms of their equivalent cellular concentration) alongside lysate fractions from CHO cells induced with the indicated concentrations of doxycycline. **(b)** GFP fluorescence from CHO cells induced with the indicated concentrations of doxycycline. The fluorescence comes from IRES-GFP downstream of AQP1.

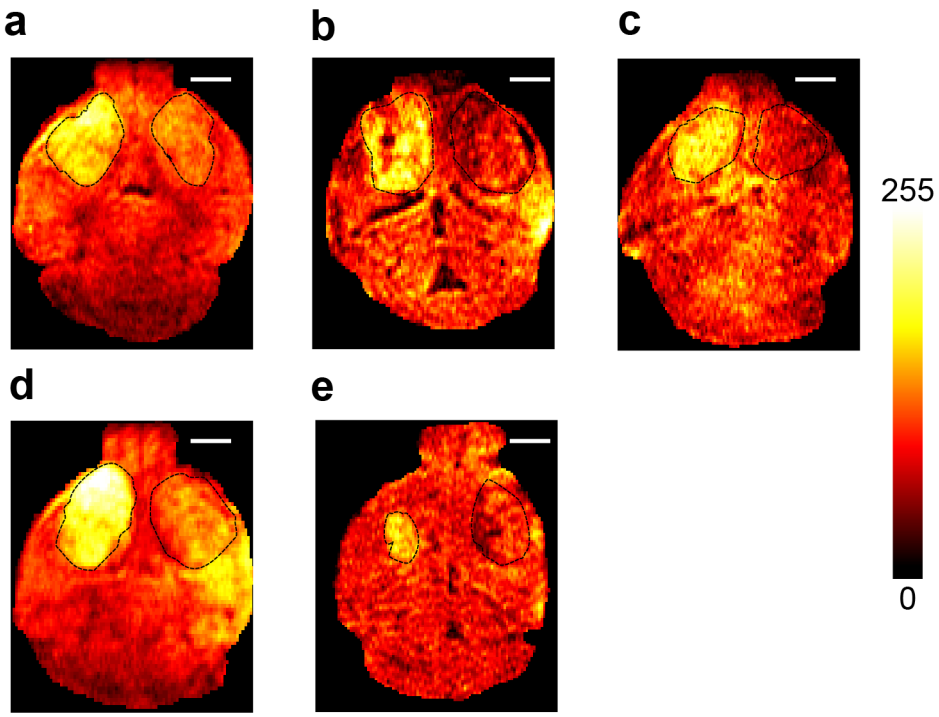

Figure S5. Diffusion-weighted images of horizontal slices of the mouse brains with bilateral tumor xenografts, acquired 48 hours following intraperitoneal injection of doxycycline. AQP1-expressing tumors (right striatum) are visibly dimmer than the contralateral GFP-expressing tumors (left striatum). Diffusion-weighted images were acquired using a DWI sequence with Δ_{eff} = 98 ms and b = 1000 s/m^2 using a Bruker 7T horizontal bore MRI. Tumor ROI(s) are indicated using solid black lines. Scale bar is 2 mm.